

Structure properties relations for polyamide 6

Citation for published version (APA):

Parodi, E. (2017). *Structure properties relations for polyamide 6*. [Phd Thesis 1 (Research TU/e / Graduation TU/e), Mechanical Engineering]. Technische Universiteit Eindhoven.

Document status and date:

Published: 26/10/2017

Document Version:

Publisher's PDF, also known as Version of Record (includes final page, issue and volume numbers)

Please check the document version of this publication:

- A submitted manuscript is the version of the article upon submission and before peer-review. There can be important differences between the submitted version and the official published version of record. People interested in the research are advised to contact the author for the final version of the publication, or visit the DOI to the publisher's website.
- The final author version and the galley proof are versions of the publication after peer review.
- The final published version features the final layout of the paper including the volume, issue and page numbers.

[Link to publication](#)

General rights

Copyright and moral rights for the publications made accessible in the public portal are retained by the authors and/or other copyright owners and it is a condition of accessing publications that users recognise and abide by the legal requirements associated with these rights.

- Users may download and print one copy of any publication from the public portal for the purpose of private study or research.
- You may not further distribute the material or use it for any profit-making activity or commercial gain
- You may freely distribute the URL identifying the publication in the public portal.

If the publication is distributed under the terms of Article 25fa of the Dutch Copyright Act, indicated by the "Taverne" license above, please follow below link for the End User Agreement:

www.tue.nl/taverne

Take down policy

If you believe that this document breaches copyright please contact us at:

openaccess@tue.nl

providing details and we will investigate your claim.

Structure Properties Relations for Polyamide 6

Emanuele Parodi

Structure Properties Relations for Polyamide 6 by Emanuele Parodi
Technische Universiteit Eindhoven, 2017.

A catalogue record is available from the Eindhoven University of Technology Library
ISBN: 978-90-386-4378-6

This thesis was prepared with the L^AT_EX 2_ε documentation system.
Reproduction: University Press Facilities, Eindhoven, The Netherlands.
Cover design: Biryukovadesign

This thesis is a result of the research programme of the Dutch Polymer Institute DPI,
“Processing for Enhanced Product Performance”, Project #786t.
DPI, P.O. Box 902, 5600 AX Eindhoven, the Netherlands.

Structure Properties Relations for Polyamide 6

PROEFSCHRIFT

ter verkrijging van de graad van doctor aan de Technische Universiteit Eindhoven, op gezag van de rector magnificus prof.dr.ir. F.P.T. Baaijens, voor een commissie aangewezen door het College voor Promoties, in het openbaar te verdedigen op donderdag 26 oktober 2017 om 16:00 uur

door

Emanuele Parodi

geboren te Recco (Genua), Italië

Dit proefschrift is goedgekeurd door de promotoren en de samenstelling van de promotiecommissie is als volgt:

Voorzitter:	prof. dr. ir. A.A. van Steenhoven
Promotoren:	prof. dr. ir. G.W.M. Peters prof. dr. ir. L.E. Govaert (UT and TU/e)
Leden:	prof. dr. P. van Puyvelde (KU Leuven) prof. dr. C. Schick (Universität Rostock) prof. dr. R.P. Sijbesma prof. dr. S. Rastogi (Maastricht University)
Adviseur:	dr. ir. L. Balzano (DSM Research)

*Het onderzoek of ontwerp dat in dit proefschrift wordt
beschreven is uitgevoerd in overeenstemming met de TU/e Gedragscode
Wetenschapsbeoefening.*

Contents

Summary	ix
1 Introduction	1
1.1 Polyamide 6	1
1.1.1 Crystal structure and hydrogen bonding	2
1.1.2 Water absorption	2
1.2 Motivation	3
1.3 Scope and outline of the thesis	4
2 Prediction of plasticity-controlled failure in polyamide 6	7
2.1 Introduction	8
2.2 Background	9
2.3 Experimental	10
2.3.1 Material	10
2.3.2 Sample preparation	10
2.3.3 Sample conditioning	10
2.3.4 Mechanical tests	10
2.3.5 X-ray diffraction	11
2.3.6 Dynamical mechanical thermal analysis	12
2.4 Results and discussion	12
2.4.1 Yield kinetics - dry state	12
2.4.2 Deformation mechanisms	14
2.4.3 Influence of temperature	14
2.4.4 Influence of humidity	16
2.4.5 Long-term failure	20
2.5 Conclusions	22
2.6 Acknowledgments	22
Appendix A	23

3	Glass transition temperature versus structure of polyamide 6: a flash-DSC study	25
3.1	Introduction	26
3.2	Experimental	27
3.2.1	Materials	27
3.2.2	Differential scanning calorimetry	28
3.2.3	X-ray diffraction	31
3.3	Results and discussion	32
3.3.1	Relations between phase contents	37
3.3.2	Relation between Tg and the RAF and MAF content	44
3.4	Conclusions	47
3.5	Acknowledgments	47
	Appendix A	48
	Appendix B	50
	Appendix C	50
4	Structure-properties relations in polyamide 6 processed in quiescent condition	53
4.1	Introduction	54
4.2	State of the art	54
4.3	Experimental	56
4.3.1	Material	56
4.3.2	Sample preparation	56
4.3.3	Sample conditioning	57
4.3.4	Mechanical tests	57
4.3.5	X-ray diffraction	57
4.3.6	Dynamical mechanical thermal analysis	58
4.4	Results and discussion	59
4.4.1	Samples characterization	59
4.4.2	Mechanical properties	60
4.4.3	Influence of temperature	62
4.4.4	Influence of humidity	64
4.4.5	Time-to-failure	70
4.4.6	Structure-properties relations	71
4.5	Conclusions	74
4.6	Acknowledgments	74

5 Injection molding of polyamide 6: influence of mold temperature on the yield and failure kinetics at different environmental conditions	75
5.1 Introduction	76
5.2 State of the art	76
5.3 Experimental	77
5.3.1 Material	77
5.3.2 Sample preparation	78
5.3.3 Sample conditioning	78
5.3.4 Mechanical tests	79
5.3.5 X-ray diffraction	79
5.3.6 Dynamical mechanical thermal analysis	81
5.3.7 Dilatometry - PVT	81
5.4 Results and discussion	81
5.4.1 Samples characterization	81
5.4.2 Yield kinetics	85
5.4.3 Structures-properties relations for modelling	88
5.4.4 Influence of temperature	90
5.4.5 Influence of the conditioning environment	90
5.4.6 Creep tests	95
5.5 Conclusions	98
5.6 Acknowledgments	98
6 Conclusions and recommendations	99
6.1 Conclusions	99
6.2 Recommendations	101
References	103
Samenvatting	111
Acknowledgments	113
Curriculum Vitae	115
List of publications	117

Summary

Engineering polymers are used in a multitude of load-bearing applications where structural integrity and long-term reliability are of extreme importance. At present their reliability can only be warranted after full-scale testing of real products. This procedure is costly and time-consuming, hampering product optimization and a flexible response to market demands.

The aim of this project is to develop new experimental methods, tools and protocols that allow a fast and accurate estimation of lifetime of load-bearing polymer constructs, taking into account the interaction of the structural performance with processing and shaping conditions. Such tools will enable structural optimization in very early stages of design, leading to lighter, more reliable products with short time-to-market and enhanced service life.

The complexity of this project results mainly from the polymorphism and the moisture-induced depression of the glass transition of polyamide 6; these two phenomenon lead to substantial differences in properties and therefore the product performances, as widely discussed in this thesis.

Firstly, an empirical method able to predict the plasticity controlled failure of PA6 conditioned at different relative humidity was developed. This was possible with a modification of the Ree-Eyring equation. This equation is generally used to predict the yield kinetics as a function of temperature and strain rate. In order to include the effect of moisture absorption, the temperature was replaced with a so called apparent temperature which takes into account the Tg depression. The modification is based on the hypothesis that the distance to Tg is determining in the mechanical response. This model was initially applied on samples processed in the same way, i.e. quiescent crystallization at 80°C, which lead to crystallization of γ -form. Then, to understand the relation between structure and properties, different thermal histories were investigated in the case of compression and injection molding.

Next, the influence of processing on the structures formation was investigated. Initially, flash-DSC (ultra-fast scanning calorimetry) was employed to characterize the crystallization kinetics. Then, compression and injection molding were used to produce macroscopic samples

of which, by the use of wide and small angle X-ray diffraction techniques, a crystallographic characterization was made; clear differences in crystallization kinetics among the three techniques were found.

Moreover, an influence of structure formation on the dry glass transition temperature was found. This phenomenon was studied by flash-DSC in the case of isothermal crystallization and continuous cooling. Observation showed that glass transition temperature does not depend on crystallinity but on the structures formation. Introducing the concept of rigid amorphous phase (i.e. a constricted amorphous), a correlation between RAF and T_g was found and eventually a model able to estimate the dry T_g for a given thermal history was made.

To conclude, this project has given rise to a set of methods that facilitate the prediction of properties of PA6 accordingly to the thermal and humidity conditions.

Chapter 1

Introduction

1.1 Polyamide 6

Polyamides are widely used as engineering polymers, with a multitude of applications such as fibers for clothing, ropes, structural and mechanical components, reinforcements in tires and adhesives. Because of their excellent properties, polyamides covers a considerable part of the world engineering polymers market [1]. The main user is the transportation manufacturing industry, covering 35% of the polyamide (PA) consumption [2].

Polyamide, also known as Nylon, was invented by the American chemist Wallace Hume Carothers in 1935. At that time, Carothers was working for Du Pont (an American chemical industry) as a group leader. The development of Nylon was driven by the Japanese silk monopoly in the late 30's, from which a legend about the Nylon's acronym etymology was born: "Now You've Lost, Old Nippon". However, this is only one of the many legends about Nylon's name.

The main characteristic of polyamide is that they contain a recurring amide group (-CONH-) in the chain [3]. Polyamide can be split in two categories, namely aromatic and aliphatic. Nylons are conventionally identified by the number of carbon atoms present in the monomer. Two monomers are often needed, a diamine and a diacid monomers. Consequently, polyamides are differentiated by two numbers: the first one corresponds to the number of carbon in the diamine and the second one to that in the diacid, see figure 1.1. Acid and amine groups can be also found in the same monomer. If that is the case, the name is defined by a single digit alike the case of polyamide 6 and polyamide 11.

The synthesis of polyamides can be carried out in several ways such as bulk polyamidation (polycondensation), anionic polymerization, polyamidation in solution [4]. The main object of this thesis is the polyamide 6 (Nylon 6), which is polymerized mainly by hydrolytic ring opening polymerization of ϵ -caprolactam at 250-270°C. This technique consists of three equilibrium reactions. The first step is the hydrolysis of ϵ -caprolactam forming ϵ -aminocaproic acid followed by the addition by ring opening polymerization (ROP) of ϵ -caprolactam to the

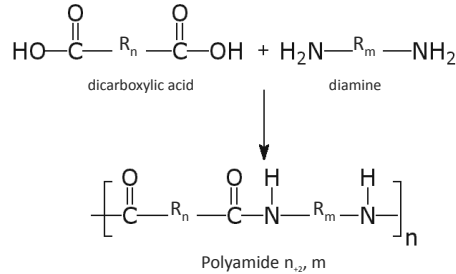


Figure 1.1: Nomenclature of polyamides.

amine end group of a growing chain (which can also be the ϵ -aminocaproic acid). The polycondensation reaction between the amine and carboxylic acid end groups leads to high molecular weight product where water is released. The ROP and the polycondensation reaction occur simultaneously during a significant part of the process.

1.1.1 Crystal structure and hydrogen bonding

Polyamide 6 is a semi-crystalline polymer, this means that, if solidified with a suitable cooling rate, parts of its macromolecules will organize in ordered region (crystals). Crystallinity is an often desired feature, as it provides strength, stiffness, and temperature stability. Another very important contribution to PA yield stress is given by the hydrogen bonds that can be formed between chains. The H-bonds are stronger than Van Der Waals interactions but weaker than covalent bonds, and they are formed between the amide and carbonyl group. The chains are oriented in a way to maximize the hydrogen bonding which also provides high regularity [5, 6]. By melt processing, PA6 crystallize usually in two phases: i) monoclinic α -phase and ii) pseudo-hexagonal γ -mesophase. They can be obtained throughout different processing, low cooling rates ($\dot{T} < 8^\circ\text{C/s}$) and intermediate cooling rates ($8^\circ\text{C/s} < \dot{T} < 100^\circ\text{C/s}$) for α and γ , respectively [7]. Please note that the chain conformations of α and γ are different, causing a different position of H-bonds along the chains, as shown in figure 1.2b.

1.1.2 Water absorption

The polar character of PA6's monomer implies also that interactions between chains and surroundings may occur. In fact, if exposed to a humid environment, part of the H-bonds between chains are broken and reconverted to connect with the water molecules [8–10]. The amount of absorbed water is dependent on the temperature and relative humidity of the

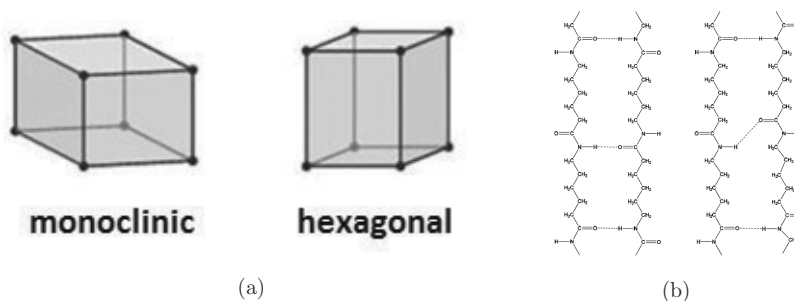


Figure 1.2: a) Unit cell: left) monoclinic (α) and right) hexagonal (γ). b) H-bonds distribution in the case of left) α and right) γ crystals.

surrounding environment, and it is proportional to the amorphous fraction [11]. The decrease of H-bonds between chains leads to an enhancement of mobility, that results in a decrease of the glass transition temperature [12]. This phenomenon, often called “plasticization”, leads to a strong decrease of the mechanical properties [13–15]. Moreover, the hydration-induced drop of T_g can lead to changes in the material morphology [16].

1.2 Motivation

Engineering polymers are used in a multitude of load-bearing applications where structural integrity and long-term reliability are of the utmost importance. In the design and optimization of polymer components for load-bearing applications the ability to estimate their lifetime in service is essential. With the increasing social demand for durable products with long service life, and a gradual shift to more critical applications, e.g. involving high loads and temperatures (e.g. under-hood automotive applications, domestic hot water systems), the need for predictive methods is even more vital.

A complicating factor is that the polymer’s intrinsic material properties depend strongly on the processing conditions (pressure, temperature, flow), generally leading to anisotropy and a spatial variation of the mechanical performance throughout the product.

For amorphous polymers, this problem is solved. A method to monitor the evolution of yield stress resulting from physical aging in glassy polymers was proposed [17, 18]. In combination with the thermal history during cooling from the melt (obtained from commercial processing simulation tools like Moldflow[®]), the yield stress distribution in an injection molded products can be obtained as well as its lifetime (ductile failure) in static loading conditions.

The situation is much more complex in the case of semi-crystalline polymers where structural features, such as degree of crystallinity, lamellar thickness and orientation, that strongly

influence their mechanical properties, may drastically vary depending on the conditions under which the material is processed [19, 20]. The ability to predict the development of crystalline orientation under realistic processing conditions is, therefore, a critical component in tackling processing-property relations for these materials.

In the case of isotropic structures, the morphology will be largely determined by the thermal and pressure history during processing. A complicating factor is the possibility of polymorphism, that is for instance encountered in polyamide 6 (PA6). By melt processing, neat PA6 can crystallize in two forms: a monoclinic α -phase and a pseudo-hexagonal γ -mesophase [7, 21]. The final composition (α/γ) of the solidified material is determined by subtle details of the pressure and temperature history [22, 23], but generally both phases are observed in injection molded products [24]. The mechanical properties of the α -phase and γ -mesophase are quite different [25], which leads to rather strong variations in mechanical performance with slight changes in the processing procedure.

1.3 Scope and outline of the thesis

This thesis aims to investigate the influence of processing on the structures formation, and the structures-properties relations at the final scope of obtaining a unified model to determine the mechanical properties starting from a given thermal history. To achieve such an ambitious goal, each topic was first approached from an experimental point of view, and subsequently, to describe the obtained results, empirical models were proposed.

In **Chapter 2**, a method to predict yield and failure kinetics at different relative humidity and temperature of samples processed in quiescent conditions with the same thermal history, is proposed. The Ree-Eyring equation was modified by the introduction of an “apparent” T , that takes into account the depression of T_g due to hydration. The enhancement of mobility due to the depression of T_g is associated to an increase of the testing temperature. By this modification of the Ree-Eyring, the yield kinetics as a function of temperature and relative humidity is described.

Chapter 3 focuses on the glass transition temperature. The influence of thermal history on the dry glass transition (T_g) of PA6 is investigated by the use of flash-DSC. The investigation leads to a relation between T_g and the formation of rigid amorphous phase. Three equations able to predict the rigid amorphous fraction (RAF), mobile amorphous fraction (MAF) and their relations with the glass transition temperature are proposed.

In **Chapter 4** the method developed in Chapter 2 is extended to different thermal histories (α , γ and l_c); always in quiescent condition. A relation between l_c and the rate factors

(Ree-Eyring parameters) is found. Moreover, a strong influence of mold temperature on the mechanical response and thermal stability is presented.

In **Chapter 5**, the challenging injection molding process is studied. In particular the influence of mold temperature on the crystallographic and mechanical properties, is investigated. The method proposed in chapter 2 and extended in chapter 4 is also applied in the case of injection molded samples. An important influence of mold temperature, pressure and shear flow on the sample properties is found. It concludes that, injection molding processing induces different morphologies over the sample thickness, which are determining for the mechanical response.

Chapter 2

Prediction of plasticity-controlled failure in polyamide 6: influence of temperature and relative humidity

Abstract

In this study, the influence of temperature and relative humidity on the plasticity controlled failure of polyamide 6 was investigated. Uniaxial tensile tests were performed at several temperatures, strain rates and relative humidity; creep tests under constant load were performed at different relative humidity and applied load. In order to describe and predict the yield kinetics, the Ree-Eyring equation was employed and modified to include the effect of relative humidity. Subsequently, by the introduction of the concept of critical amount of accumulated plastic strain, the yield kinetics were successfully translated to predictions of time-to-failure. A good agreement between predictions and experimental results is obtained, showing that the model is a suitable and versatile tool to evaluate mechanical performance of a temperature and moisture sensitive material such as polyamide 6.

2.1 Introduction

Polyamide 6 (PA6) is one of the most commonly used engineering polymers, which can be found in the form of fibers, films and also injection molded products. In the past decades, it was also introduced in the field of load-bearing applications such as mechanical parts, under-hood components and sport items that are often exposed to demanding conditions combining high load, high temperature regimes and high relative humidities. These applications require a high level of reliability, thus an investigation of humidity and temperature influence on the mechanical properties is required.

Polyamide 6 is an aliphatic polyamide, the monomer has two polar groups: the amide and carbonyl group. Hydrogen bonds can be formed between chains, resulting in high modulus and yield strength [26]. However, the polar character also causes a crucial issue of PA6: hygroscopicity [27]. If exposed to a humid environment, PA6 absorbs water up to a saturation level which typically depends on temperature and relative humidity [16]. When this occurs, part of the hydrogen bonds are broken and new H-bonds are formed with the absorbed water molecules [12]. This phenomenon leads to plasticization and results in a depression of the glass transition temperature [8] which also results in a considerable degradation of the mechanical properties [14, 28–30]. In case of exposure to humidity, T_g can drop to values below room temperature, in which case structural changes at room temperature may occur [31].

Another characteristic of PA6 is polymorphism. If solidified starting from the molten state, it can crystallize in two forms, i) the most stable α -phase (monoclinic cell), which is obtained in low under-cooling or in isothermal crystallization at temperatures exceeding 170°C, and ii) the less stable γ -mesophase (pseudo-hexagonal cell) obtained at high under-cooling or isothermal crystallization at temperatures between T_g and 170°C. In case of very fast cooling ($>100^\circ\text{C/s}$), also a completely amorphous sample can be obtained [7].

Although lifetime prediction of polymers is a widely investigated topic, studies regarding neat PA6 are hardly found in literature, most of the studies in literature are focused on PA6 nanocomposites [32, 33]. In general it is known that three different failure modes can be distinguished: a) plasticity controlled failure (high applied load), b) slow crack growth (medium load) and, c) molecular degradation (low or no load) [34]. The latter is regarded to be independent of applied stress, and is, at least in PA6, not regarded as a limiting factor. Crack growth controlled failure is mainly studied by cyclic fatigue [35–37], however it is a failure regime hardly achieved in the case of polyamide 6, due to its excellent fatigue properties. Finally, the plasticity controlled regime, where failure occurs by accumulation of plastic deformation, can be studied by uniaxial tensile test at constant applied strain rate and constant applied load (creep).

In this study, a model able to predict the plasticity controlled failure of polyamide 6 at different temperatures and relative humidity is presented.

2.2 Background

Under constant load, solid polymers tend to display time dependent deformation (creep) and, ultimately, creep rupture occurs. A creep curve can be divided in three regimes: primary creep where the strain rate decreases in time, secondary creep in which strain rate remains constant, and tertiary creep where strain rate increases in time due to intrinsic or geometric softening which eventually leads to failure. The time-to-failure depends on the applied load and temperature, where an increase of these two leads to a decrease of time-to-failure, as shown in literature by [38, 39]. Important in lifetime prediction is an estimate of the plastic flow during secondary creep. Bauwens-Crowet *et al.* [40], has shown that the steady state reached at yield point in constant strain rate experiment is the same as the one reached during secondary creep. Thus, stress- and temperature-dependence measured in constant strain rate experiments can be used to characterize the kinetics of plastic flow. The deformation kinetics is described by the Eyring's activated flow theory [41]:

$$\dot{\epsilon}_{pl}(\sigma, T) = \dot{\epsilon}_0 \exp\left(-\frac{\Delta U}{RT}\right) \sinh\left(\frac{\sigma V^*}{kT}\right) \quad (2.1)$$

where $\dot{\epsilon}_0$ is a rate factor, σ is the yield stress, V^* is the activation volume, ΔU is the activation energy, R is the universal gas constant, k is the Boltzmann's constant and T the absolute temperature.

Plotting the plastic flow rate for each applied load as a function of the corresponding time-to-failure, a linear relation with slope -1 (in a double logarithmic plot) is found [42], implying that the product of $\dot{\epsilon}_{pl}$ and t_f is a constant:

$$\dot{\epsilon}_{pl}(\sigma) \cdot t_f(\sigma) = C \quad (2.2)$$

This constant C can be defined as the critical strain, ϵ_{cr} , which equals the accumulated plastic strain for a material subjected to the plastic flow rate, $\dot{\epsilon}_{pl}$. By this phenomenological approach and by the stress-temperature-dependence of the plastic flow rate, the prediction of time-to-failure under a constant load is achieved:

$$t_f(\sigma, T) = \frac{\epsilon_{cr}}{\dot{\epsilon}_{pl}(\sigma, T)} \quad (2.3)$$

In order to determine the stress- and temperature-dependence of the plastic flow rate, constant strain rate experiments are the most suitable because of their logistic advantages and planning possibilities. The stress strain response in uniaxial extension initially shows a linear elastic region, in which chain mobility is negligible and the elastic modulus depends on intermolecular interactions among chains. With increasing stress, mobility increase gradually, changes in chain conformation take place, with a resulting plastic deformation; at higher stress levels, the mobility increases even further with stress until the resulting plastic flow rate exactly matches the applied strain rate, this point is called yield stress. It is known that

deforming a solid polymer at higher strain rate, a higher mobility is required to obtain the same balance; hence, the yield stress will increase.

2.3 Experimental

2.3.1 Material

The material employed in this work was a polyamide 6 (Akulon K122) kindly provided by DSM (The Netherlands). This PA6 has a viscosity-average molar mass (M_v) of about 24.9 kg/mol.

2.3.2 Sample preparation

Sheets with a thickness of 0.5mm were prepared by compression molding. After a careful drying procedure (1 night at 110°C under vacuum) the pellets were placed in a “sandwich” consisting of two thick steel plates (about 3mm), two thin aluminum foils (about 0.2mm) and a 250×250×0.5mm steel mold. The material was melted at 265°C for 5 minutes, while a force of about 10kN was applied. Then, the “sandwich” was rapidly moved to a cold press set at 80°C where the material was solidified in quiescent condition for 3 minutes. Dog-bone samples, according to the ISO527 type 1BA, were prepared using a cutting die (main measures: width 5mm, length 22mm).

2.3.3 Sample conditioning

To investigate the influence of hydration, samples were stored at four different relative humidities, RH0% (dry), RH35%, RH50% and RH75%. In the case of dry conditioning, samples were stored in a desiccator under vacuum at room temperature; for RH50% an environmental chamber was employed. While in the case of RH35% and RH75% two desiccators, containing supersaturated salt solutions able to maintain a constant relative humidity in a close environment, were used. The salts were sodium chloride and magnesium chloride hexahydrate for RH75% and RH35% respectively.

2.3.4 Mechanical tests

Uniaxial tensile tests and creep tests under constant load were performed using a Zwick Z010 Testing Machine equipped with a 1kN load-cell. The testing area was surrounded by an environmental chamber which allows to test at controlled temperature and humidity. The tensile tests were performed, at least in duplicates, in a range of strain rates from $10^{-5} s^{-1}$ up to $3 \cdot 10^{-2} s^{-1}$, temperatures between -40°C and 120°C (in dry condition) and relative humidity of 35, 50 and 75% (at room temperature). Before starting the experiments, a pre-load of 0.1 MPa was applied at a speed of 1mm/min. Creep measurements were performed at a relative

humidity of 35, 50, and 75%. The stress was applied within 10 seconds and subsequently kept constant until failure. The time-to-failure was estimated as the time at which the strain reaches the value of 25%, which was defined as strain at failure. The plastic flow rate ($\dot{\epsilon}_{pl}$) was estimated as the minimum in a Sherby-Dorn plot [43].

2.3.5 X-ray diffraction

Wide angle x-ray diffraction was performed at the European Synchrotron Radiation Facility in Grenoble (FR) at the Dutch-Belgian beamline (DUBBLE). After normalization, the crystallinity was estimated by subtracting an amorphous halo (experimentally obtained) to the measured patterns. The weight percentage of crystallinity is finally calculated by:

$$\chi_c = \frac{T - A}{T} \quad (2.4)$$

where T is the total scattered intensity and A is the scattering from the amorphous halo. In order to estimate the effect of different conditioning on the crystallographic structures, a deconvolution analysis was performed. This was obtained by fitting Lorentzian functions, in proximity of each characteristic reflection. Eventually, all the Lorentzian functions and the amorphous halo were summed to verify the fidelity of the fitting procedure (green markers in figure 4.1). Thus, the relative quantities $\chi_{c,\alpha}$ and $\chi_{c,\gamma}$ were calculated by the following:

$$\chi_{c,\alpha} = \frac{A_\alpha}{A_m} \quad \text{and} \quad \chi_{c,\gamma} = \frac{A_\gamma}{A_m} \quad (2.5)$$

where A_α and A_γ are the total area of the Lorentzian functions for the α and γ peaks, and A_m is the total area of the measured pattern. An example is given in figure 4.1.

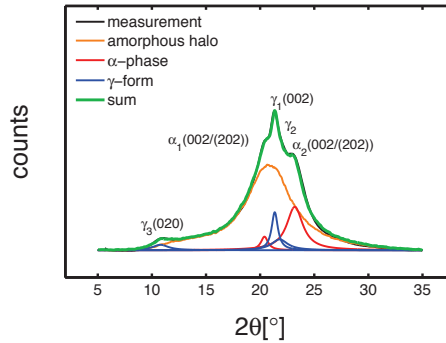


Figure 2.1: Example of WAXD pattern deconvolution analysis. The green line is the result of the deconvolution procedure, the orange line is the measured amorphous halo, blue and red curves are the Lorentzian functions.

2.3.6 Dynamical mechanical thermal analysis

In order to measure the glass transition temperature before and after conditioning, dynamical mechanical thermal analysis (DMTA) was performed by a TA instruments Q800 DMA. Samples were rectangular bars of about 5mm width, 0.5mm thickness. The experiments were carried out at a single frequency of 1Hz and along a temperature ramp from -40°C to 100°C with a heating rate of $3^{\circ}\text{C}/\text{min}$. The glass transition temperature was defined as the maximum in $\log \tan(\delta)$.

2.4 Results and discussion

The first step of this investigation was a crystallographic characterization performed by wide angle x-ray diffraction experiments. These were carried out on the dry samples at room temperature. In figure 2.2, the result of a radial integration is given. The pattern shows the characteristics of γ -form, i.e. the main peak at about 2θ 21° , and the secondary peak at about 2θ 10° . By deconvolution analysis, the crystallinity was estimated to be around 30%.

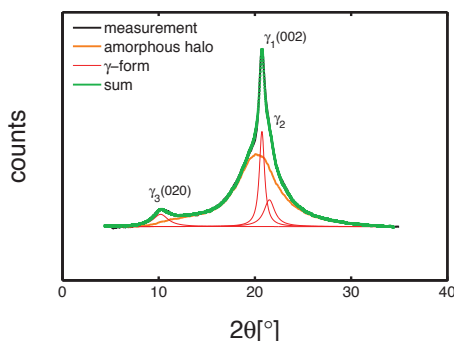


Figure 2.2: Radial integration of WAXD with deconvolution analysis.

2.4.1 Yield kinetics - dry state

The mechanical characterization started with tensile tests at several temperatures in dry condition at strain rates ranging from 10^{-4} to $3 \cdot 10^{-2} \text{ s}^{-1}$. In figure 2.3a, the stress-strain response of dry samples at several temperatures and strain rates are shown; as expected, an increase of strain rate results in an increase of yield stress. It is clear that the strain at yield varies strongly with temperature and strain rate. At 80°C , yield occurs at about 15% of strain, whereas it shifts towards 5% at 23°C . This effect is related to the presence of two different contributions to yield: i) the glassy amorphous domains at low strain and ii) the crystalline domains at higher strain. The contribution of glassy amorphous domains becomes dominant

at low temperatures and (or) high strain rates and, as a result, the strain at yield decreases. Figure 2.3b shows the yield stress as a function of strain rate at different testing temperatures for samples in the dry state. From figure 2.3b it is evident that the strain rate-dependence of yield stress displays two different slopes. This observation indicates that the deformation occurs through two different molecular deformation mechanisms that contribute to the flow stress, as already proposed by several authors [42, 44–46]. These two processes are generally attributed to an intra-lamellar deformation mechanism further referred to as processes I and an inter-lamellar mechanism, further referred to as processes II [47–49]. In figure 4.5, a schematic decomposition of the two processes is proposed. The stress contributions of both processes can be regarded to be additive, therefore the equation 2.1 is re-written, leading to:

$$\sigma_y(\dot{\epsilon}, T) = \frac{kT}{V_I^*} \sinh^{-1} \left(\frac{\dot{\epsilon}}{\dot{\epsilon}_{0,I}} \exp \left(\frac{\Delta U_I}{RT} \right) \right) + \frac{kT}{V_{II}^*} \sinh^{-1} \left(\frac{\dot{\epsilon}}{\dot{\epsilon}_{0,II}} \exp \left(\frac{\Delta U_{II}}{RT} \right) \right) \quad (2.6)$$

where $\dot{\epsilon}_{0,I}$, ΔU_I and V_I^* are the rate factor, activation energy and activation volume related to process I and $\dot{\epsilon}_{0,II}$, ΔU_{II} and V_{II}^* are related to the process II. In order to describe the results shown in figure 2.3b, the set of parameters shown in table 2.1 was employed.

Table 2.1: Eyring parameters.

	$V^* [m^3]$	$\Delta U [J mol^{-1}]$	$\dot{\epsilon}_0 [s^{-1}]$
I	$9 \cdot e^{-27}$	$1 \cdot e6$	$1 \cdot e123$
II	$1.9 \cdot e^{-27}$	$3 \cdot e5$	$2 \cdot e45$

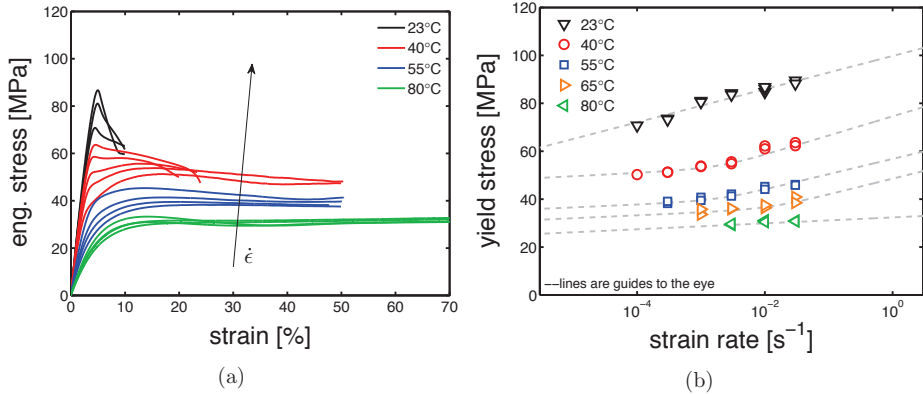


Figure 2.3: a) Stress-strain response of uniaxial tensile tests at 23, 40, 50 and 80°C in a range of strain rates from 10^{-4} to $3 \cdot 10^{-2} s^{-1}$ in dry condition. b) Yield kinetics of samples tested at different temperatures at the dry state, lines are guides to the eye.

Finally, in figure 2.4b the yield kinetics of polyamide 6 at dry state is shown, in this case the lines are results of equation 4.1.

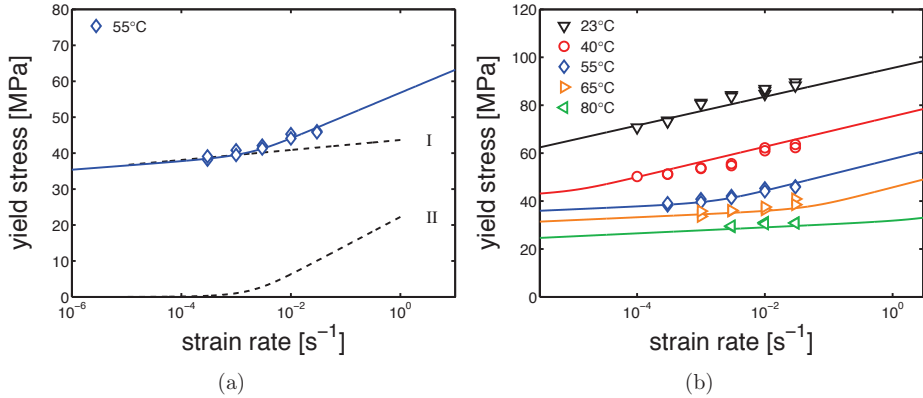


Figure 2.4: a) Yield stress versus strain rate at 55°C; the black dashed lines are the two contribution separated (process I and II). b) Yield kinetics of polyamide 6 at dry state, the lines are results of equation 4.1 with parameters shown in table 2.1.

2.4.2 Deformation mechanisms

As already mentioned, experimental evidences suggest that the deformation takes place through (at least) two different mechanisms which act in parallel. These two are strain rate-temperature-activated processes and they are additive to each other, therefore by varying the temperature (or relative humidity) and strain rate it is possible to observe deformation governed by processes I or I+II. These two mechanism are usually associated to an intra-lamellar (process I) and inter-lamellar deformation (process II). More in details, it is proposed that:

- Process I (intra-lamellar), active below melting temperature (T_m), is governed by plastic deformation of lamella via crystallographic slip, which is facilitated by the movement of screw dislocation present in the crystals.
- Process II (inter-lamellar), is related to the deformation of the inter-lamellar amorphous region. Depression of glass transition temperature and (or) an increase of temperature lead to higher mobility in the amorphous regions, which results in a lower yield stress contribution.

2.4.3 Influence of temperature

To further explore the kinetics, the stress-strain response was investigated at a single strain rate (10^{-2} s^{-1}) in a wide range of temperatures, from -40°C to 120°C , the resulting stress-strain curves are shown in figure 2.6a. In figure 2.6b the yield stress is plotted as a function of temperature, the line is the result of equation 4.1 in the case of a fixed strain rate (10^{-2}

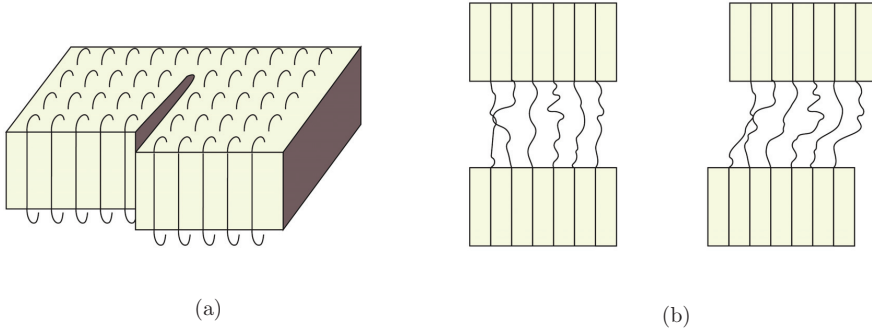


Figure 2.5: a) Screw dislocation (schematic), b) mobilization of the inter-lamellar amorphous region (schematic).

s^{-1}) and varying temperatures. As shown, the model describes the results well in the range of temperatures between 23°C and 100°C ; as far as the description at low temperatures is concerned, the deviation from the prediction is related to reduction of the strain to yield due to the onset of the stress contribution of glassy component. This causes strain localization to take place at much lower strains, see also figure 2.6a. In appendix A examples of compression tests are given; in this case, the localization does not occur, and the prediction remains in good agreement with the results, even at low temperatures.

At very high temperatures ($T > 100^{\circ}\text{C}$), the temperature-dependence of yield stress flattens; this is due to an evolution of the crystallographic structure during the test. In fact, at high temperature, well above T_g , the chain mobility is higher and lamellar thickening and (or) cold crystallization occur (this phenomenon will be called “annealing”); this leads to an increase of yield stress in time. An example of this effect is given in figure 2.7a, where the samples are tested at 110°C in a range of strain rates from $3 \cdot 10^{-4}$ up to $3 \cdot 10^{-2} s^{-1}$. Remarkably, the yield stress is observed to increase with decreasing strain rate, which is possible only in case of structural evolution during the test. Annealing is a time- and temperature-dependent phenomenon, its effect increases with increasing temperature and (or) exposure time; thus, during an experiment at low strain rate, where the exposure time is high, more annealing will occur and yield stress will increase. Moreover, to understand whether the stress plays a role in annealing kinetics, another kind of experiment was performed; tensile tests were performed at constant strain rate after conditioning the samples at 110°C for several different exposure times. In figure 2.7b yield stress is plotted as a function of exposure time; the increase of yield due to annealing starts only after about 10^4 seconds, while in the case of figure 2.7a, an increase of yield stress is visible already in the case of strain rate $10^{-2} s^{-1}$ which is equivalent to about 350 seconds (300 s without stress + 50 s with stress).

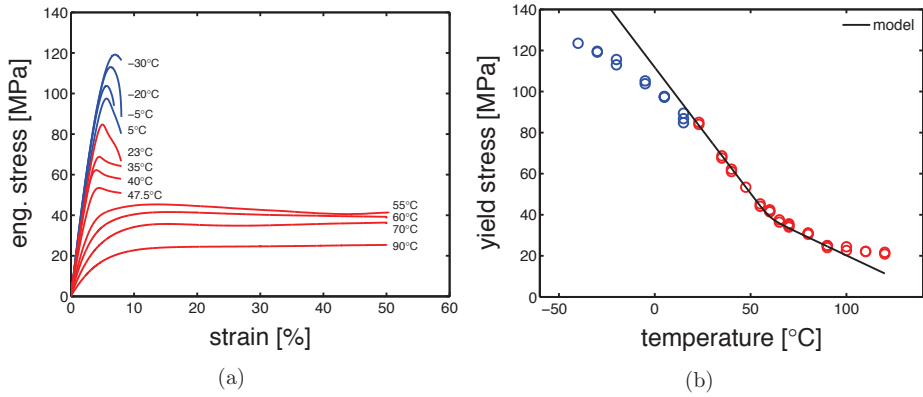


Figure 2.6: a) Examples of temperature-dependence of stress-strain response at the dry state and strain rate of 10^{-2} s^{-1} ; b) yield stress as a function of testing temperature, markers are the experimental results and the line is the prediction based on the Ree-Eyring equation.

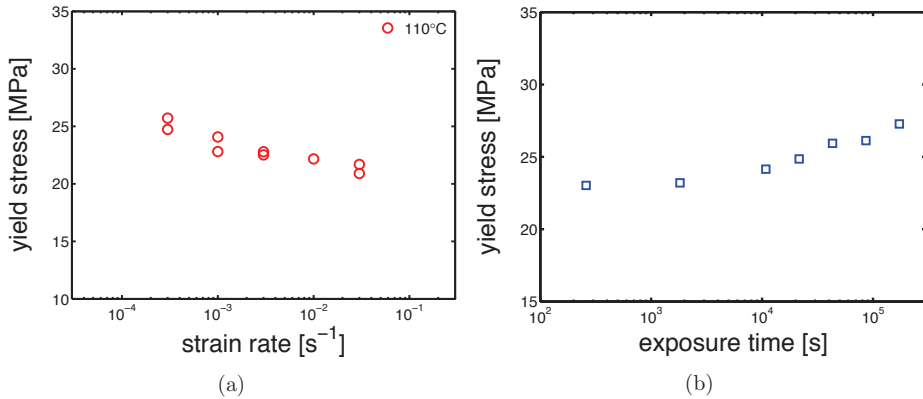


Figure 2.7: a) Yield kinetics for dry samples testes at 110°C and different strain rates. This plot shows the result of the structure evolution which takes place during testing. b) Yield stress as a function of exposure time at 110°C prior to test.

2.4.4 Influence of humidity

As explained in section 3.1, the conditioning environment (i.e. temperature and humidity) has a crucial influence on the glass transition of PA6. Consequently, the samples were exposed to four different moist environments (RH35%, RH50%, RH75% and under water) for a certain time up to saturation. The absorbed water fraction was calculated by the following:

$$H_2O\% = \left(\frac{W_i - W_0}{W_0} \right) \times 100 \quad (2.7)$$

where W_0 is the weight of the sample before conditioning and W_i is the weight at the time t_i . In figure 2.8a, an example of water absorption kinetics is shown. After a certain time, the absorbed water fraction reaches a plateau value, which is considered as the saturation level.

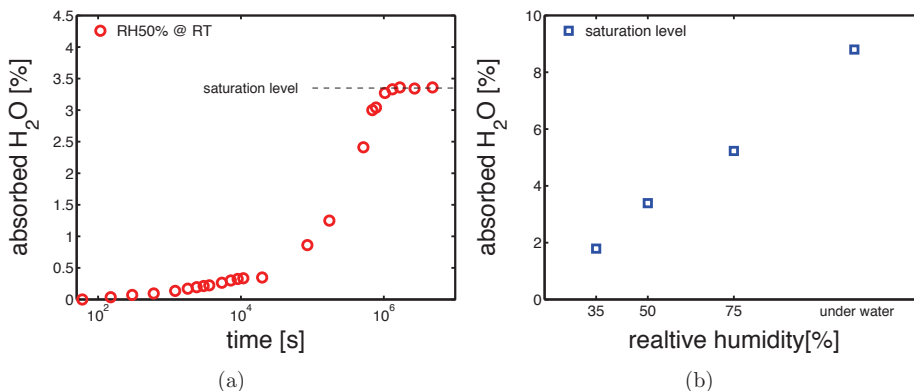


Figure 2.8: (a) Example of water absorption kinetics, the absorbed water fraction is plotted as a function of time in the case of samples soaked in water. b) Saturation level as a function of relative humidity, conditioning at 23°C.

An investigation of the moisture-induced glass transition depression was performed by DMTA. In figure 2.9a the phase angle ($\tan(\delta)$) of samples conditioned at different humidity is plotted as function of temperature. The maximum defines the glass transition temperature; as expected, T_g decreases with increasing relative humidity. In figure 2.9b, the glass transition temperatures obtained by DMTA, are plotted as a function of absorbed water fraction. T_g drops from about 60 °C for the dry sample to about -20°C for sample soaked in water. In table 2.2 the glass transition temperatures are reported.

Table 2.2: Glass transition temperature after conditioning.

[°C]	dry	RH35%	RH50%	RH75%	water
T_g	58	36	19	4	-20

If T_g reaches a value smaller or equal to the room temperature, hydration-induced crystallization may occur at room temperature during conditioning. In figure 2.10a the wide WAXD patterns are given for the four different relative humidity; figure 2.10b shows the crystalline fraction evolution as a function of relative humidity. Figure 2.10b shows the effect of hydration on crystallographic structures; as already mentioned, at dry condition the sample has a crystallinity of about 30% of consisting of solely γ -mesophase, whereas upon hydration, part of the amorphous and γ -mesophase transform into α -phase.

Next, the samples conditioned at different RH% are tested, an example is given in figure

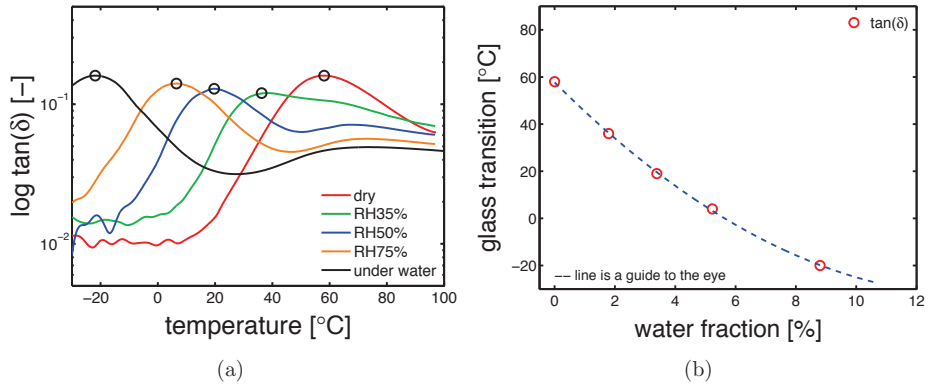


Figure 2.9: (a) DMTA results, $\log \tan(\delta)$ as a function of temperature for samples conditioned at different humidity; markers are the T_g . (b) Glass transition temperature (obtained by DMTA) as function of the water fraction absorbed by the sample.

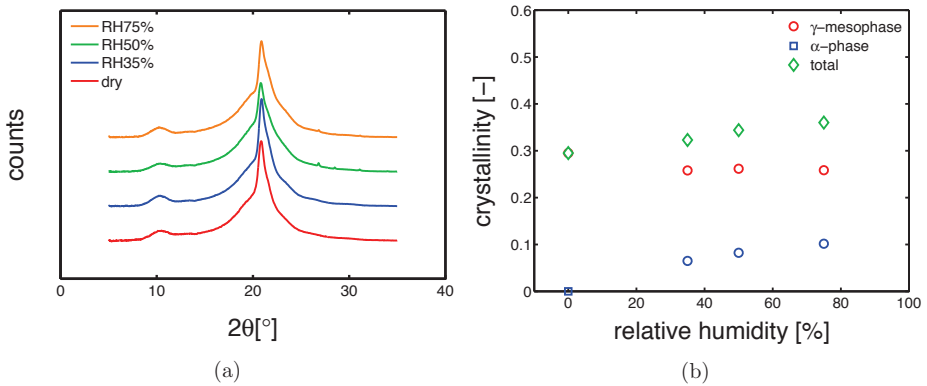


Figure 2.10: a) Wide angle x-ray diffraction integrated patterns of samples conditioned at different relative humidity and 23°C ; b) crystalline fractions as functions of relative humidity, obtained by deconvolution analysis.

Table 2.3: Crystallinity after conditioning.

[%]	dry	RH35%	RH50%	RH75%
γ - form	30	25	24	23
α - phase	0	5	7	9
total	30	30	31	32

2.11a; as mentioned, hydration lowers the stress-strain response. Experiments were performed at several strain rates and relative humidity, and the resulting deformation kinetics for samples

conditioned at different RH% are shown in figure 2.11b. In this case, the lines are the results of the Ree-Eyring equation but after a modification which includes the effect of relative humidity. The modification is based on the hypothesis that the distance to T_g is determining in the mechanical response. A humidity-induced reduction in glass transition temperature is subsequently regarded as an “apparent” increase in the ambient temperature. Consequently, we introduce an ”apparent temperature” (\tilde{T}):

$$\tilde{T} = T + (T_{g,dry} - T_{g,wet}) \quad (2.8)$$

where T is the actual testing temperature, $T_{g,dry}$ is the glass transition temperature at the dry state and $T_{g,wet}$ is the T_g after conditioning. A similar modification was applied by Söntjens *et al* [50], to describe the influence of molecular weight on the deformation kinetics of poly-D,L-lactide.

Introduction of equation 5.1 into equation 4.1 leads to:

$$\sigma_y(\dot{\epsilon}, \tilde{T}) = \frac{k\tilde{T}}{V_I^*} \sinh^{-1} \left(\frac{\dot{\epsilon}}{\dot{\epsilon}_{0,I}} \exp \left(\frac{\Delta U_I}{R\tilde{T}} \right) \right) + \frac{k\tilde{T}}{V_{II}^*} \sinh^{-1} \left(\frac{\dot{\epsilon}}{\dot{\epsilon}_{0,II}} \exp \left(\frac{\Delta U_{II}}{R\tilde{T}} \right) \right) \quad (2.9)$$

As shown in figure 2.11b, this modification results in a good prediction of yield stress, the same parameters reported in table 2.1 were employed.

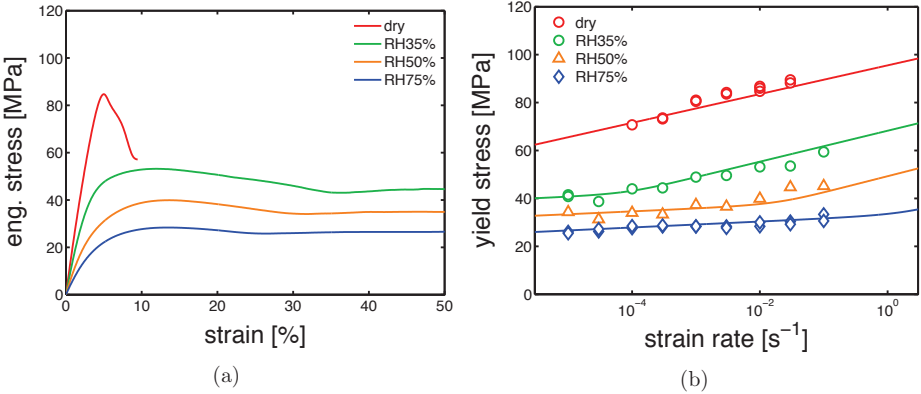


Figure 2.11: a) Examples of stress-strain response of samples conditioned at different relative humidity and tested at 23°C with a strain rate of 10^{-2} s^{-1} ; b) yield kinetics of samples conditioned at different RH% and testes at room temperature in a range of strain rates from 10^{-5} s^{-1} to $3 \cdot 10^{-2} \text{ s}^{-1}$.

Upon hydration, a decrease of yield stress is registered in both process I (intra-lamellar) and process II (inter-lamellar). As previously discussed in section 2.4.2, the inter-lamellar mechanism is related to the deformation of amorphous domains, whereas the intra-lamellar is related to movement of screw dislocations (crystal imperfections). Since water can be

absorbed only by the amorphous domains, it is straightforward to understand that the effect of hydration on the inter-lamellar deformation is due to the drop in glass transition temperature. As far as the intra-lamellar deformation is concerned, the deformation is governed by the movement of screw dislocations (defects). In order to explain the influence of hydration on this deformation mechanism, it is hypothesized that the hydration-induced plasticization not only improves mobility of the bulk amorphous region, but also enhances the mobility of the amorphous layer next to the crystal lamella; thus, the higher mobility of the amorphous local to the crystal might stimulate the movement of dislocations, facilitating the deformation.

2.4.5 Long-term failure

After the extensive investigation of deformation kinetics with experiments at constant strain rate, creep tests (constant load) are employed to study the influence of hydration on the time-to-failure. In figure 4.17a, two examples of creep test are shown; the annotations help to understand the definition of plastic flow rate ($\dot{\epsilon}_{pl}$) and critical strain (ϵ_{cr}). To predict lifetime we have made use of an experimental observation; if we perform creep at several applied loads and plot the plastic flow rate as a function of time-to-failure in a double-logarithmic plot, a slope of -1 is found, see figure 4.17b. This implies, as stated in section 2.2 equation 5.3, that the product of the plastic flow rate ($\dot{\epsilon}_{pl}$) and the time-to-failure (t_f) is constant.

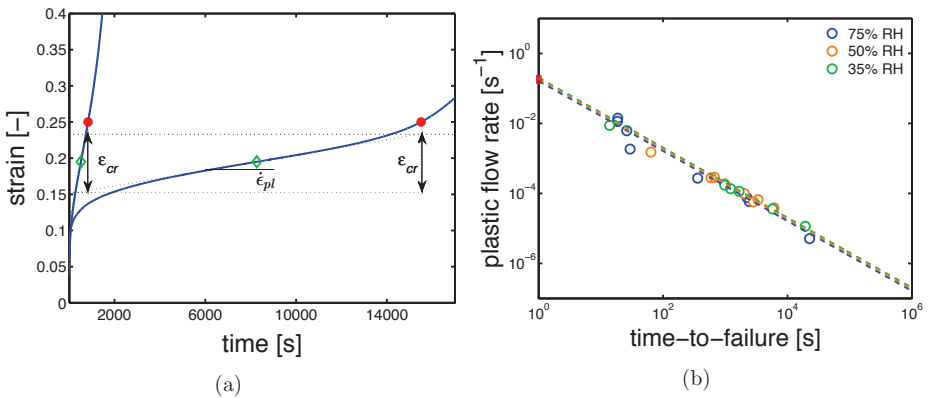


Figure 2.12: a) Example of creep test at constant applied load, it shows the definition of $\dot{\epsilon}_{pl}$, ϵ_{cr} and t_f . b) Plastic flow rate as a function of time to failure for samples conditioned at different relative humidity.

Figure 2.13a demonstrates that the kinetics of plastic flow rate during secondary creep (open markers) matches the strain rate dependence of yield stress measured in short-term constant strain rate experiments (solid markers). The lines are results of equation 5.2 employing the parameters listed in table 2.1. To describe the time-to-failure results, the modified

Ree-Eyring equation (eq. 5.2) combined with the critical strain were employed, as shown in figure 2.13b. Note that lines have the same absolute stress dependency (slope) in both figure 2.13a and 2.13b, but with opposite signs. Finally, as shown in figure 2.13b, the model gives a satisfactory description of the experimental results, therefore it is suitable to predict of long term plastic failure of polyamide 6 conditioned at different relative humidities.

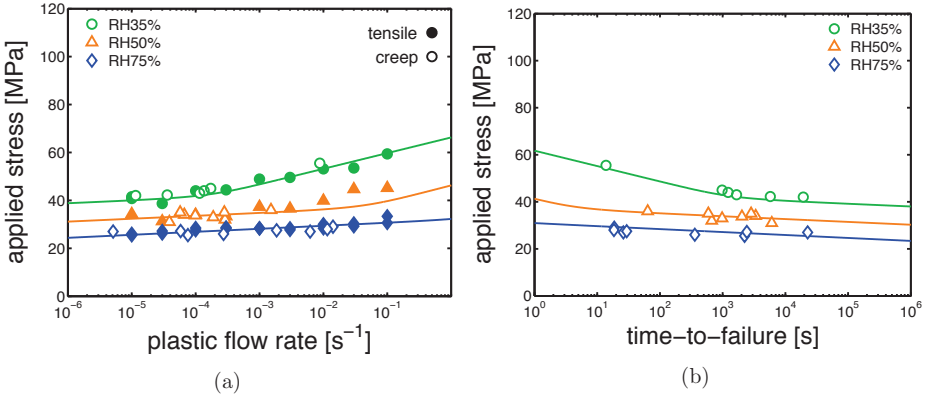


Figure 2.13: Applied stress as a function of a) plastic flow rate and b) time-to-failure for samples conditioned at different relative humidity. In figure a) the solid markers are the results of tests at constant strain rate, open markers are results of creep test and lines the results of equation 5.2. Figure b) shows the results of creep test and lines are the results of combined 5.2 and 5.3.

2.5 Conclusions

In this study, the effect of temperature and relative humidity on the mechanical properties of melt processed polyamide 6 was investigated. PA6 shows a strong dependency on temperature, in the investigated range (from -40°C to 120°C) yield stress varies from about 125 MPa to 20 MPa at a strain rate of 10^{-2} s^{-1} . Hydration strongly lowers the glass transition temperature, this affects substantially the mechanical properties. The pre-existing Ree-Eyring equation was modified in order to include the effect of humidity (T_g depression), the temperature was replaced by the “apparent temperature”. After this modification, the Eyring equation is therefore suitable to predict the deformation kinetics of polyamide 6 at different temperatures and relative humidity. Moreover, by the introduction of the critical strain, the predictions made for the deformation kinetics (tensile test - constant plastic strain rate) can be translated also to predictions of time-to-failure (creep test - constant load) for different relative humidity.

2.6 Acknowledgments

This work is part of the Research Program of the Dutch Polymer Institute DPI, Eindhoven, the Netherlands, project number #786.

Appendix A

In order to explain the partial mismatch between prediction and results of figure 2.6a, compression tests were performed with strain rate 10^{-2} s^{-1} (the same of tensile test) in a range of temperatures from -40°C to 120°C . The experiments were performed on cylindrical sample of about 3 mm height and 3 mm diameter; in order to decrease the friction between sample and the compression tool, they the samples were wrapped in PTFE tape and before every experiment, a layer of PTFE spray was sprayed on the testing surfaces.

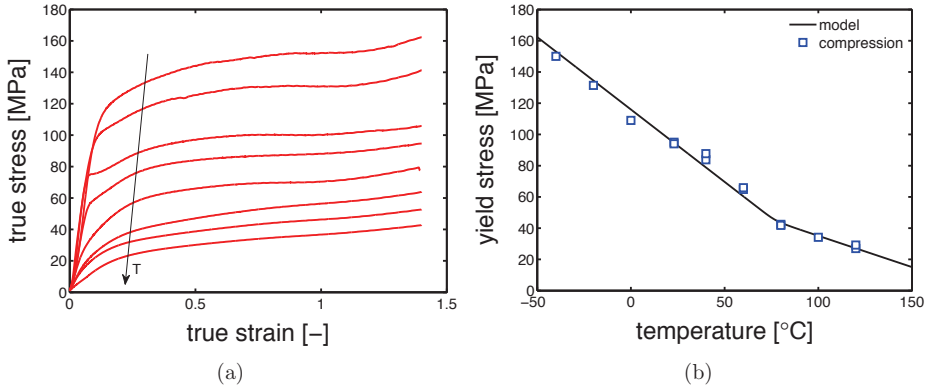


Figure 2.14: Compression tests. a) True stress versus true strain of samples tested in a range of temperatures from -40 to 120°C with a strain rate of 10^{-2} s^{-1} . b) Yield stress as a function of temperature of samples tested in a range of temperatures from -40 to 120°C with a strain rate of 10^{-2} s^{-1} .

Figure 2.14b proves that the partial mismatch between prediction and experimental results shown in figure 2.6a is exclusively due to a geometric effect which unavoidable unless by changing the testing technique.

Chapter 3

Glass transition temperature versus structure of polyamide 6: a flash-DSC study

Abstract

The glass transition temperature (T_g) is a crucial parameter for understanding the mechanical behavior of polyamide 6. It depends mainly on two aspects: hydration level and processing, i.e. the thermal history and the flow conditions. In this work, the effect of the thermal history on T_g was investigated by means of fast scanning calorimetry (flash-DSC). Two different solidification procedures were studied; isothermal crystallization and continuous cooling were performed at different temperatures and rates respectively. The procedures have led to two contradictory trends of glass transition evolutions when related to their crystallinity fraction. The concept of rigid amorphous phase is used. This is considered as a part of the amorphous phase with a lower mobility, present at the inter-phase between crystals and bulk amorphous (mobile amorphous fraction). The analysis leads to the conclusion that the thermal history affects the ratio between rigid and mobile amorphous phases and it is this ratio that determines the glass transition temperature of dry polyamide 6.

3.1 Introduction

Polyamide 6 (PA6) is an engineering polymer, commonly known as "Nylon 6", which is used in the field of load-bearing applications where mechanical performance and lifetime are keywords. Applications such as under-the-hood components and sport items are often exposed to demanding conditions like high load, challenging temperature regimes and elevated relative humidities. However, the performance of PA6 (and also most other polymers) depends strongly on micro-structural details (such as crystallinity, lamellar thickness, phase content, etc.) that, to a great extent, are determined during processing. Therefore, it is obvious that an investigation of the influence of processing on properties is required to predict and improve the performance.

PA6 belongs to the family of aliphatic polyamides. Its monomer has two polar groups; the amide and carbonyl groups. These polarities can form hydrogen bonds between chains, leading to high strength [26]. However, this polar character causes a crucial characteristic of polyamide 6; hygroscopicity [27]. Indeed, if exposed to a humid environment, PA6 absorbs water till reaching a saturation level which is dependent on temperature and relative humidity [16]. If this occurs, part of the hydrogen bonds are broken and new H bonds are formed with the water molecules [12]. This phenomenon is called plasticization and results in a depression of the glass transition temperature [8]. The plasticization causes a considerable deterioration of the mechanical properties, as shown by a number of authors in literature [14, 28–30]. Therefore, it is clear that the glass transition temperature is an important parameter for PA6 properties. However, the glass transition temperature of PA6 not only depends on the hydration level; it also changes with crystallinity [51, 52], amorphous orientation [13, 52] and, as more recently reported, with the rigid amorphous phase content (RAF) [53, 54]. An illustrative example of the influence of processing on the glass transition is given in figure 3.1, where the storage modulus (E') is displayed as a function of temperature for three samples produced with three different thermal histories. The drop in the modulus due to the glass transition is different for the three samples, and also the value of T_g changes. In order to understand how processing affects the glass transition, we will use a model that describes a semi-crystalline polymer as a system composed by three phases: the crystalline phase, the rigid amorphous (RAF) and the mobile amorphous phase (MAF). The main difference is in the molecular mobility, the highest mobility belongs to the mobile amorphous phase, the lowest to the crystalline domains and the rigid amorphous phase has an intermediate mobility [54–56]. The rigid amorphous phase, as assumed in this model, is a sort of inter-phase between the crystalline and the mobile amorphous phase. This concept was employed also to other systems [57–59]. Many experimental techniques are used, but the most common one is the traditional differential scanning calorimetry (DSC), focusing on the change of specific heat capacity due to the glass transition. From this it is possible to estimate the amount of amorphous phase that did not transform to the rubbery state during the glass transition. This excess of amorphous phase

is defined as the rigid amorphous phase. Fast scanning calorimetry (flash-DSC) allows us to investigate a wide range of cooling rates and cooling procedures that are not achievable by traditional DSC. This gives the possibility to a) get completely amorphous samples, b) perform real isothermal crystallization and c) suppress cold crystallization upon heating.

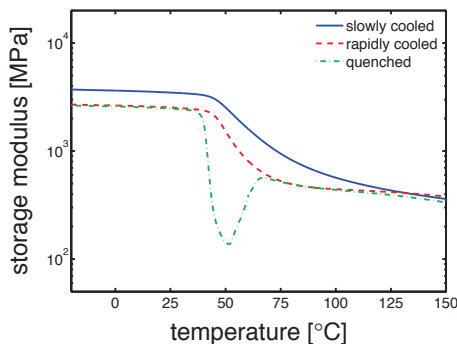


Figure 3.1: Dynamical mechanical thermal experiments of samples with different thermal history. Heating rate $3^{\circ}\text{C}/\text{min}$, frequency 1Hz, dry samples.

The difference in figure 3.1 are typically caused by processing-induced differences in structure. An important characteristic of PA6 is its polymorphism; there are two important crystal forms with respect to melt processing: the most stable α -phase (monoclinic cell) for low under-cooling or high isothermal crystallization temperature, and the less stable γ -mesophase (pseudo-hexagonal cell) for high under-cooling or medium to low isothermal crystallization temperatures. In case of very fast cooling also a completely amorphous sample can be obtained [7]. Mileva *et al.* [60], have shown that melt-crystallization at low under-cooling is connected with the formation of lamella, also for the γ -mesophase, while high under-cooling leads to γ -mesophase with a nodular morphology for which no lamella can be observed. The aim of this work is to investigate the structure formation in PA6 for a wide range of cooling procedures and conditions mainly by means of fast scanning calorimetry, in order to determine the relation of the glass transition temperature with the structure, i.e. the amount of crystalline phase, MAF and RAF. This will form the basis for future works on mechanical properties for which T_g is a crucial parameter.

3.2 Experimental

3.2.1 Materials

The material employed in this work was polyamide 6 (Akulon K122) provided by DSM (The Netherlands). This PA6 has a viscosity-average molar mass (M_v) of about 24.9 kg/mol.

3.2.2 Differential scanning calorimetry

Two different DSC apparatus were used. A traditional DSC and two flash-DSC's. The conventional DSC was a Mettler-Toledo 823e/700 module with a Cryostat intra-cooler; one flash-DSC was a Metler Toledo flash-DSC 1 equipped with a Huber TC100 intra-cooler, the other one was a special flash-DSC setup for in-situ X-ray. Experiments were carried out using 50 μ l aluminum pans and UFS1 sensors for DSC and flash-DSC respectively. Moreover, in all DSC's experiments were performed under a constant flow of dry nitrogen.

Sample preparation

In the case of conventional DSC, the samples were obtained by cutting pellets in pieces with a mass between 5 and 10 mg that were placed in the aluminum pans. For the ultrafast DSC, tiny pieces of approximately 100ng were cut and put onto the sensor by the use of an eyelash.

Estimation of sample mass (flash-DSC)

In order to estimate the sample mass, the same thermal effect was measured by traditional and ultrafast DSC. A sample with measurable mass was cooled at 20°C/min and heated at 20°C/min in the conventional DSC. From this experiment, the "specific" melting enthalpy (Δh_m), for the crystallinity obtained at the chosen cooling rate, was determined by peak integration. Subsequently, a sample of unmeasurable mass was cooled at 20°C/min and heated at 1000°C/s in the flash-DSC. From the heating curve, the melting enthalpy (ΔH_m) was determined. Finally, the sample mass was determined from:

$$m = \frac{\Delta H_m}{\Delta h_m} \quad (3.1)$$

Methods

In this work, conventional DSC was used solely for the determination of flash-DSC sample mass. Two different solidification methods were investigated, namely continuous cooling and isothermal crystallization. In order to get a well defined and comparable T_g, the standard continuous cooling is actually replaced by a so called "two step continuous cooling" where the cooling rate with which T_g is passed is kept constant. This is explained in detail in Appendix A. In order to have an absolutely identical condition from which the experiment could start, every experiment was preceded by a condition cycle, see Appendix B,

The two step continuous cooling procedure starts from a molten sample at 300°C, followed by cooling at several speeds (in a range from 0.1 to 1000°C/s) up to 100°C after which the cooling rate is switched to 1000°C/s to -50°C. Subsequently, the samples is heated at 1000°C/s up to 300°C. The isothermal crystallization method, see figure 3.2b, starts from the molten state at 300°C as well. The chosen isothermal temperature is reached by cooling at 1000°C/s, a

rate that is fast enough to avoid crystallization during cooling. Next, the temperature is kept constant for 180s. This time is sufficient to complete the crystallization process. Completion of the crystallization process means that the full volume of the sample has been converted in a semi-crystalline state, i.e. a mixture of ordered (lamella) and amorphous material. The amount of crystal material is called the degree of crystallinity (X_c). The fraction of semi-crystalline material is called the space filling (ξ), completion means $\xi=1$. The crystallinity for a specific space filling ξ is given by:

$$X_c = \xi \cdot X_{C\infty} \quad (3.2)$$

where $X_{C\infty}$ is the maximum crystallinity at the completion of space filling. For high enough temperatures, this maximum crystallinity can increase by perfectioning of the crystals (secondary crystallization), i.e. $X_{C\infty}(T,t)$. Space filling and (final) crystallinity depend both on cooling rate (continuous cooling) and on the crystallization time and temperature (isothermal crystallization). For example, fast cooling and short crystallization times will cause incomplete space filling, a low crystallization temperature with sufficient time will lead to lower crystallinity levels $X_{C\infty}$ while space filling $\xi=1$. After crystallization, the sample is cooled down to -50°C at 1000°C/s . Finally, heating up to 300°C at 1000°C/s is performed. The final heating run is used to retrieve the characteristics, such as glass transition temperature, crystallinity and heat capacity.

In order to study the case of isothermal crystallization with space filling lower than 1, isothermal crystallization were performed at 90 and 180°C varying the duration of the isothermal segment.

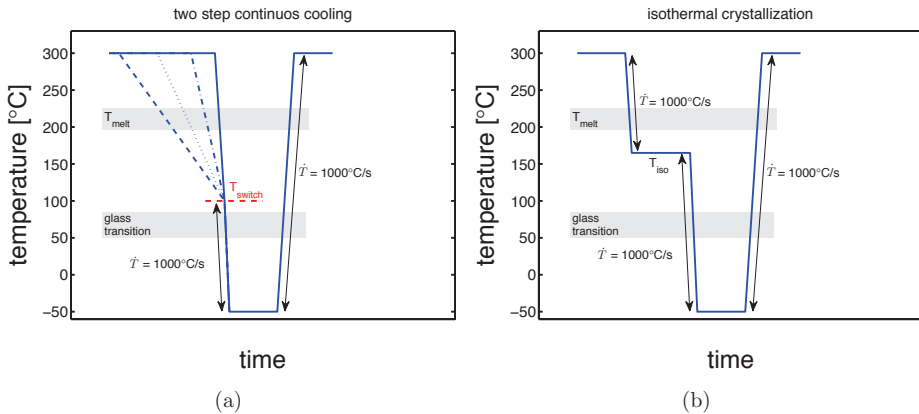


Figure 3.2: a) Two step continuous cooling and b) isothermal crystallization procedures. The segment length in the x-axes (time) is not realistic.

Analysis

The glass transition temperature was determined by estimating the midpoint in proximity of the change in specific heat (ΔC_p). Lines tangential to the $C_{p,solid}$, $C_{p,liquid}$ and the transient in between were drawn, see figure 3.3a. The intersections between $C_{p,solid}$, $C_{p,liquid}$ and transient are defined as T_g onset and T_g end-set respectively. The midpoint of the segment between T_g onset and T_g end-set was defined as the glass transition temperature, as shown in figure 3.3a. The crystallinity degree was calculated by:

$$X_c = \frac{\Delta H_m}{\Delta H_f^0} \quad (3.3)$$

where ΔH_f^0 is the thermodynamic fusion enthalpy (241 J/g for the α -phase [21] and 58 J/g for the γ -mesophase [61]) and ΔH_m is the integral of the observed melting peak, as shown in figure 3.3b.

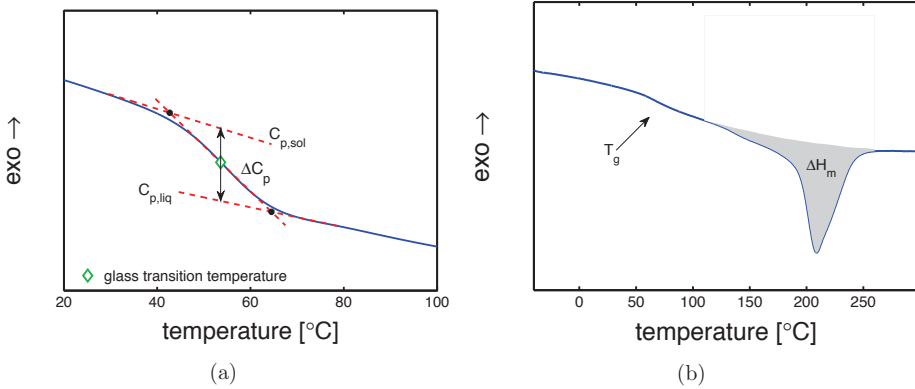


Figure 3.3: Example of a) glass transition temperature definition and ΔC_p determination and b) crystallinity estimation.

Unfortunately, estimating the crystallinity is not always possible. In fact, despite high heating rate (1000°C/s), when starting from γ -mesophase in the solid state, partial melting and re-organization in the more stable α -phase will take place. Thus, the measured melting area would not be related to only the pre-existing crystallinity but also to the heat necessary to melt the transformed fraction of crystals. This fraction cannot be estimated from the DSC measurements. Therefore, also in-situ wide angle x ray diffraction (WAXD) experiments were carried out on samples on the flash-DSC sensor for several solidification procedures. The crystallinity (χ_c) obtained by WAXD was subsequently used for the structural analysis (details about this procedure are explained in section 5.3.5 and Appendix C).

The estimation of the mobile amorphous fraction (MAF) is based on the ratio:

$$MAF = \frac{\Delta C_p}{\Delta C_{p_{am}}} \quad (3.4)$$

where ΔC_p is the measured variation of heat capacity during glass transition and $\Delta C_{p_{am}}$ is related to a completely amorphous sample as already proposed by [62–64]. Therefore, imposing the following statement:

$$1 = RAF + MAF + X_c \quad (3.5)$$

the rigid amorphous fraction can be calculated by:

$$RAF = 1 - (MAF + X_c) \quad (3.6)$$

Notice that we do not study the evolution of the structural parameters but we focus on the resulting values for a wide variety of thermal histories. Such an in-depth study is beyond the scope of this work. Examples of such studies can be found in [65, 66].

3.2.3 X-ray diffraction

Wide angle x-ray diffraction (WAXD) experiments were carried out in situ on the samples on the sensors during fast-scanning calorimetry experiments. The choice of an in-situ technique was crucial because of the hydrophilic nature of PA6, as explained in section 3.1. With ex-situ experiments, the sample would uptake water, decrease its T_g (even below room temperature) and therefore, crystallization at room temperature may occur. It is important to point out that the saturation time scales inversely with the sample size; thus, a sample size in the order of hundreds micron lead to saturation in a matter of minutes. These experiments were performed at the European Synchrotron Radiation Facility (ESRF) of Grenoble in France, at the Dutch-Belgian beamline 26 (DUBBLE). An innovative setup able to allow fast-scanning calorimetry with in-situ x-ray was used, this setup is extensively described in [67]. In this work, the samples were not irradiated with x-ray during the whole thermal protocol. Only at the end of each solidification procedure (at room temperature) patterns were taken with an exposition time of 15 seconds. After normalization, the crystallinity was estimated by subtracting the amorphous halo (experimentally obtained). Finally, the degree of crystallinity is calculated by:

$$\chi_c = \frac{T - A}{T} \quad (3.7)$$

where T is the total scattered intensity and A is the scattering from the amorphous halo. Also small angle X-ray scattering was performed on flash-DSC sensor (ex-situ). Lorentz [68] and thermal density fluctuation [69] correction were applied to the pattern. Thus, the peak position of the SAXS pattern (d^*) is used to define the long period (l_b):

$$L_b = \frac{2\pi}{d^*} \quad (3.8)$$

which is used to estimate the average lamellar thickness:

$$l_c = \chi_c \cdot l_b \quad (3.9)$$

where l_b is the long period and χ_c is the crystallinity. Ex-situ experiments were performed only in the case of isothermal crystallization, where full space filling was reached and therefore the influence of hydration on structure development is minor.

3.3 Results and discussion

Two illustrative results of this study are given in figure 3.4. The solidification procedures are compared; in figure 3.4a the two step continuous cooling and in figure 3.4b isothermal crystallization. Both show a clear influence of solidification parameters on the glass transition temperature. In figure 3.4a two heating curves, related to samples cooled with different cooling rates, show two main differences a) melting occurs only for the slow cooled samples and b) the glass transition temperatures are different. Figure 3.4b shows the results for samples that are crystallized isothermally. Again a clear difference in melting behavior is observed. This is related to crystallization of different crystalline phases as demonstrated by, for example, van Drongelen *et al.* [70]. Again, differences in glass transition temperatures are found.

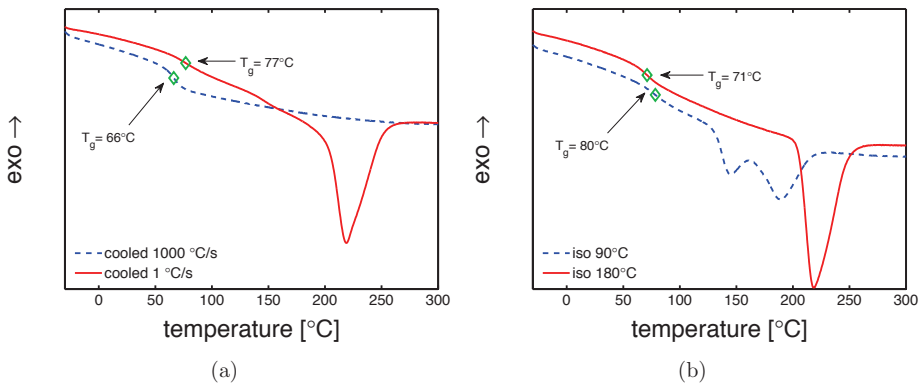


Figure 3.4: Heating at 1000°C/s of samples crystallized a) upon continuous cooling and b) isothermally (to improve clarity, the curves are shifted vertically).

The crystallinity values are derived from the patterns shown in figure 3.5 applying the X-ray analysis explained in Appendix C and section 5.3.5. The WAXD analysis also gives information about the crystallographic phase obtained by several solidification procedures. As far as the two step continuous cooling is concerned, a completely amorphous sample was obtained by very fast cooling at 200°C/s; at 75°C/s a weak γ -form characteristic reflection

was found; with a cooling rate of 5 and 2.5°C/s a predominance of the γ -form reflection with α -phase shoulders was observed; for very slow cooling (0.1°C/s), only α -phase reflections were observed, see figure 3.5a. In the case of isothermal crystallization, at low temperature (90°C) only the γ -form reflection was found, for temperatures between 120 and 170°C the γ characteristic reflection is predominant and rather weak α -phase shoulders were observed; at 180°C only the α -phase characteristic reflections were found, see figure 3.5b.

First the influence of cooling rate and isothermal temperature on the a) crystallinity (figure 3.6) and b) glass transition temperature (figure 3.7) will be presented. In figure 3.6a, the overall crystallinity obtained by two step continuous cooling is reported as a function of the initially applied cooling rate. As expected, cooling rates higher than $\approx 100^\circ\text{C/s}$ lead to a completely amorphous sample while for cooling rates lower than 100°C/s , a rapid increase of crystallinity is observed up to a maximum value of about 37% (a clear plateau in crystallinity was not reached because of the impossibility to perform experiments with cooling rate slower than $\approx 0.1^\circ\text{C/s}$). Upon isothermal crystallization for temperatures between 90°C and 180°C , a rather slight increase in crystallinity is found from about 30% at the lowest T_{iso} of 90°C up to 36% at the highest T_{iso} of 180°C , see figure 3.6b.

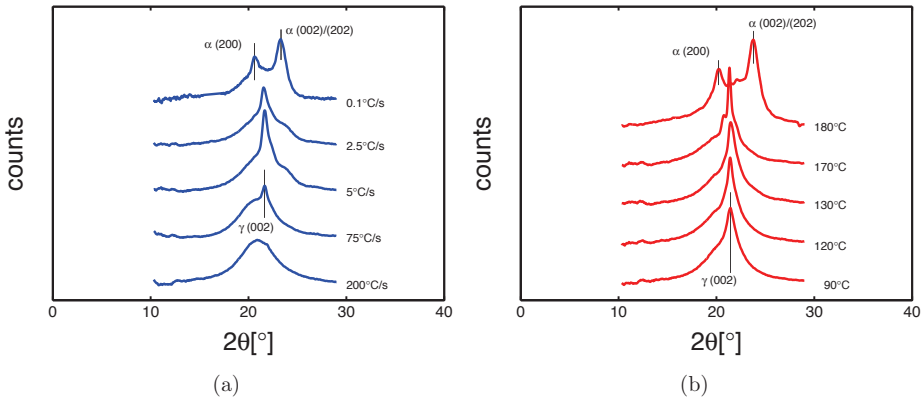


Figure 3.5: Wide angle x-ray patterns regarding samples obtained by a) cooling at several applied cooling rates and b) crystallization at different isothermal temperatures.

Plotting the glass transition temperature as a function of applied cooling rate a minimum ($\approx 66^\circ\text{C}$) is found for the higher cooling rates where the samples are completely amorphous, and a maximum ($\approx 77^\circ\text{C}$) for the lower cooling rates where crystallinity is the highest. Similar to crystallinity, T_g also increases with the decreasing cooling rate. In the case of isothermal crystallization (figure 3.7b), the glass transition shows a monotonic decrease.

Next, the correlation between structural parameters and T_g is investigated. In figure 3.8 the glass transition is plotted as a function of crystallinity. In the case of continuous cooling,

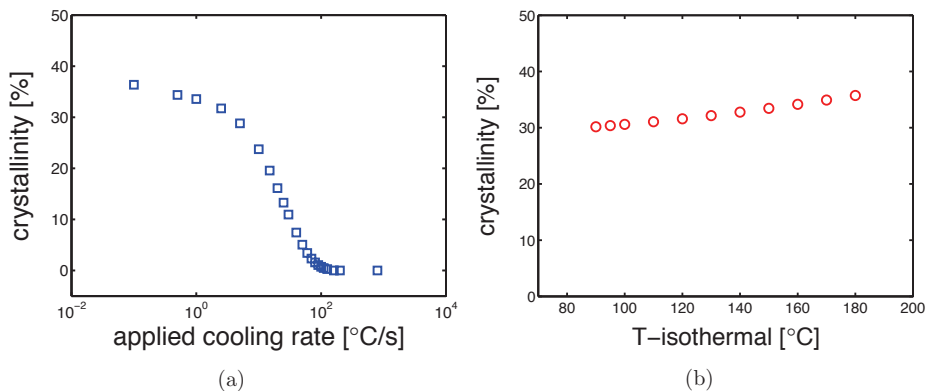


Figure 3.6: Overall crystallinity obtained by X-ray measurements of samples crystallized upon (a) several applied cooling rate and (b) different isothermal temperatures.

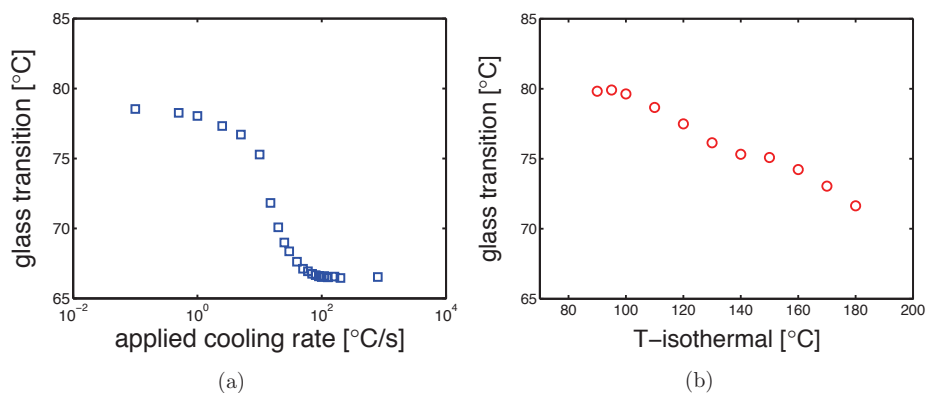


Figure 3.7: Glass transition temperature obtained a) upon solidification at several applied cooling rates and b) crystallization at different isothermal temperature.

the highest T_g corresponds to the highest crystallinity and the increase of glass transition is close to proportional with crystallinity. In contrast, the isothermal crystallization displays a totally different scenario; the glass transition temperatures measured in the case of isothermal crystallization is opposite to what is observed from continuous cooling. This is the first clear sign that crystallinity is not a determining parameter for the glass transition temperature, in contrast to what previously proposed by [51, 52]. In the following we will present a concept that explains these results and, moreover, a rather simple model that can capture them and predict the T_g as a function of structural parameters that, again, are determined by the thermal history.

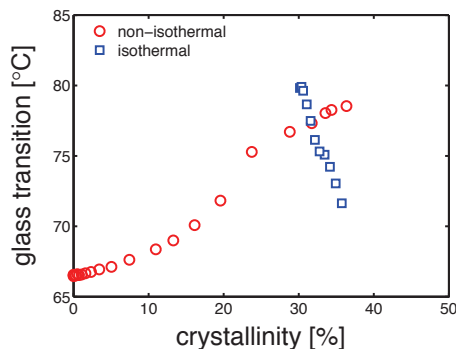


Figure 3.8: Glass transition temperature as a function of overall crystallinity obtained upon continuous cooling and isothermal crystallization.

Next, a phase composition analysis was performed in order to investigate the influence of the solidification procedure on the RAF, MAF and crystallinity content. In figure 3.9a the fraction of rigid amorphous phase, mobile amorphous phase and crystallinity are presented as a function of applied cooling rate. When completely amorphous samples are obtained, the rigid amorphous fraction (RAF) and crystallinity (χ_c) are both zero while the mobile amorphous fraction (MAF) is stable at 1. For cooling rates between about 10 and 90°C/s, both crystallinity and RAF increase rapidly, while MAF decreases. For even lower cooling rates, the rigid amorphous fraction appears to be rather stationary while the mobile amorphous fraction keeps on decreasing slightly. Figure 3.9b shows the case of isothermal crystallization. In this case, only temperatures leading to complete space filling were selected. In fact, the maximum MAF estimated is about 0.5 for crystallization at 180°C where the crystallinity is the highest and RAF the lowest. Moving towards lower isothermal temperatures, crystallinity slowly decrease and, at the same time, the mobile amorphous fraction decreases and the rigid amorphous increases till a maximum at 90°C.

By comparing figures 3.7 and 3.9, it is observed that the glass transition follows a similar trend as the rigid amorphous fraction; opposite to the one observed for the mobile amorphous fraction. This observation is made for both, continuous cooling and isothermal crystallization.

Figure 3.10a shows the glass transition temperature as a function of mobile amorphous fraction for samples solidified by continuous cooling and by isothermal crystallization while in figure 3.10b the glass transition temperature is plotted as a function of the rigid amorphous fraction. These two figures demonstrate that, although not perfectly, both solidification procedures give a similar trend for T_g if plotted as a function of RAF or MAF. This is, an indication that structural investigation are crucial to understand the glass transition in PA6.

In order to understand the role of crystallinity for a given crystallization temperature (T_{iso}), isothermal crystallization at 90 and 180°C were performed varying the isothermal

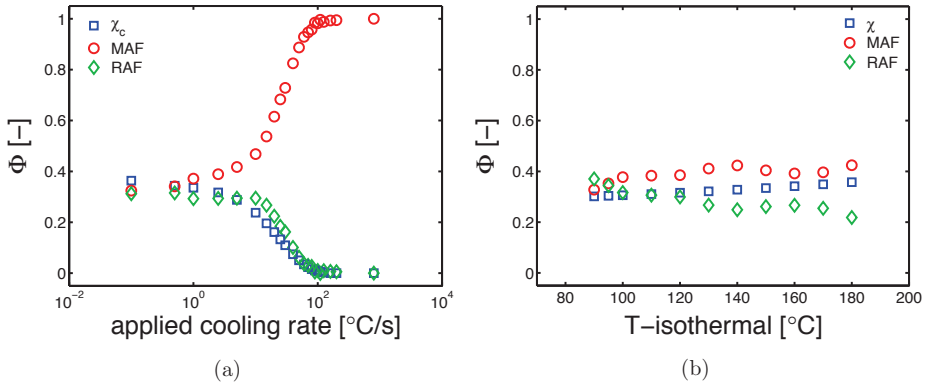


Figure 3.9: Phase composition as a function of a) applied cooling rate and b) as a function of isothermal temperature of crystallization.

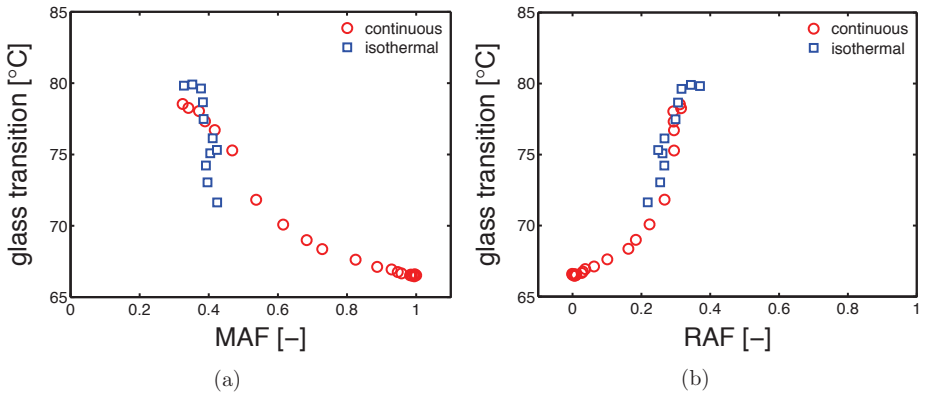


Figure 3.10: Comparison between continuous cooling and isothermal crystallization, glass transition temperature as a function of a) MAF and b) RAF.

segment duration (t_{iso}).

In figure 3.11 the glass transition of samples crystallized at different T_{iso} and t_{iso} is plotted as a function of crystallinity. Remarkably a lower isothermal temperature lead to a higher T_g for the same fraction of crystallinity. Therefore, a phase composition analysis was performed and shown in figure 3.12. The fractions of RAF, MAF and crystallinity are plotted as functions of crystallization time, for the crystallization temperature at 90 and 180 $^{\circ}\text{C}$. From figure 3.12a and 3.12b, it becomes clear that these differences can be rationalized in terms of the RAF content. At lower crystallization temperature the resulting RAF content is higher.

In figure 3.13a and 3.13b comparisons between T_{iso} 90 $^{\circ}\text{C}$ and 180 $^{\circ}\text{C}$ are given. In this

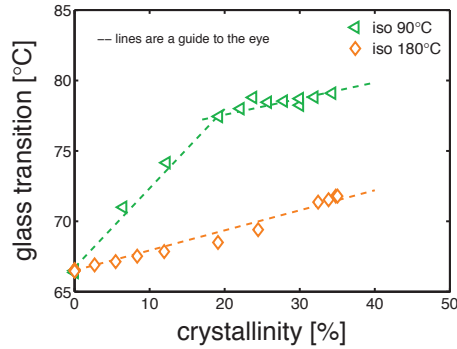


Figure 3.11: Glass transition temperature as a function of crystallinity in the case of isothermal crystallization at 90 and 180°C for several crystallization times.

case, MAF and RAF are plotted as functions of crystallinity; it is observed that RAF (MAF) increase (decrease) linearly with crystallinity. Two different slopes are observed for isothermal crystallization at 90°C (indicated with lines) and one for 180°C.

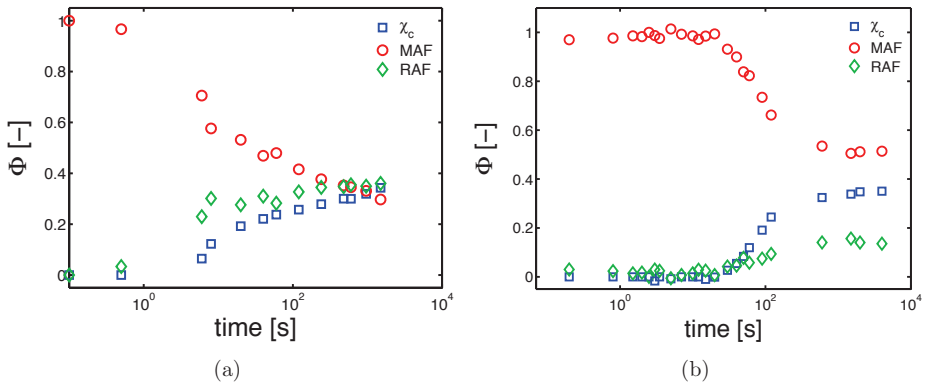


Figure 3.12: MAF, RAF and crystallinity as functions of time for isothermal crystallization at a) 90°C and b) 180°C.

3.3.1 Relations between phase contents

Some rather straightforward arguments are presented to capture the coupling between the different phases in a semi-quantitative way. This will help to understand and interpret the experimental results presented before. Starting point is the idea that RAF is a layer of changing mobility adjacent to the crystalline lamella, i.e. the amount of RAF is proportional

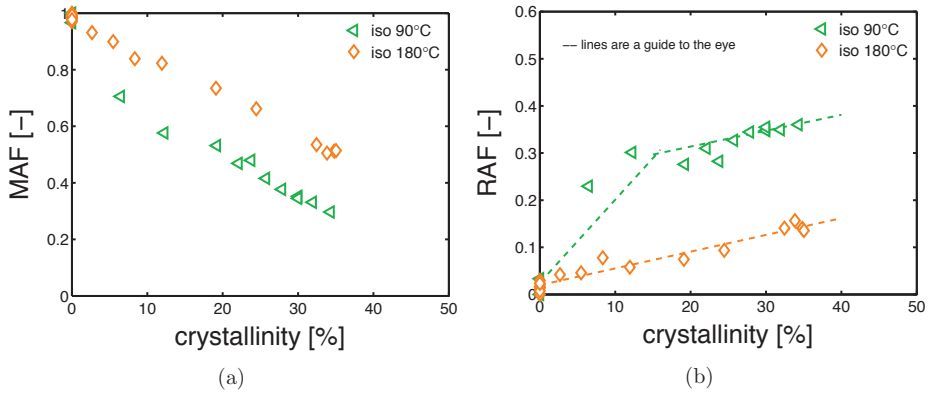


Figure 3.13: a) Mobile and b) rigid amorphous fractions as functions of crystallinity for different T_{iso} (90 and 180°C) and several t_{iso} .

to the face areas of the lamella, see figure 3.14.

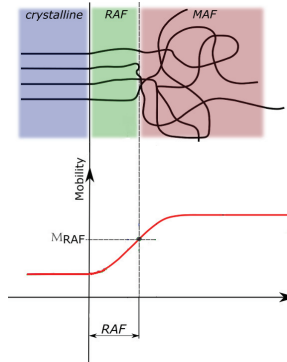


Figure 3.14: Schematics representing the definition of the rigid amorphous phase (RAF).

With the space filling given by ξ ($0 < \xi < 1$) and crystallinity level in the space filled by χ_∞ it follows that the crystallinity χ_c and the fraction of RAF in a volume V_0 are given by:

$$\chi_c = \xi \cdot \chi_\infty = \frac{\xi \cdot A_c \cdot l_c}{V_0} \quad (3.10)$$

$$RAF = \frac{2 \cdot \xi \cdot A_c \cdot l_R}{V_0} \quad (3.11)$$

in which A_c is the total lamellar face area in a volume V_0 , l_c the lamellar thickness and l_R the thickness of the RAF layer. For now, the thickness of the RAF layer is considered to

be (approximately) constant. It easily follows that:

$$RAF = \frac{2 \cdot \chi_c \cdot l_R}{l_c} = \frac{2 \cdot \xi \cdot \chi_\infty \cdot l_R}{l_c} \quad (3.12)$$

and with the basic relation $\chi_c + MAF + RAF = 1$ we get:

$$MAF = 1 - \chi_c \left(1 + \frac{2 \cdot l_R}{l_c} \right) = 1 - \xi \chi_\infty \left(1 + \frac{2 \cdot l_R}{l_c} \right) \quad (3.13)$$

First we will discuss some direct consequences and trends resulting from this model. For a constant crystallinity χ_c , the fraction of RAF goes up and for MAF goes down with decreasing lamellar thickness l_c . Moreover, this increase (decrease) is stronger for higher χ_c -values. For isothermal crystallization the lamellar thickness l_c is directly related with the crystallization temperature, i.e. a higher crystallization temperature leads to higher MAF values at equal χ_c -values. In the same way, using the expression for the RAF content, it is found that, for isothermal crystallization, the RAF content is higher for lower crystallization temperatures at equal χ_c -values. For isothermal crystallization with completed space filling, see figure 3.9b, the final crystallinity χ_∞ varies with crystallization temperature; a higher T_{iso} (T_c) means more mobility and thus more perfect crystals and a higher crystallinity. From equations 3.12 and 3.13 it follows, when considering crystallinity only, that MAF and RAF should decrease and increase, respectively. However, the opposite is observed. This is due the dominant role of the varying lamellar thickness.

It is clear that knowledge of the lamellar thickness is crucial and, therefore, this was separately measured for the case of isothermal crystallization only by means of ex-situ SAXS. Results are shown in figure 3.15a. For the non-isothermal experiments the crystallization-peak was defined as the (average) crystallization temperature, see figure 3.15b. Using interpolation of the isothermal results for l_c versus T_c , the l_c -values for the non-isothermal experiments were estimated; see again figure 3.15a. As mentioned in section 3.1, crystallization of γ -mesophase at high under-cooling leads to a non-lamellar morphology; thus, l_c values obtained at temperatures below 130°C should be interpreted as crystal thickness rather than lamellar thickness [60].

With a full model for the crystallization kinetics, including secondary crystallization, and the relation between crystallization temperature(s) and lamellar thickness it would be possible to predict the the MAF and RAF content for a given thermal history. However, the formulation and experimental validation of such a model is outside the scope of this paper. Instead we will use the experimentally measured space filling and the estimates for the final crystallinity levels to give predictions for the MAF and RAF contents for the whole range of experimental conditions.

The results from isothermal crystallization for two crystallization temperatures (90 and 180°C, see figures 3.12 and 3.13) and different crystallization times are discussed first. Values given below are estimates from these figures. Three regimes can be observed: regime I)

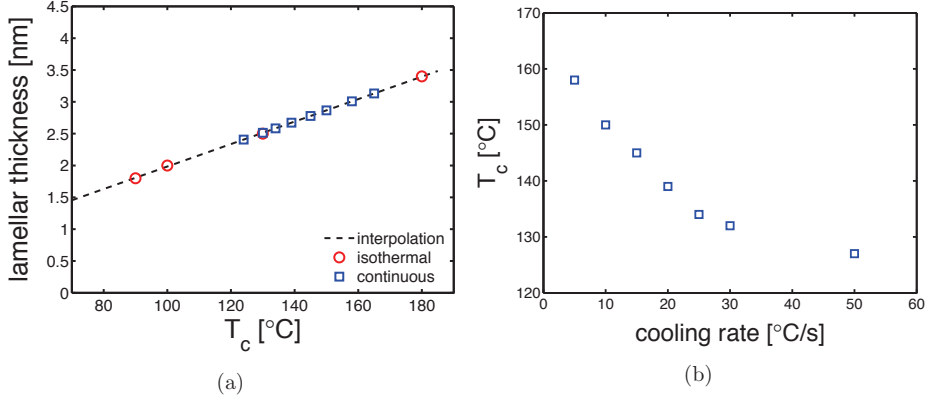


Figure 3.15: a) Lamellar thickness as a function of crystallization temperature. The red circles are experimental results obtained by ex-situ X-ray experiments on the flash-DSC chips; the blue squares are estimations of lamellar thickness obtained by matching the interpolation (dashed black line) of the experimental results and the measured crystallization temperatures in figure 3.15b, in the case of continuous cooling. b) Crystallization temperature as a function of cooling rate; the blue squares are experimental results whereas the green diamond is an extrapolated T_c .

for too short times no observable crystallinity is found ($t_{iso} < 8s$ for $T_{iso} \approx 90^\circ C$, $t_{iso} < 20s$ for $T_{iso} \approx 180^\circ C$), regime II) crystallization with growing space filling and RAF-fraction ($1s < t_{iso} < 8s$ for $T_{iso} \approx 90^\circ C$, $20s < t_{iso} < 120s$ for $T_{iso} \approx 180^\circ C$). The crystallinity χ_∞ at space filling $\xi=1$ estimated to be ≈ 0.15 and ≈ 0.3 for $T_{iso}=90$ and $180^\circ C$, respectively. Finally, regime III) crystallinity increases further while the RAF becomes approximately constant, i.e. χ_∞ increases to its maximum that is in the order of ± 0.3 . The average lamellar thickness for these two crystallization temperatures is ≈ 1.8 and 3.4 nm, respectively (see figure 3.15a). Using the numbers at the end of regime II) in equation 3.12 it follows that the thickness of the RAF layer is about 1-1.15 nm where the higher value is found for the lower temperature. This small difference in RAF layer thickness could be related to the freezing of lower mobility at a lower crystallization temperature. More important is the observation of a much higher RAF content for $T_{iso}=90^\circ C$ compared to the results for $T_{iso}=180^\circ C$, while the crystallinity values χ_c show the opposite. This is rationalized by equation 3.12: the large difference in the lamellar thickness over-compensates the difference in crystallinity. Moreover, in regime III) crystallinity can still grow via crystal perfectioning, i.e. lamellar thickening, while RAF does not hardly change since χ_∞ and l_c are proportional, see eq. 3.10. This is most clear for $T_{iso}=180^\circ C$ while for $T_{iso}=90^\circ C$, where less perfect crystals are grown, also some new lamella could be created and thus some new surface for RAF. However, this effect is small.

Using the estimated value $l_R=1.1$ nm, interpolated values for the measured crystallinity chi_c (see figure 3.6b) for isothermal crystallization for 180s for which the space filling $\xi=1$

and the lamellar thickness given in figure 3.15a, the MAF and RAF fractions are calculated over the whole range of temperatures by applying equations 3.12 and 3.13. The results are presented in figure 3.16 and they show a clear match between the experimental and the model results (the line for χ_c is the interpolation line). Notice that in figure 3.9b and 3.16 the trend for the crystallinity is smooth while the MAF and RAF show a slight change in the slope at $T_{iso} \approx 145^\circ\text{C}$. This could be related to the presence of a fraction of α -phase that increases with crystallization temperature (see also figure 3.5) and, therefore, indicate that polymorphism might play a role. However, these results are not strong and convincing enough to include such a more detailed concept in our model. For varying isothermal crystallization times for the case of isothermal crystallization, space filling ξ varies from 0 to 1. The range where $\xi=0$ or $\xi=1$ correspond to $\chi_c=0$ and $\chi_c=\chi_\infty$, respectively. The transition between these two regions is captured by a descriptive auxiliary function:

$$\xi = (c_1 - c_2) \cdot \left(1 + (r_0 \cdot (\log(x) - c_3))^{r_1}\right) \frac{(r_2 - 1) + c_2}{r_1} \quad (3.14)$$

in which the parameters have no physical meaning, the values are chosen such that the desired smooth transition is obtained and x is the time.

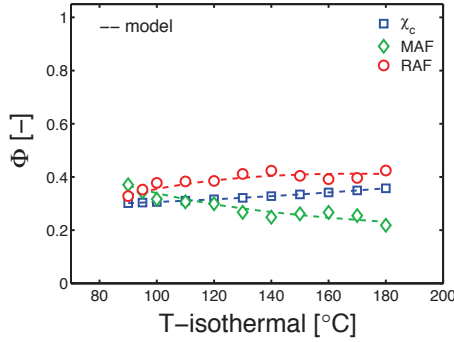


Figure 3.16: Crystallinity, MAF and RAF as a function of isothermal temperature; comparison between experimental (markers) and model results (dashed lines). Parameter: $l_R=1.1\text{nm}$.

The lamellar thickness was assumed to be constant, at $l_c=1.7\text{ nm}$ for 90°C and $l_c=3.4\text{ nm}$ for 180°C . Figures 3.17a and 3.17b give the results for $l_R=1.1\text{ nm}$. Clearly the trends are captured quite well but the final levels of the MAF and RAF fractions are off. By adjusting the RAF-layer thickness $l_R=0.8\text{ nm}$ the results look much better, see figures 3.18a and 3.18b. However, for the longer crystallization times ($t_{iso} > 180\text{s}$) the same l_R as for the isothermal experiments with varying T_{iso} and $t_{iso}=180\text{s}$ should be used.

Next, continuous cooling results are analyzed. These non-isothermal crystallization cases are rather complex. Crystalline structures are formed in a range of temperatures leading

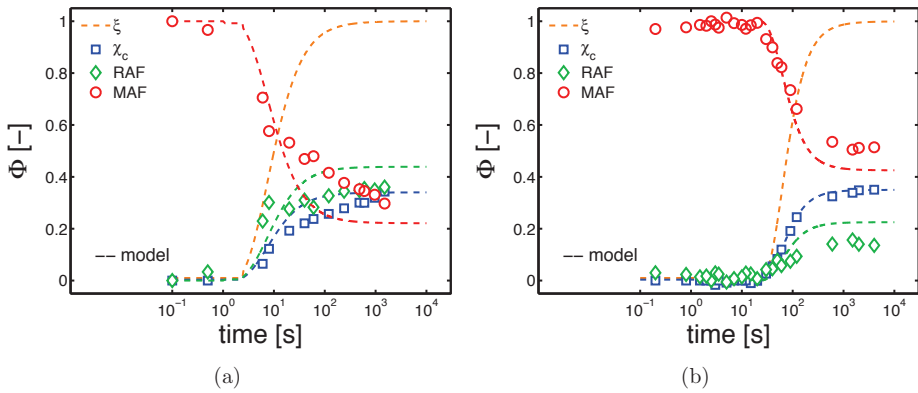


Figure 3.17: Crystallinity, space filling, MAF and RAF as a function of isothermal crystallization time; dashed lines are the results of the model and the markers are experimental results. a) Isothermal at 90°C, parameters: $l_R=1.1\text{nm}$, $\chi_\infty=0.34$. b) Isothermal at 180°C, parameters: $l_R=1.1\text{nm}$, $\chi_\infty=0.35$.

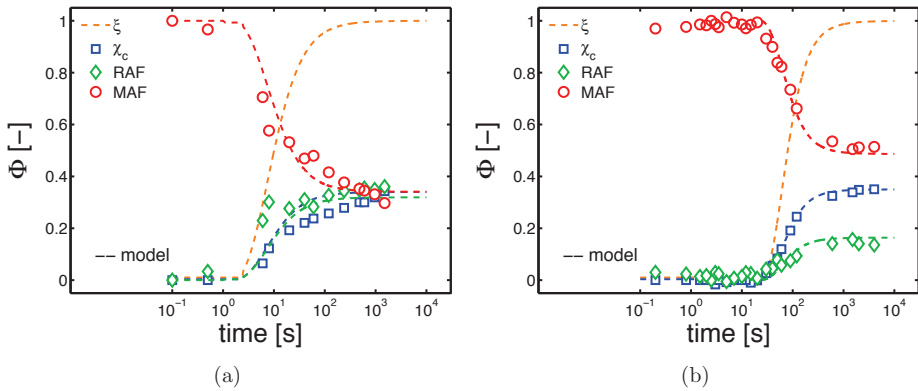


Figure 3.18: Crystallinity, space filling, MAF and RAF as a function of isothermal crystallization time; dashed lines are the results of the model and the markers are experimental results. a) Isothermal at 90°C, parameters: $l_R=0.8\text{nm}$, $\chi_\infty=0.34$. b) Isothermal at 180°C, parameters: $l_R=0.8\text{nm}$, $\chi_\infty=0.35$.

to a more broad distribution of lamellar thickness, new nuclei may occur during the cooling history and the spherulite growth rate varies. Moreover, similar to the varying isothermal crystallization time experiments, a range of cooling rates did not lead to complete space filling. Therefore, we use the auxiliary function (eq. 3.14) again, but now with the cooling rate as the argument. As mentioned before, the enthalpy-peak during crystallization was defined as average crystallization temperature, see figure 3.15b. This is only possible for a limited number of intermediate cooling rates. The corresponding lamellar thickness are

plotted in figure 3.15a. Clearly, full space filling, i.e. $\xi=1$, is obtained at a crystallinity higher than 0.2, from where on the RAF fraction is constant. The χ_∞ was chosen equal to the maximum crystallinity reached at the lowest cooling rate, $\chi_\infty=0.36$, from which the crystallinity is obtained with equation 3.2. As already discussed, the lamellar thickness could not be estimated along the full range of cooling rates; hence, the l_c values were obtained by interpolation over the full range of cooling rates, see figure 3.19b. Also in this case, the RAF thickness (l_R) is fixed at 1.1 nm.

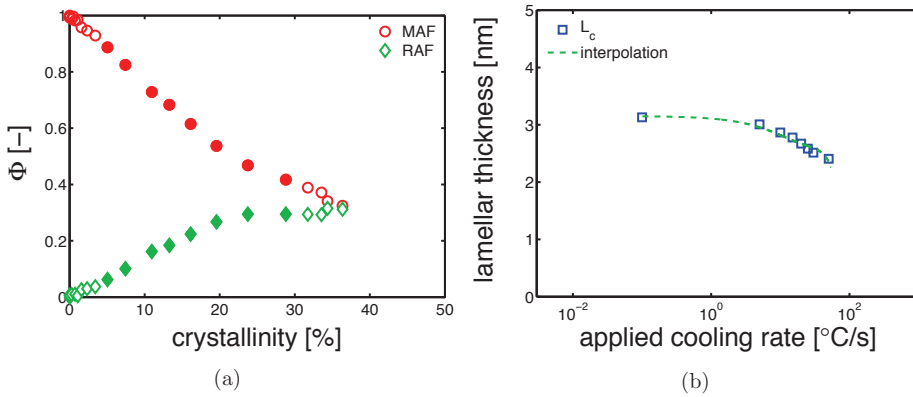


Figure 3.19: a) RAF and MAF content as functions of crystallinity in the case of two step continuous cooling. The solid markers are from the experiments for which an average crystallization temperature could be determined (see figure 3.15b). b) Lamellar thickness versus applied cooling rate, markers are the estimated L_c and the dashed line is the interpolation over the full range of cooling rates.

Figure 3.19a gives the MAF and RAF fractions as a function of the crystallinity for all continuous cooling rates. The results for which a crystallization temperature could be defined are indicated by solid symbols.

The results shown in figure 3.20 are quite reasonable; again, the trends are captured well but the final levels of the MAF and RAF fractions can be improved by varying one of the parameters. The RAF-layer thickness is not measured directly and the lamellar thickness is an estimated average value. The results improve by varying of l_R from 1.1 nm to 1.25 nm, see figure 3.21a, or decreasing l_c by multiplying with a factor 0.85 and keeping $l_R=1.1$ nm, see figure 3.21b.

These results show the potential of this model. However, the model could be improved by a further investigation of the non-isothermal crystallization case. In particular, the lamellar thickness distribution, which is expected to be broader in non-isothermal conditions; in fact, the low thickness part of the population would contribute to a higher RAF. Another aspect to investigate further is the RAF thickness (l_R). This effect is mimicked by decreasing l_c , see figure 3.21b. It seems reasonable to think that l_R is not really a constant but varies with the

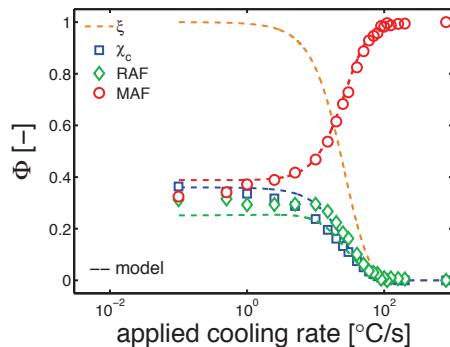


Figure 3.20: Crystallinity, space filling, MAF and RAF as a function of applied cooling rate; dashed lines are the results of the model and the markers are experimental results. Parameters: $l_R=1.1\text{nm}$, $\chi_\infty=0.36$.

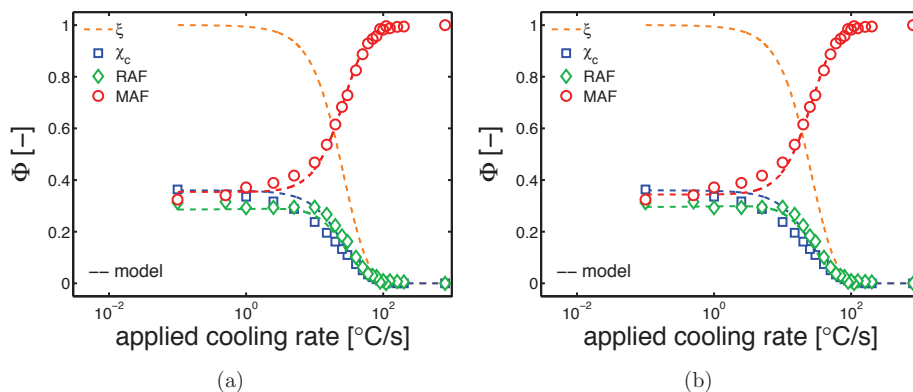


Figure 3.21: Crystallinity, space filling, MAF and RAF as a function of applied cooling rate; dashed lines are the results of the model and the markers are experimental results. a) Parameters: $l_R=1.25\text{nm}$, $\chi_\infty=0.36$. b) Parameters: $l_R=1.1\text{nm}$, $\chi_\infty=0.36$ and $l_c=l_c\cdot 0.85$.

temperature. However, these parameters are not easily achievable, in particular in the case of flash-DSC samples.

3.3.2 Relation between T_g and the RAF and MAF content

A relation between the glass transition temperatures T_g and the RAF and MAF content is proposed and compared with the experimental results for a range of crystallization conditions. A relation between the glass transition temperature and the RAF content was already reported in the literature for isotactic Polypropylene [71]. The starting point is the idea that, in the

case of pure RAF or pure MAF the material has a corresponding T_g , i.e. the $T_{g,RAF}$ or $T_{g,MAF}$, respectively. Note that pure RAF (or MAF) means that 100% of the amorphous phase is RAF (or MAF). For any crystallinity value χ_c , it is the ratio between RAF and MAF that determines the T_g . The simplest relation one can think of is a linear function between the two T_g 's. For a given χ_c the MAF varies between 0 and $1-\chi_c$ (RAF between $1-\chi_c$ and 0) while T_g is between $T_{g,RAF}$ and $T_{g,MAF}$. It easily follows that:

$$T_g = T_{g,MAF} + \frac{1}{1 + MAF/RAF}(T_{g,RAF} - T_{g,MAF}) \quad (3.15)$$

The value for $T_{g,MAF}$ is obtained from the experimental results (66.3°C) while the $T_{g,RAF}$ is used as the only fitting parameter, which correspond to 91°C. Note that this is not necessarily the actual $T_{g,RAF}$, whatever that might be, since RAF is not really a phase but rather represents a layer with a gradient in the reduced mobility. Figure 3.22a, 3.22b and 3.22c show the results; the model captures the experimental T_g results quite well. The standard deviation is 1.15°C.

Note that a model for the crystallization kinetics that includes the evolution of the distribution of the lamellar thickness is available, see for example Caelers *et.al.* [72]. Connecting such a model with the one presented in this study, will create the possibility of making a prediction of the T_g and this result can be used as input for deformation kinetics modeling that is used for lifetime predictions.

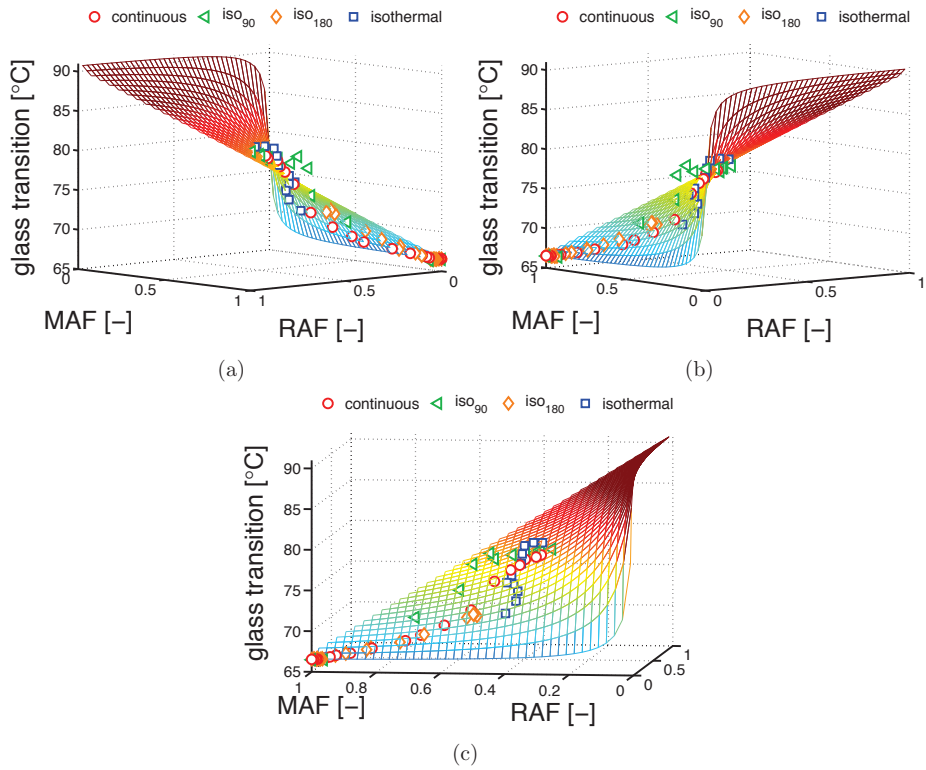


Figure 3.22: Overall overview of glass transition as a function of RAF and MAF in a 3D plot. The plane is the result of equation 3.15. Three views are shown.

3.4 Conclusions

In this work, the influence of thermal history on glass transition was investigated. The glass transition temperature was found to be not directly dependent on crystallinity whilst a clear relation with structures was established. In fact, the content of crystallinity, rigid and mobile amorphous phase for different cooling procedure were measured. A marked relation between glass transition and RAF-MAF content was found. More in particular, T_g is directly proportional to RAF and inversely proportional to MAF. This founding is also in agreement with the mobility scenario; indeed glass transition is a physical parameter strictly related to mobility, thus an high content of low mobility amorphous phase (RAF) would lead to high T_g . In the opposite case, a full mobile amorphous sample can only have a minimum value of glass transition temperature. The structural investigation led to deny any strict correlation between RAF-MAF content and the crystalline unit cell (as shown in 3.5a and 3.5b), as supported by X-ray experiments. Moreover, a model able to predict the structure development (RAF and MAF content) was proposed. Finally an equation able to predict the glass transition temperature as function of RAF-MAF content was presented.

3.5 Acknowledgments

This work is part of the Research Program of the Dutch Polymer Institute DPI, Eindhoven, the Netherlands, project number #786. The authors thank: Dr. D.Baeten (KU/Leuven) for the use of the fast-scanning calorimetry with in-situ x-ray setup; the Dutch-Belgian beamline (DUBBLE) at the ESRF facility in Grenoble (ESRF), in particular Dr. D.Hermida-Merino; Dr. M.van Drongelen (UT) for helping with the ex-situ small angle x-ray experiments on flash-DSC sensors.

Appendix A

As mentioned in section 3.1, the typical continuous cooling from melt to solid was replaced by a so called two step continuous cooling. This is due to the kinetic response of the ΔCp , which is a crucial characteristic in order to define the RAF and MAF content. In fact, as already proposed by [64], the change in heat capacity at glass transition temperature (ΔCp) varies for different applied cooling rate even if the same amount of crystalline phase is obtained and the probing heating rate is consistent. By performing typical continuous cooling experiments (i.e. cooling continuously from the melt to the solid passing through the glass transition region) at different cooling rates, not only crystallinity is varied but also the amorphous state is affected. The influence of applied cooling rate on ΔCp is attributed to a) change in crystallinity, b) variation of RAF-MAF content due to ageing and c) kinetic behavior. In figure 3.23a, a clear example of the applied cooling rate influence on amorphous state is given. In this case, two procedures are compared; two step continuous cooling (blue line) and continuous cooling (red line). In both the experiments, the cooling rate during crystallization is $1^\circ\text{C}/\text{s}$. In the case of two step continuous cooling, at 100°C the cooling rate is switched to $1000^\circ\text{C}/\text{s}$. As visible in 3.23a, the two experiments differ only in the change in C_p ; the crystallinity is exactly the same.

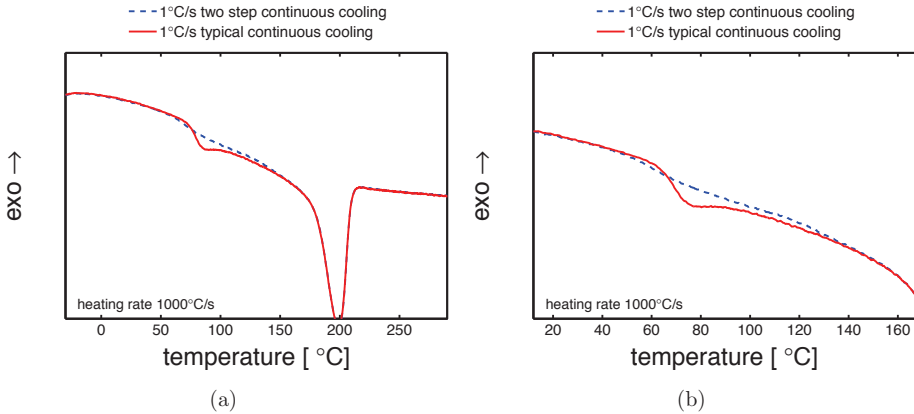


Figure 3.23: Comparison between two step continuous cooling and typical continuous cooling a) whole thermogram and b) magnification of the glass transition region.

Thus, by performing experiments with the same cooling rate before T_{switch} (e.g. $1^\circ\text{C}/\text{s}$) and varying the applied cooling rate after T_{switch} , we obtain substantial differences in change of heat capacity and glass transition, see figure 3.24a and 3.24b, respectively. In these experiments with fixed crystallinity, the variation of ΔCp and T_g might be attributed to the variation of RAF-MAF content due to ageing and kinetic behavior. Therefore, experiments

on completely amorphous samples were performed. In this case, only the kinetic behavior plays a role because only mobile amorphous phase is present. A decrease of ΔCp is observed for increasing applied cooling rate after T_{switch} , although smaller than the effect shown in figure 3.24a.

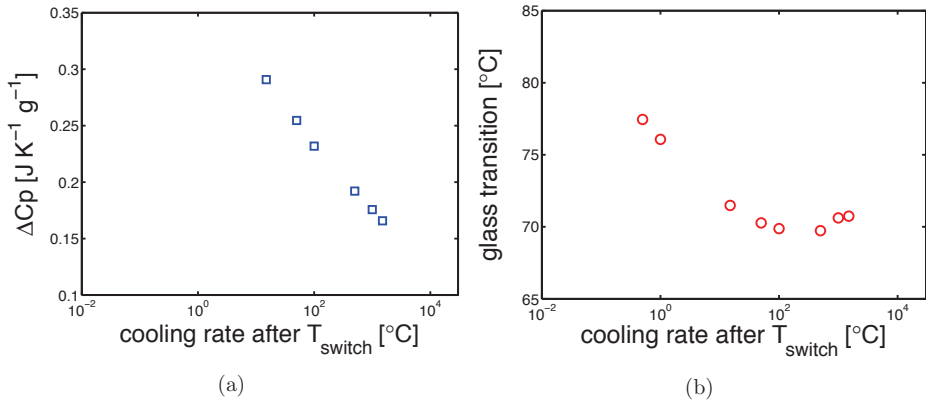


Figure 3.24: Effect of applied cooling rate after T_{switch} on a) change of heat capacity (ΔCp) and b) glass transition temperature; case of semi-crystalline sample, cooled at 1°C/s before T_{switch} .

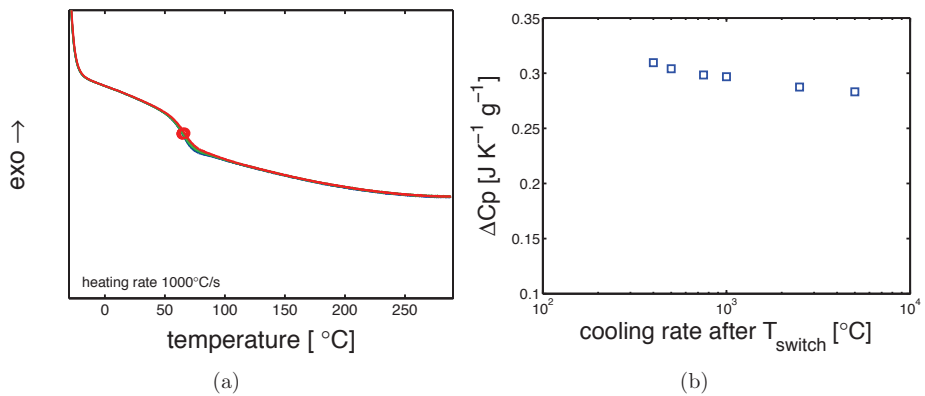


Figure 3.25: a) Heating of amorphous samples cooled at several different speeds after T_{switch} . b) Effect of applied cooling rate after T_{switch} on change of heat capacity (ΔCp); case of amorphous sample, cooled at 1000°C/s before T_{switch} .

In this section, the use of "two step continuous cooling" rather than typical continuous cooling was explained and justified. Indeed, this work was meant to investigate the influence of structure formation on the glass transition temperature and, therefore, this procedure was chosen to avoid influence of ageing and kinetics.

Appendix B

In this section, the conditioning procedure is described and justified. This procedure was applied for mainly two reasons: a) drying the sample and b) erase the thermal history. As explained in section 3.1, PA6 has a strong hydrophilic character which leads to water absorption. Moreover, the absorbed water acts as plasticizer and lowers the glass transition. The conditioning procedure is performed prior to each experiments. The procedure consist of two times heating at 1000°C/s followed by a short isothermal period at high temperature (300° for 1s) and quenching at 1000°C/s to -50°C , see figure 3.26. By applying this procedure, the thermal history is erased and the sample is dried thanks to the high temperature reached and the inert ambient (nitrogen).

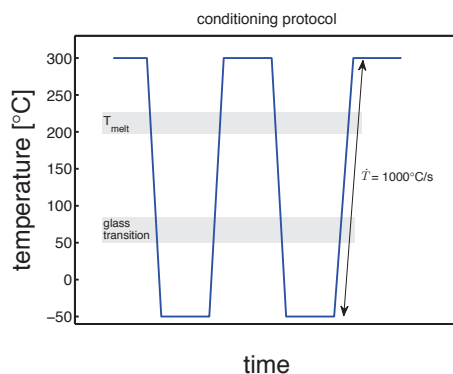


Figure 3.26: Conditioning procedure performed at the beginning of each fast scanning experiments.

Appendix C

The estimation of the crystalline fraction is a crucial part of this study. Indeed, because of possible re-organization and (or) phase transformations during heating, the enthalpy of fusion obtained for samples containing a mixture of γ -mesophase and α -phase can not be accurately deconvoluted to the pre-existing crystalline fraction. Unfortunately, this happens for most of the applied cooling rates and isothermal temperatures. Only in the extreme cases, where only γ -mesophase or α -phase exists, crystallinity can be estimated from the thermograms, i.e very low and very high isothermal temperatures (or cooling rates). Therefore, another technique must be used. Wide angle X-ray diffraction experiments were performed in-situ for several solidification procedures. An estimation of crystallinity was made for samples cooled at different cooling rates. In figure 3.27a, the crystallinity estimated by WAXD is compared with the few interpretable results obtained by flash-DSC (i.e. the experiment

with lowest cooling rate where only α -phase was obtained, and the measurements leading to completely amorphous samples). As is observed, the crystallinity onset resulting from the values obtained by WAXD (green markers in figure 3.27a) takes place at cooling rate higher than the onset obtained with flash-DSC results (blue markers). In 3.27b four cooling thermograms are compared. The blue (dashed) and red (solid) lines are related to experiments carried out in in-house laboratories and at the synchrotron in Grenoble, respectively. For a set cooling rate, the experiment performed at the synchrotron show a higher crystallization temperature than in the case of in-house flash-DSC. The reason of these differences is related to the difference between the two experimental equipments. Therefore, a shift factor was applied on the cooling rate vector. To estimate this shift factor, the cooling curve obtained by the external flash-DSC at 50°C/s was taken as a reference. Next, the cooling curve from the in-house flash-DSC that matches the reference curve was determined. As shown in figure 3.28a, a match between 50°C/s and 20°C/s was found, thus a factor 0.4 was applied to the cooling rates (see figure 3.27a). The results are shown in 3.27a (red markers).

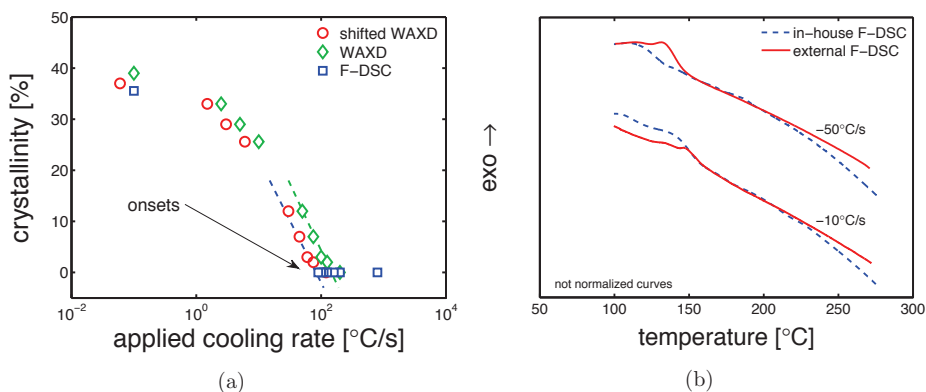


Figure 3.27: a) Crystallinity obtained by thermal analysis (blue markers), WAXD (green markers) and shifted crystallinity (red markers) as a function of cooling rate. b) Cooling thermograms regarding experiments carried out by the in-house flash-DSC and the external flash-DSC.

Also for the case of isothermal crystallization, flash-DSC results were compared with those from WAXD. In this case two measurements obtained by thermal analysis are taken as reference points i.e. the isothermal crystallization at 180°C and 90°C. In these cases, only one phase was crystallized, thus a deconvolution of the flash-DSC thermogram was possible; the melting of γ -mesophase and α -phase take place at different temperatures, therefore the melting peak area can be measured and the crystallinity can be estimated using the equation 3.3. The crystallinity values estimated by X-ray are comparable with the one obtained by flash-DSC, see figure 3.28b, thus they are used in the analysis. In order to estimate the crystallinity at temperatures for which no WAXD was performed, an interpolation over the

full range of temperature was performed, see figure 3.28b (red circles).

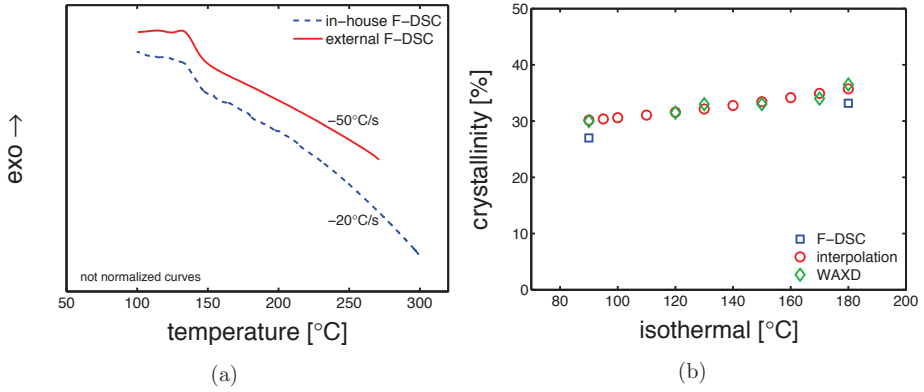


Figure 3.28: a) Matching cooling curves with different applied cooling rate. b) Crystallinity obtained by thermal analysis and WAXD as functions of applied isothermal temperature.

Chapter 4

Structure-properties relations in polyamide 6 processed in quiescent condition: influence of the thermal history on mechanical performance

Abstract

The present investigation focuses on the influence of micro-structural details on the mechanical performance of polyamide 6. Samples with different micro-structural composition (crystal structure, crystallinity, lamellar thickness) were obtained by quiescent crystallization using different thermal protocols. The mechanical properties of the different compositions were studied in uniaxial extension and creep, over a range of temperature and relative humidity. For each composition, the experimental results reveal the contribution of two molecular processes to the yield stress. These were successfully captured using a modified Ree-Eyring expression that covers the influence of relative humidity through the introduction of an apparent temperature that corrects for a change in the glass transition temperature. In combination with the concept of a critical level of accumulated plastic strain, also an accurate prediction of the creep rupture response for the different micro-structural components could be obtained. The first molecular deformation process is an intra-lamellar slip process, for which the activation volume and activation energy appear identical over all micro-structural compositions. The second process is related to inter-lamellar shear. In this case, the activation volume and activation energy are different for the two polymorphs (α, γ) covered in this study. Differences in thermal history are captured by rate constants that are a function of the lamellar thickness.

4.1 Introduction

The processing of polymer products is a widely discussed topic in polymer science [18, 19, 72, 73]. The solidification procedure is a crucial element in processing because of its influence on the structures which often affect the product performance. In the case of glassy polymers, the solidification procedure affects mainly the thermodynamic state, i.e. ageing; it was found that ageing increases as the cooling rate during solidification decreases, consequently the yield stress increases [17]. The case of semi-crystalline polymers is more complicated; pressure and cooling rate can affect strongly the material morphology, i.e. crystallinity and lamellar thickness [23, 73, 74]. The influence of morphology (structures) on properties was studied by several authors [20, 75–77], most of them concluded that the mechanical properties are highly dependent on structures. The yield kinetics of i-PP solidified upon different processing was investigated by [72, 75]; moreover, the results were described by the use of a model based on the Ree-Eyring equation. It was found that lamellar thickness (or crystal thickness) is a key parameter in order to model the yield kinetics of i-PP produced by different processing.

This work focuses mainly on the effect of processing on structures and the relations between structures and mechanical properties of polyamide 6 (PA6) tested at different temperatures and different relative humidity. PA6 crystallize, by melt processing, in two forms: a) α -phase for slow cooling ($\dot{T} < \approx 8^\circ\text{C}$), b) γ -mesophase for intermediate cooling ($\approx 8^\circ\text{C} < \dot{T} < \approx 100^\circ\text{C}$); in case of quenching ($\dot{T} > \approx 100^\circ\text{C}$), a complete amorphous material can be obtained [7]. PA6 is hydrophilic [27], if exposed to a humid environment, it absorbs water. This is due to the polar character of its amide and carbonyl groups [16]. In dry conditions, the polar groups form hydrogen bonds between the polymer chains; these H-bonds give high strength to the material [26]. In case of hydration, part of the H-bonds between chains are broken and new H-bonds are made with the water molecules. This process, also known as plasticization, enhance the chain mobility and a decrease of glass transition temperature is obtained [8]. The hydration-induced depression of T_g has a strong impact on mechanical properties [14, 28–30] as well as crystallographic properties [31].

In this work, the mechanical properties (both tensile and creep test) of polyamide 6 samples prepared with different thermal histories, and conditioned at different relative humidities, are investigated. An empirical model, based on the Ree-Eyring equation, was implemented to predict the yield kinetics and time-to-failure.

4.2 State of the art

For most of polymers, the yield kinetics (i.e. the yield stress as a function of applied strain rate) displays two regimes. These are generally attributed to an intra-lamellar deformation mechanism further referred to as processes I and an inter-lamellar mechanism, further referred to as processes II [47–49]. To describe the rate- and temperature-dependence of yield stress

obtained by tensile test at constant strain rate, the Eyring's activated flow theory [41], modified by Ree-Eyring [78] is used. In this theory, the two deformation processes are considered as independent and their stress contributions are additive. Consequently, the yield stress as a function of strain rate and temperature is calculated as follow:

$$\sigma_y(\dot{\epsilon}, T) = \frac{kT}{V_I^*} \sinh^{-1} \left(\frac{\dot{\epsilon}}{\dot{\epsilon}_{0,I}} \exp \left(\frac{\Delta U_I}{RT} \right) \right) + \frac{kT}{V_{II}^*} \sinh^{-1} \left(\frac{\dot{\epsilon}}{\dot{\epsilon}_{0,II}} \exp \left(\frac{\Delta U_{II}}{RT} \right) \right) \quad (4.1)$$

where $\dot{\epsilon}_{0,I}$, ΔU_I and V_I^* are the rate factor I, activation energy and activation volume related to process I and $\dot{\epsilon}_{0,II}$, ΔU_{II} and V_{II}^* are related to the process II. As mentioned in section 5.1, the mechanical properties of PA6 depends strongly dependent on the glass transition, which depends significantly on the sample conditioning, i.e. the hydration level. In fact, PA6 can absorb water, which acts as a plasticizer and lowers the glass transition. To include the effect of relative humidity onto the Ree-Eyring equation, the "apparent" temperature was introduced. This temperature, as explained in [50, 79], is based on the principle that a reduction in glass transition temperature is subsequently regarded as an "apparent" increase in the ambient temperature. Consequently, we express this concept as followed:

$$\tilde{T} = T + (T_{g,dry} - T_{g,wet}) \quad (4.2)$$

where T is the actual experimental temperature, $T_{g,dry}$ is the glass transition temperature at the dry state and $T_{g,wet}$ is the T_g after conditioning. The substitution into equation 4.1 leads to:

$$\sigma_y(\dot{\epsilon}, \tilde{T}) = \frac{k\tilde{T}}{V_I^*} \sinh^{-1} \left(\frac{\dot{\epsilon}}{\dot{\epsilon}_{0,I}} \exp \left(\frac{\Delta U_I}{R\tilde{T}} \right) \right) + \frac{k\tilde{T}}{V_{II}^*} \sinh^{-1} \left(\frac{\dot{\epsilon}}{\dot{\epsilon}_{0,II}} \exp \left(\frac{\Delta U_{II}}{R\tilde{T}} \right) \right) \quad (4.3)$$

With this relation, the dependence of yield stress on the temperature, strain rate and relative humidity can be predicted. Observing a creep test, i.e. test with a constant applied load, three regimes can be found: i) the primary creep regime in which the plastic flow rate decrease in time, ii) the secondary creep regime where plastic flow rate is constant in time and iii) the tertiary creep regime where plastic flow rate increase in time and finally failure occurs. Plotting, on a log-log scale plot, the plastic flow rate ($\dot{\epsilon}_{pl}$) in the secondary regime versus the corresponding time-to-failure, a linear trend with slope of -1 is found, which implies that:

$$\dot{\epsilon}_{pl}(\sigma) \cdot t_f(\sigma) = C \quad (4.4)$$

This observation held for several polymers tested at different temperatures [42] and also different relative humidity [79].

where $\dot{\epsilon}_{pl}$ is the plastic flow rate in the secondary creep regime, t_f is the time-to-failure, σ is the applied stress and C is the constant (-1). It was observed that the steady state reached by test at constant strain rate (i.e. yield stress) and the steady state achieved by test at

constant load are identical [40]. Eventually, the relation between the strain rate dependence of yield stress and the load dependence of time-to-failure is described by the critical strain concept [46, 80]:

$$t_f(\sigma, T) = \frac{\epsilon_{cr}}{\dot{\epsilon}_{pl}(\sigma, T)} \quad (4.5)$$

where ϵ_{cr} is the critical strain that can be related to the amount of plastic deformation that the material would accumulate in the case in which the $\dot{\epsilon}_{pl}$ was constant all along the creep test.

4.3 Experimental

4.3.1 Material

The material employed in this work was a polyamide 6 (Akulon K122) kindly provided by DSM (The Netherlands). This PA6 has a viscosity-average molar mass (M_v) of about 24.9 kg/mol.

4.3.2 Sample preparation

Several different cooling procedures were performed in order to prepare sheets of 0.5mm thickness with different structure parameters. The material was melted at 265°C for 5 minutes, while a force of about 10kN was applied. After this, different cooling procedures were applied:

- α -I, the hot press was switched off and the “sandwich” was left inside the hot press over night ($\approx 0.1^\circ\text{C}/\text{min}$).
- α -II, the hot press was switched to 180°C, the “sandwich” was kept under moderate pressure until 5 minutes at 180°C and then cooled in air.
- α -III, the same procedure of α -I was applied but an α -nucleating agent was added to the basic grade.
- γ -I, the “sandwich” was rapidly moved to a cold press set at 80°C where the material was solidified in quiescent condition for 5 minutes.
- γ -II, the “sandwich” was rapidly moved to a cold press set at 110°C where the material was solidified for 5 minutes.
- Q-I, the “sandwich” (only thin aluminum foils and mold) was rapidly moved to a bath of water with ice and salt (NaCl), water temperature around -14°C .

According to the ISO527 type 1BA, dog-bone samples were prepared using a cutting die (main measures: width 5mm, length 22mm).

4.3.3 Sample conditioning

In order to investigate the influence of hydration, the samples were stored at four different relative humidity, namely RH0% (dry), RH35%, RH50% and RH75%. For dry conditioning, samples were stored in a desiccators under vacuum at room temperature; for RH50% an environmental chamber was employed; while in the case of RH35% and RH75% two desiccators containing supersaturated salt solutions able to maintain a constant relative humidity in a close environment, were employed. The supersaturated solutions were made of water and two salts (at room temperature): sodium chloride and magnesium chloride hexahydrate for 75 and 35% respectively.

4.3.4 Mechanical tests

Uniaxial tensile and creep tests were performed on a Zwick Unviversal Testing Machine provided with a 1kN load-cell and equipped with an environmental chamber to control temperature and relative humidity. The tensile tests were repeated, at least, two times. Several conditions were investigated: a range of strain rates from 10^{-5} s^{-1} up to $3 \cdot 10^{-2} \text{ s}^{-1}$, temperatures between 23°C and 120°C (dry) and relative humidity of 35, 50 and 75% (at 23°C). A pre-load of 0.1 MPa was applied at a speed of 1mm/min before each experiment. Creep were performed at three relative humidities: RH35%, RH50%, and RH75%. The desired load was applied within 10 seconds, and kept constant up to failure. The time-to-failure was estimated as the time at which the strain reaches a fixed strain value of 40%, which was defined as strain at failure.

4.3.5 X-ray diffraction

Wide and small angle x-ray measurements were taken by a Ganesha X-ray instrument equipped with a GeniX-Cu ultra low divergence source ($\lambda = 1.54 \text{ \AA}$) and a Pilatus 300K silicon pixel detector (487×619 pixels of $172 \times 172 \mu\text{m}^2$). After normalization, the crystallinity was estimated by subtracting an amorphous halo (experimentally obtained) to the measured patterns. The degree of crystallinity is finally calculated by:

$$\chi_c = \frac{T - A}{T} \quad (4.6)$$

where T is the total scattered intensity and A is the scattering from the amorphous halo. Moreover, a deconvolution analysis was performed. This was obtained by fitting Lorentzian functions, in proximity of each characteristic reflection. Eventually, all the functions and the amorphous halo were summed to check the fidelity of the fitting routine (green markers in figure 4.1). Thus, the relative quantities $\chi_{c,\alpha}$ and $\chi_{c,\gamma}$ were calculated by the following:

$$\chi_{c,\alpha} = \frac{A_\alpha}{A_m} \quad \text{and} \quad \chi_{c,\gamma} = \frac{A_\gamma}{A_m} \quad (4.7)$$

where A_α and A_γ are the total area of the Lorentzian functions for the α and γ peaks, and A_m is the total area of the measured pattern. An example is given in figure 4.1. As far as the small angle X-ray scattering (SAXS) experiments is concerned, Lorentz [68] and thermal density fluctuation [69] correction were applied. The peak position of the SAXS pattern (d^*) is used to define the long period (l_b):

$$l_b = \frac{2\pi}{d^*} \quad (4.8)$$

which is used to estimate the average lamellar thickness:

$$l_c = \chi_{vol} \cdot l_b \quad (4.9)$$

where l_b is the long period and χ_{vol} is the volumetric crystallinity, which is defined by the following:

$$\chi_{vol} = \frac{\frac{\chi_c}{\rho_c}}{\frac{\chi_c}{\rho_c} + \frac{100 - \chi_c}{\rho_a}} \quad (4.10)$$

where ρ_c is the density of the crystal (1.21 g/cm^3 for α -phase [21], 1.16 g/cm^3 for γ -mesophase [21]), ρ_a the density of the amorphous (1.09 g/cm^3 [21]) and χ_c the mass crystallinity.

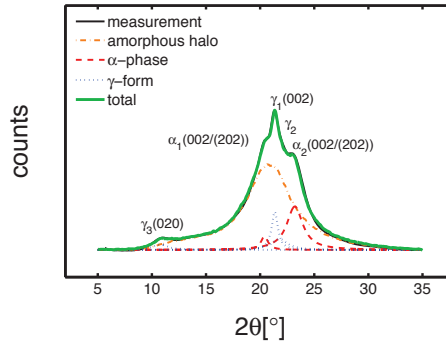


Figure 4.1: Example of WAXD pattern deconvolution analysis. The green line is the result of the deconvolution procedure, the orange line is the measured amorphous halo, blue and red curves are the Lorentzian functions.

4.3.6 Dynamical mechanical thermal analysis

Dynamical mechanical thermal analysis (DMTA) was employed to measure the glass transition temperature. The equipment was a TA instruments Q800 DMA. The samples were films

(rectangular shape) of about 5mm width, 0.5mm thickness. The sample were tested at a single frequency of 1Hz and a temperature ramp (from -40°C to 100°C) with a heating rate of $3^{\circ}\text{C}/\text{min}$. The T_g was defined as the maximum in $\tan(\delta)$.

4.4 Results and discussion

4.4.1 Samples characterization

In order to understand the effect of different processing on structures, the first step of this study was a crystallographic characterization. It was performed by wide angle X-ray diffraction (WAXD) and small angle X-ray scattering (SAXS) on samples in the dry state. In figure 4.2a and 4.2b the integrated WAXD patterns and the results of deconvolution analysis are shown, respectively.

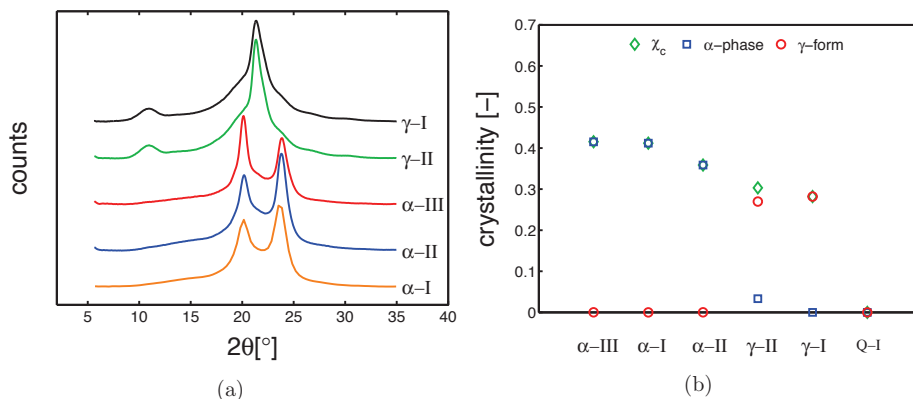


Figure 4.2: a) Wide angle x-ray diffraction integrated patterns; b) deconvolution analysis of all the investigated samples with different thermal histories (dry state).

In figure 4.2a, the integrated patterns show that the samples γ -I and γ -II have crystallized in the γ -form, which is recognizable by the characteristic central peak at around $2\theta \approx 21^{\circ}$ and the secondary peak at $2\theta \approx 10^{\circ}$; the obtained crystallinity is around 30% and by deconvolution it is possible to state that only in the case of γ -II a small fraction of α -phase is obtained, as shown in figure 4.2b. The samples α -I, α -II and α -III showed the two characteristic peaks of α -phase, at about $2\theta \approx 20^{\circ}$ and $2\theta \approx 24^{\circ}$; the obtained crystallinity is around 40% in the case of α -III and α -I, while a slightly lower crystallinity (about 35%) is obtained for α -II. These three α -samples have crystallized in pure α -phase. To estimate the average lamellar thickness, small angle X-ray were performed on the dry samples.

In figure 4.3a the integrated patterns are reported, the peak position (red markers) is translated to the long period by the equation 5.8. The relationship between L_c and crystallinity is

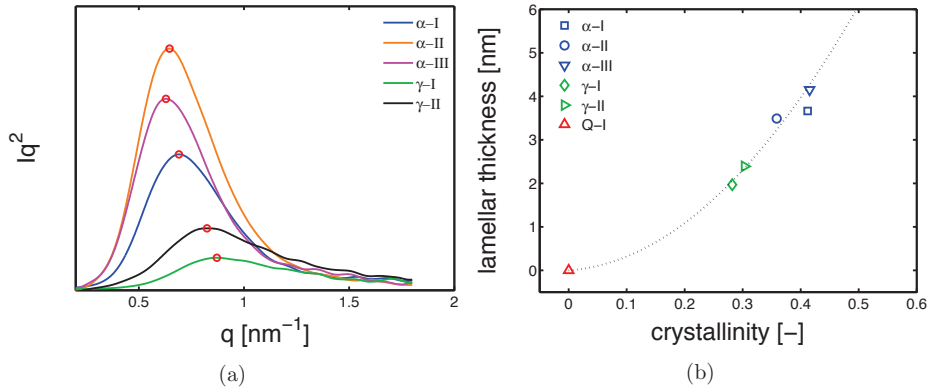


Figure 4.3: a) Small angle X-ray scattering integrated patterns in dry conditions. b) Lamellar thickness as a function of crystallinity in the dry state. The dashed line is a guide to the eye.

given in figure 4.3b; the average lamellar thickness increases for increasing crystallinity with an asymptotic-like trend. It is remarked that, as stated in [60], crystallization of γ -mesophase at high under-cooling leads to the formation of non-lamellar morphology. Therefore, the values of l_c for the γ - samples should be intended as crystal thickness rather than lamellar thickness.

4.4.2 Mechanical properties

Next, the study can proceed with the investigation of the mechanical properties. This is initially done by tensile tests at different temperatures, applying a range of strain rates (from 10^{-4} s^{-1} up to $3 \cdot 10^{-2} \text{ s}^{-1}$) in dry condition. As a starting point for the mechanical properties investigation, only three cases will be investigated: α -I for the polymorph α , γ -I for the polymorph γ and Q-I for the complete amorphous material.

As expected, the overall stress level increases as the strain rate increases for both α -I and γ -I; while it decreases with increasing temperature, see figure 4.4a and 4.4b. In the case of α -I at 23°C , the stress-strain response shows a very clear double yielding (see figure 4.4a). This occurs because the amorphous and crystalline domains yield at different strains; the yield at low strain range (about 5-10%) is regarded as the contribution of amorphous domains, and the yield at higher strain range (about 15-35%) is considered to be the contributions of crystalline regions. This effect can be simply proven by observing the effect of temperature (for a fixed strain rate) on the stress-strain response: the first yield, well visible at room temperature, tend to disappear as temperature increases and clearly disappear when the temperature is above T_g (see 4.4a green lines). It should be noted that the double yield will also occur at temperature higher than T_g if high strain rates are applied. The double yielding is less visible

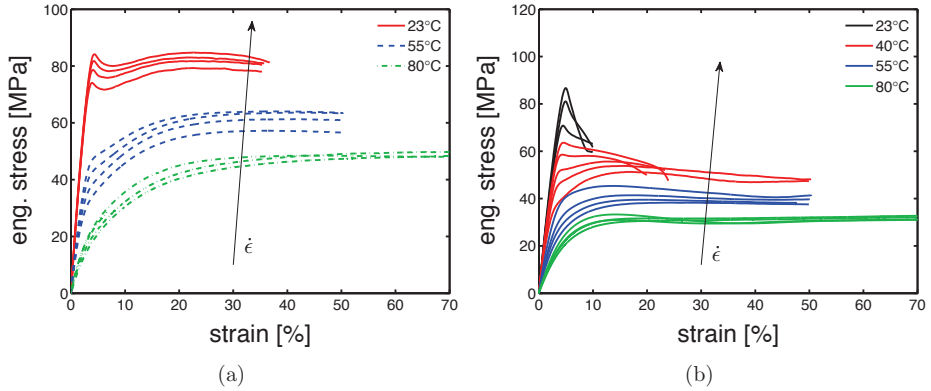


Figure 4.4: Stress-strain response at different temperatures and a range of strain rates for a) α -I and b) γ -I samples.

in the case of γ -I, which can be related to a difference in crystallinity or the level of constrain of the amorphous phase, as demonstrated by the lower value of crystallinity estimated for γ -I ($\approx 30\%$) compared with the one of α -I ($\approx 40\%$). In order to study the yield kinetics, the yield stress is plotted as a function of the applied strain rate for different temperatures.

In figure 4.6a and 4.6a the yield kinetics are shown; in both α -I and γ -I cases, two different strain rate dependences are observed, as mentioned in section 4.2. A steep slope is observed at low temperatures and (or) high strain rates, while a rather flat one is displayed at high temperatures and (or) low strain rates. In figure 4.5, a schematic decomposition of the two processes is proposed.

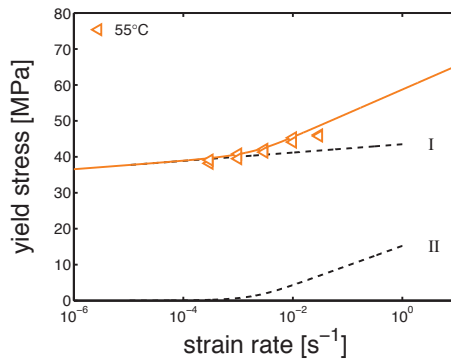


Figure 4.5: Example of two processes contributions. Yield stress versus strain rate at 55°C; the black dashed lines are the two contribution separated (process I and II).

	$V^* [m^3]$	$\Delta U [J mol^{-1}]$	$\dot{\epsilon}_0 [s^{-1}]$
I	$9 \cdot e-27$	$1 \cdot e6$	$1 \cdot e108$
II	$6 \cdot e-27$	$3.2 \cdot e5$	$4 \cdot e45$

 Table 4.1: Ree-Eyring parameters for α -I.

	$V^* [m^3]$	$\Delta U [J mol^{-1}]$	$\dot{\epsilon}_0 [s^{-1}]$
I	$9 \cdot e-27$	$1 \cdot e6$	$1 \cdot e122$
II	$1.9 \cdot e-27$	$3 \cdot e5$	$2 \cdot e45$

 Table 4.2: Ree-Eyring parameters for γ -I.

In order to describe the yield kinetics obtained experimentally, equation 4.1 is used and the parameters in table 5.1 and 5.2 were employed.

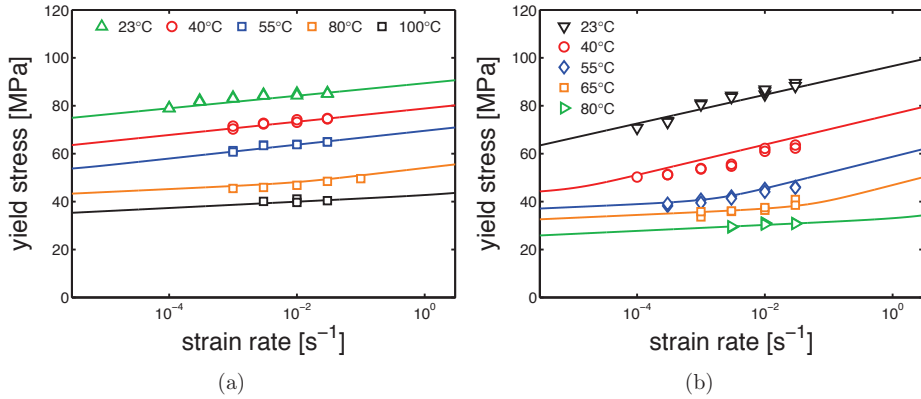


Figure 4.6: Stress-strain response at different temperatures (ranging from 23°C to 100°C) and a range of strain rate from $10^{-4} s^{-1}$ up to $3 \cdot 10^{-2} s^{-1}$ for a) α -I and b) γ -I samples. Lines are the results of equation 4.1.

In figure 4.6a and 4.6b it is shown that the model can describe well the results at different temperatures for both α -I and γ -I. Moreover, it is observed that the activation energy and activation volume employed for process I are the same for both α -I and γ -I. The parameters of process II do not match between the two different polymorphs; a plausible reason could be found in differences in amorphous constraint. Looking at the mobility scenario in a semi-crystalline polymer, it is known that, the crystalline regions have the lowest mobility whereas the amorphous region should have the highest mobility. However, an elevated presence of crystalline regions may constrain the amorphous regions, with a consequently decrease of mobility. Thus a difference in crystallinity may affect also the state (mobility) of the amorphous regions.

4.4.3 Influence of temperature

To obtain a large overview about the effect of temperature on the yield stress, several tensile tests were performed at $10^{-2} s^{-1}$ and testing several temperatures, see figure 4.7. Observing the results in figure 4.7a, it is possible to notice a clear double yielding behavior at temperature

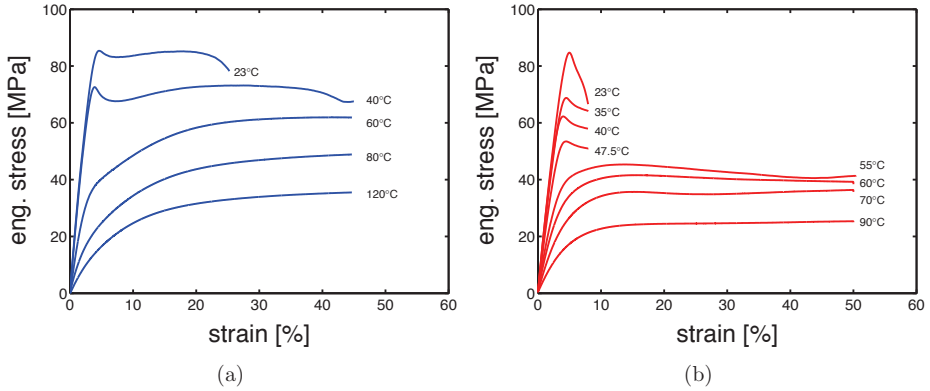


Figure 4.7: Stress-strain response at temperatures in a range from 23 to 120°C, and strain rate of 10^{-2} s^{-1} for a) α -I and b) γ -I samples.

lower than T_g , while increasing the testing temperature, the first yield (at low strains) tends to disappear. The α -I samples show a predominantly crystalline contribution to yield, this is due to a high crystallinity index and a relatively high lamella thickness. Figure 4.7b shows a very different picture; at low temperature, yield takes place at low strains ($\approx 5\%$) and it moves to about 15% strain when the temperature is increased above 50°C. Comparing the strain at yield for both α -I and γ -I samples, we observed a very similar strain for the yield related to the amorphous domains (about 5%), whereas the contribution of the crystalline domains takes place at quite different strain range, $\approx 15\%$ for γ -I and about 30% for α -I. Please note that these observations are strictly related to engineering stress-strain curves.

Figure 4.8 shows that α -I, γ -I and Q-I samples have three very different temperature dependence. For the green markers, related to Q-I samples, no description (solid line) is provided. In fact, looking at the trend of yield stress as a function of temperature, three regions are found: i) at low temperature, yield stress decrease drastically as temperature increases, ii) at about 50°C the yield stress reaches a minimum, iii) after which the material starts cold crystallizing and the yield stress increases and reaches a plateau up to 120°. The variation of yield stress of Q-I is due to structure development (cold crystallization, etc.) which is time- and temperature-dependent. For this reason, the Q-I samples will be taken out of this study. As far as the blue and red markers (α -I and γ -I respectively) are concerned; they show very similar yield stress at 23°C but, as temperature increases, γ -I yield stress decrease more rapidly than α -I. In these two cases, the model is applied: in the case of α -I, the experimental results are matching the description; in the case of γ -I, the description matches the experimental results up to 90°C. After this temperature, the experimental yield stress flattens. As already explained in [79], an evolution of crystallinity and/or lamellar thickness takes place

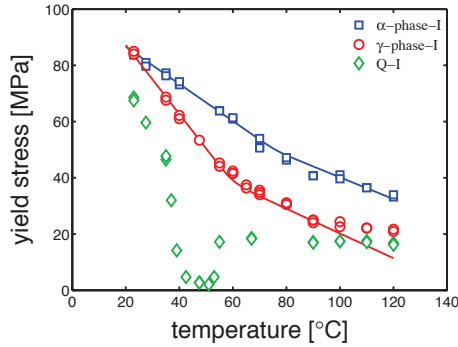


Figure 4.8: Yield stress versus testing temperature of samples tested with a strain rate of 10^{-2} s^{-1} and several temperatures. The lines are the results of equation 4.1 in which the strain rate is a fixed value (10^{-2} s^{-1}) and the temperature is a ranging from 23 to 120°C.

at high temperatures; this phenomenon, called “annealing”, is a time- temperature-activated process, which is governed by an enhancement of mobility that results in either cold crystallization and (or) lamellar thickening (perfectioning). Hence, higher crystallinity and (or) lamellar thickness result in an increase of yield stress, as shown in figure 4.8. This effect is not observed in the case of α -I samples. It is hypothesized that “annealing” does not occur in α -I because of the already very high crystallinity and lamellar thickness obtained during processing.

The Ree-Eyring equation is applied with satisfactory results on the dry samples for both the two polymorphs, and two set of parameters have been defined for the α -phase and γ -form, respectively; next, the influence of relative humidity and other thermal histories are investigated.

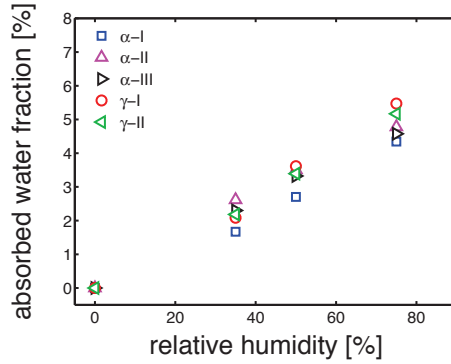
4.4.4 Influence of humidity

As explained in section 5.3.3, the samples were exposed to humid environments (relative humidity ranging from 35 to 75%) for a period long enough to allow the complete saturation. All the samples were conditioned at room temperature (23°C). The absorbed water fraction was calculated by the following:

$$W\% = \left(\frac{W_i - W_0}{W_0} \right) \times 100 \quad (4.11)$$

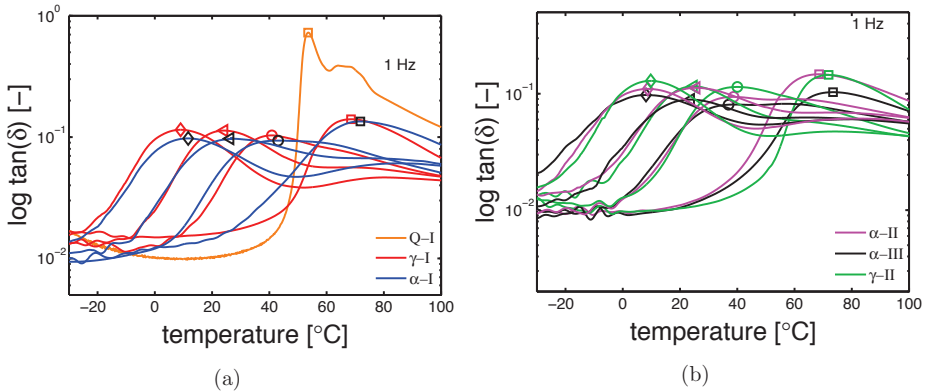
where W_0 is the weight of the sample before conditioning and W_i is the weight at the time t_i .

The absorbed water fraction is plotted as a function of relative humidity (HR%), se figure 4.9a. The saturation level is different between the the samples because of a difference in crystallinity, as mentioned in section 5.1, water can be absorbed only by the amorphous regions



(a)

Figure 4.9: Absorbed water percentage at saturation in environments with different relative humidity at 23°C.



(a)

(b)

Figure 4.10: DMTA results, $\tan(\delta)$ as a function of temperature for samples conditioned at different humidity; markers are the T_g at \square) RH0%, \circ) RH35%, \triangleleft) RH50%, \diamond) RH75%. a) Samples α -I and γ -I; b) α -II, α -III and γ -II.

(because of their mobility state). The results of the thermal-mechanical characterization, performed by DMTA, are shown in figure 4.10a and 4.10b. The details about this technique are given in section 5.3.6. Figure 4.10a shows the results of DMTA for the samples Q-I, α -I and γ -I after conditioning at different RH%; the markers are the defined T_g 's. The Q-I is presented only in dry condition, because upon conditioning, it crystallizes and therefore it changes drastically its state. Figure 4.11a shows the glass transition temperatures as functions of absorbed water fractions. At RH0% (dry condition) all the investigated samples show a maximum in glass transition temperature; with increasing absorbed water fraction,

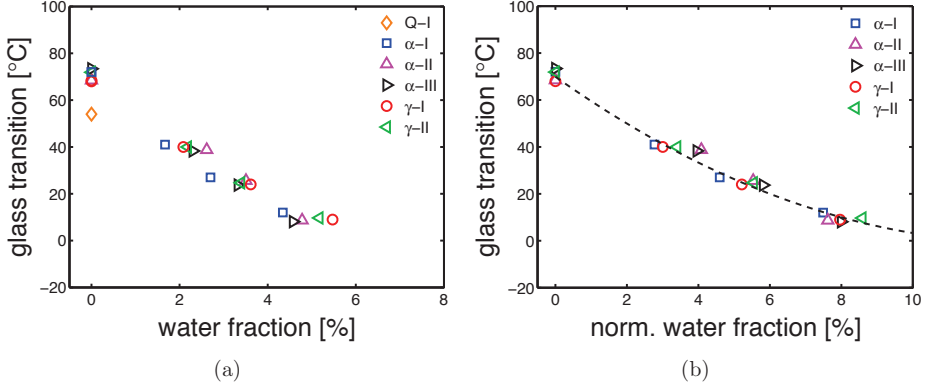


Figure 4.11: (a) Glass transition temperatures (obtained by DMTA) as functions of the water fraction absorbed by the samples. (b) Glass transition temperatures as functions of the normalized water fractions (line is a guide to the eye).

a monotonic decrease of T_g is recorded. This is due to the plasticizing effect described in section 5.1. Moreover, relying on the fact that only the amorphous region can absorb water, the glass transition temperature can be plotted as a function of normalized water fraction. The normalization is applied as follow:

$$W_n \% = \frac{W\%}{1 - \chi_{vol}} \times 100 \quad (4.12)$$

where χ_{vol} is the crystallinity and $W\%$ is the water fraction estimated experimentally (see equation 4.11). The results are shown in figure 4.11b. As proposed, T_g follows a unique trend if plotted against a normalized water fraction. All the T_g are reported in table 5.6.

Table 4.3: Glass transition temperature [°C].

sample	dry	35RH%	50RH%	75RH%
α -I	72	43	27	12
α -II	68	39	26	9
α -III	73	38	24	8
γ -I	68	41	24	9
γ -II	72	40	25	10
Q-I	53	-	-	-

As already mentioned in section 5.1, the glass transition can drop at temperature even below room temperature. In this case, the polymer chains acquire the sufficient mobility needed to cold crystallize and (or) thickening the pre-existing crystals. The crystallinity can be plotted as a function of relative humidity for different samples as shown in figure 4.12a.

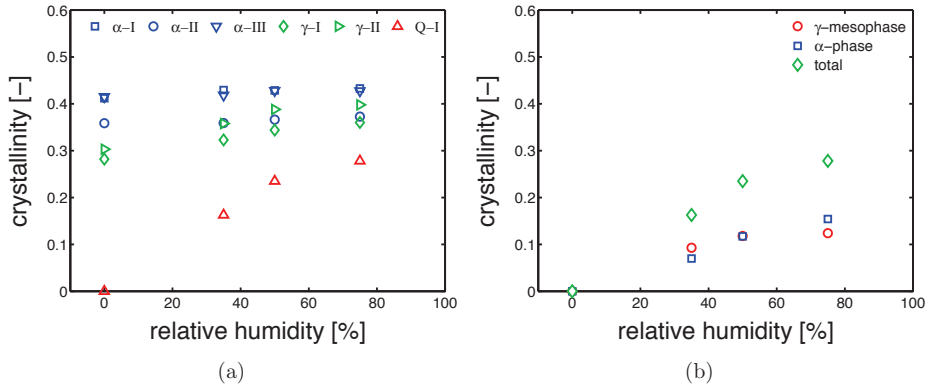


Figure 4.12: a) Overall crystallinity values as functions of relative humidity (conditioning performed at 23°C). b) Evolution of the crystallographic phase contents as functions of relative humidity (conditioning performed at 23°C) starting from Q-I (amorphous) sample.

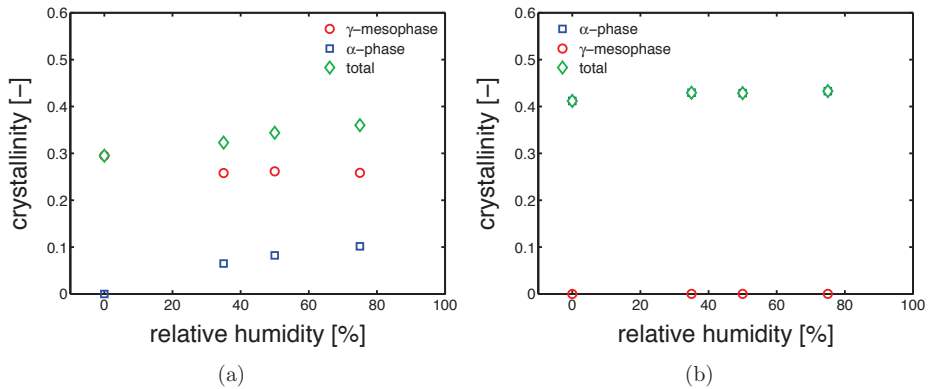


Figure 4.13: Evolution of the crystallographic phase contents as function of relative humidity (conditioning performed at 23°C) starting from a) γ -I and b) α -I sample.

Figure 4.12a shows that hydration has an actual effect on the crystallographic properties of PA6. In details, the crystallinity of Q-I samples rapidly increases for increasing relative humidity, γ -samples show a modest increase of crystallinity and α -samples show a rather constant crystallinity. In order to investigate the process of “cold crystallization” taking place in the Q-I samples, the deconvolution analysis of the WAXD patterns was performed, results are shown in figure 4.12b. The samples Q-I, starting from a completely amorphous material, are exposed to three different relative humidities, always at room temperature. The lowest RH% (35%) lead to crystallization of γ -form and α -phase with a balance slightly shifted towards the

γ -form; at 50RH% the total χ_c increases and the balance γ - α is perfectly even; at the highest investigated relative humidity (75%) the crystallinity increase even further and the balance γ - α is slightly shifted towards the α -phase. In the case of γ -samples, the starting material is already semi-crystalline with a rather high crystalline index, thus secondary crystallization, phase transition and (or) lamellar perfectioning (thickening) are expected. In figure 4.13a the results of deconvolution analysis for γ -I are shown. The χ_c increases along the all range of relative humidity, in particular a slight decrease of γ -form and a substantial increase of α -phase is detected. This effect can be related to a partial transformation γ to α , followed by a secondary crystallization of α -phase. In the case of α -I, see figure 4.13b, the deconvolution reveals that no transformation takes place and only the crystallinity seems to increase a little (probably within an experimental error).

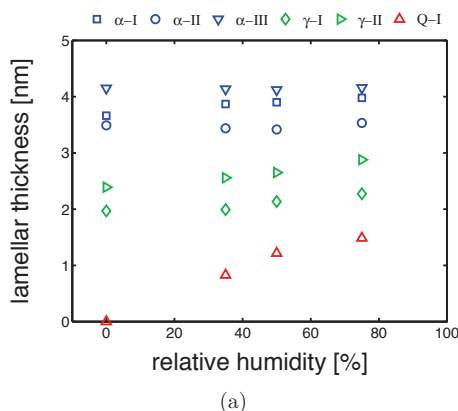


Figure 4.14: Lamellar thicknesses as functions of relative humidity. All conditioning were performed at 23°C.

In order to capture the lamellar thickness evolution upon hydration, SAXS experiments were performed (as explained in section 5.3.5). In figure 4.14a, the results of lamellar thickness are proposed as a function of relative humidity. Similar trend to χ_c versus $RH\%$ are found. The lamellar thickness of Q-I samples increase quickly with relative humidity; also the l_c of γ -samples increases although less rapidly than the amorphous samples; while the α -samples lamellar thickness are rather steady.

After, the samples were tested by tensile test at different relative humidity and a range of strain rates ($10^{-5} s^{-1}$ up to $3 \cdot 10^{-2} s^{-1}$). As it was done for yield kinetics in dry condition, the aim is to describe also the results of test at different relative humidity by the Ree-Eyring equation (see section 4.2, equation 5.2) employing the two set of parameters defined for the α -phase and γ -form, see table 5.1 and 5.2. Firstly, the model is applied to the samples α -I and γ -I, the results are shown in figures 4.15a and 4.15b.

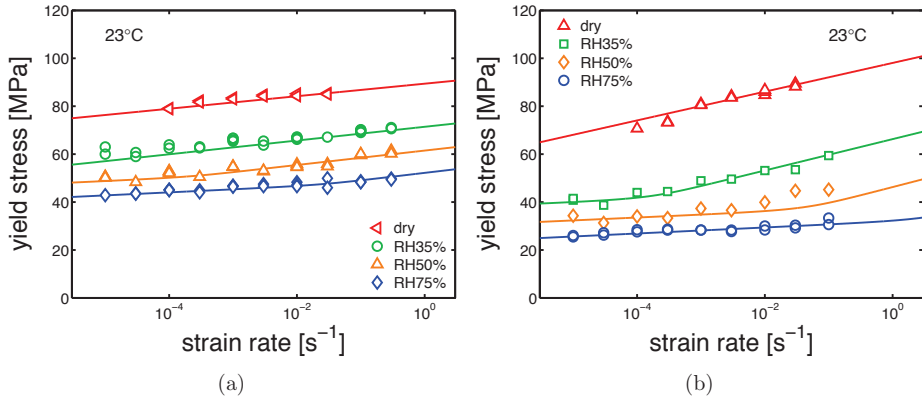


Figure 4.15: a) Yield stress as a function of strain rate for samples conditioned at different relative humidity, a) α -I and b) γ -I. Testing temperature set at 23°C.

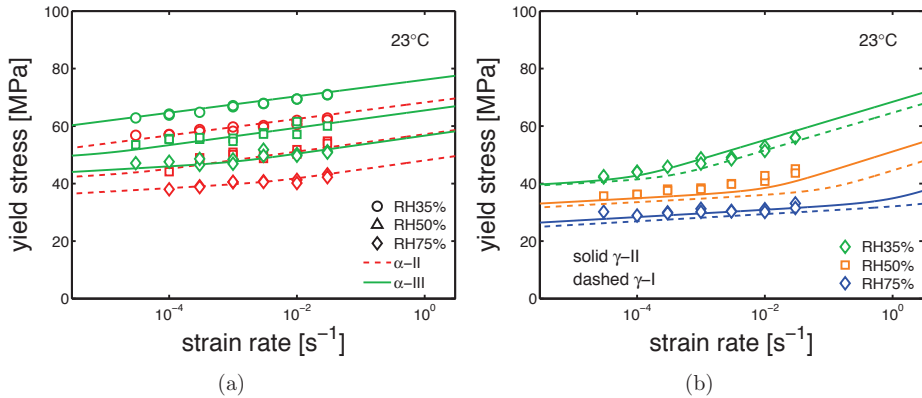


Figure 4.16: a) Yield stress as a function of strain rate for samples conditioned at different relative humidity, a) α -II, α -III and b) γ -II (solid lines) and γ -I (dashed lines). Testing temperature set at 23°C.

It is shown that equation 5.2 describes the experimental results obtained at different conditions for two polymorph of PA6. As shown in tables 5.1 and 5.2, the parameters employed for the α and γ polymorph differ mainly in the rate factors and the processes II (inter-lamellar deformation). In figures 4.16a and 4.16b, the yield kinetics of α -II, α -III and γ -II are shown, respectively. In order to describe these experimental result, the set of parameters used for α -I was employed for α -II and α -III, whereas the set used for γ -I was employed γ -II; in both cases, only the rate factors ($\dot{\epsilon}_{0,I}$ and $\dot{\epsilon}_{0,II}$) had to be changed. It is assumed that only $\dot{\epsilon}_{0,I}$ and $\dot{\epsilon}_{0,II}$ are influenced by the lamellar thickness, as proposed by [72, 75], while the V^* and ΔU

	$V^* [m^3]$	$\Delta U [J mol^{-1}]$	$\dot{\epsilon}_0 [s^{-1}]$
I	$9 \cdot e-27$	$1 \cdot e6$	$3 \cdot e112$
II	$6 \cdot e-27$	$3.2 \cdot e5$	$3 \cdot e48$

 Table 4.4: Ree-Eyring parameters for α -III.

	$V^* [m^3]$	$\Delta U [J mol^{-1}]$	$\dot{\epsilon}_0 [s^{-1}]$
I	$9 \cdot e-27$	$1 \cdot e6$	$1 \cdot e123$
II	$1.9 \cdot e-27$	$3 \cdot e5$	$6 \cdot e45$

 Table 4.6: Ree-Eyring parameters for γ -II.

	$V^* [m^3]$	$\Delta U [J mol^{-1}]$	$\dot{\epsilon}_0 [s^{-1}]$
I	$9 \cdot e-27$	$1 \cdot e6$	$3 \cdot e106$
II	$6 \cdot e-27$	$3.2 \cdot e5$	$8 \cdot e47$

 Table 4.5: Ree-Eyring parameters for α -II.

are considered to be independent to l_c . The parameters employed for these cases are listed in table 4.4, 4.5 and 4.6.

4.4.5 Time-to-failure

Next, the influence of relative humidity on the PA6 lifetime was investigated. Several creep tests were performed at 23°C and relative humidity ranging from 35% to 75%. All the five sample series were tested at different applied load. Subsequently, the $\dot{\epsilon}_{pl}$ is estimated by the use of Sherby-Dorn plot [43]; where the strain rate is plotted as a function of strain, and the $\dot{\epsilon}_{pl}$ is defined as the minimum of the obtained curve. After, all the $\dot{\epsilon}_{pl}$ are plotted as functions of the corresponding time-to-failure, as shown in 4.17b. As mentioned in section 4.2, the data plotted in a log-log graph, show a slope of -1.

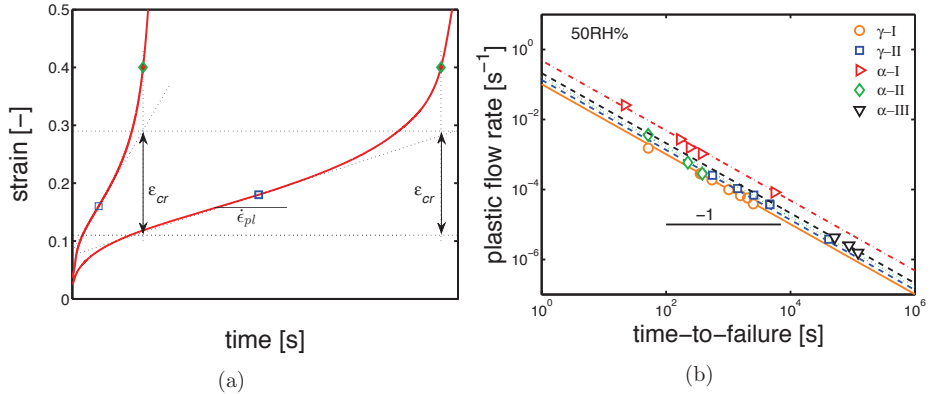


Figure 4.17: a) Examples of creep tests at constant applied load, the scheme shows the definition of $\dot{\epsilon}_{pl}$, ϵ_{cr} and t_f . b) Plastic flow rates as functions of time-to-failure for samples conditioned at RH50% and 23°C.

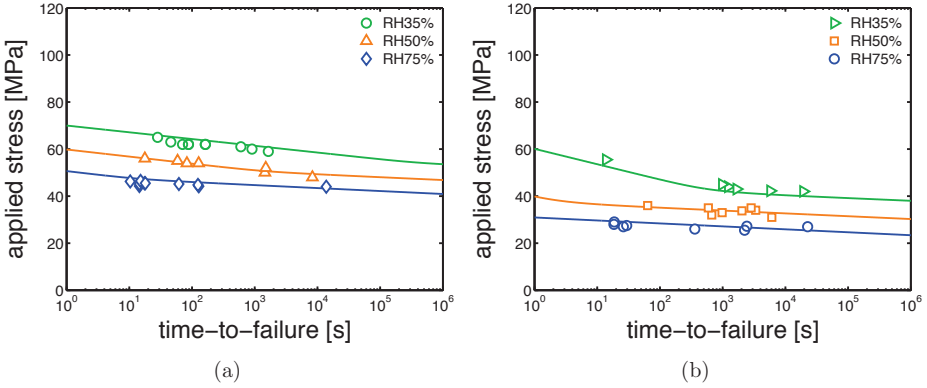
By extrapolating to $t_f = 1$ s the results shown in figure 4.17b, the ϵ_{cr} is estimated. Eventually, to describe the time-to-failure results obtained for the different samples series, the

	α -I	α -II	α -III	γ -I	γ -II
ϵ_{cr}	0.32	0.19	0.14	0.16	0.17

Table 4.7: Average critical strains obtained at different relative humidities.

$\dot{\epsilon}_{pl}$ obtained by the Ree-Eyring equation (eq.5.2) modified to include the influence of relative humidity are combined with the ϵ_{cr} in equation 5.3. The average ϵ_{cr} obtained for conditioning at different RH%, are reported in table 4.7; please note that different thermal histories as well as different humidities led to different critical strain.

In figure 4.18a and 4.18b, the applied loads are plotted as functions of the time-to-failure. The lines are the results of equation 5.3 and they are related to samples conditioned at different relative humidities (range from 35-75%) and 23°C. The lines have the same stress dependence of the ones shown in figure 4.15a and 4.15b but the slopes have opposite sign.


 Figure 4.18: Creep tests for samples conditioned at RH35%, RH50%, RH75% and 23°C; applied loads as functions of time-to-failure for a) α -I and b) γ -I samples. Lines are the results of equation 5.3.

Figures 4.18a and 4.18b show that a satisfactory prediction of time-to-failure is achieved for samples α -I and γ -I employing the set of parameters reported in table 5.1 and 5.2 for samples α -I and γ -I, respectively. By the use of the parameters listed in tables 4.4,4.5 and 4.6, also samples α -II, α -III and γ -II are described by equation 5.3; the results are shown in figure 4.19a and 4.19b.

4.4.6 Structure-properties relations

For all the investigated PA6 samples, the temperature, relative humidity and stress dependent deformation kinetics were captured by the Ree-Eyring theory. To apply this theory, the characteristic parameters were defined, namely the activation volume (V^*), the activation energy

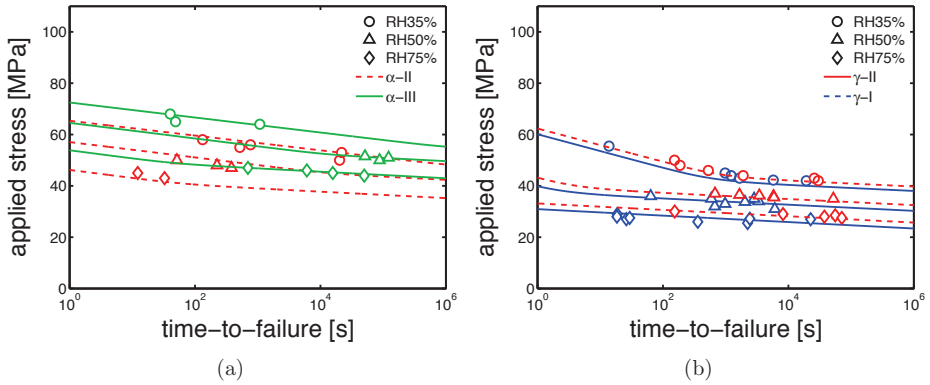


Figure 4.19: Creep tests for samples conditioned at RH35%, RH50% and RH75% and 23°C; applied loads as functions of time-to-failure for a) α -II, α -III, b) γ -I and γ -II samples. Lines are the results of equation 5.3.

(ΔU) and the rate factors ($\dot{\epsilon}_0$). As explained in section 4.4.2, PA6 shows two regimes with different strain rate dependence related to two deformation mechanisms; an intra-lamellar deformation mechanism (also called process I) and an inter-lamellar mechanism (also called process II). As shown in equation 4.1, each process need one set of parameters.

The analysis has led to conclude that: i) for process I, identical activation volume and activation energy can be used for all the samples type, a part for the quenched samples whose structures, as explained in section 4.4.3, are very dependent to temperature and relative humidity; ii) for the process II, V^* and ΔU are different for the two different polymorphs, i.e. α -phase and γ -mesophase; iii) the rate factors were varied for each samples series, for both process I and process II. About the different V^* and ΔU determined for the two crystallographic phases in the case of process II, the author can only hypothesize that the reason might be in the different level of constraint the amorphous phase. In fact, as proposed in a previous study [79], process II is associated to the deformation of the amorphous phase. About the rate factors ($\dot{\epsilon}_{0,I}$ and $\dot{\epsilon}_{0,II}$), a rather clear correlation between the lamellar thickness (l_c) was found, see figures 5.14a and 5.14b.

Figure 5.14a shows the relation between the rate factor I ($\dot{\epsilon}_{0,I}$) and the lamellar thickness; plotting the logarithm of $\dot{\epsilon}_{0,I}$ as functions of lamellar thickness for both α and γ samples, a linear trend is found. In the case of $\dot{\epsilon}_{0,II}$, two trends are found: one related to the α -samples and one for the γ -samples, see figure 5.14b. Remember that also the V^* and the ΔU are different for the process II, therefore there is no reason to expect that the trend of $\dot{\epsilon}_{0,II}$ for α matches the one for γ samples. This relation between the rate factors and the lamellar thickness was also proposed by other authors in the case of i-PP (isotactic polypropylene) [72, 75]. The fundings shown in figure 5.14a and 5.14b are crucial for the prediction of

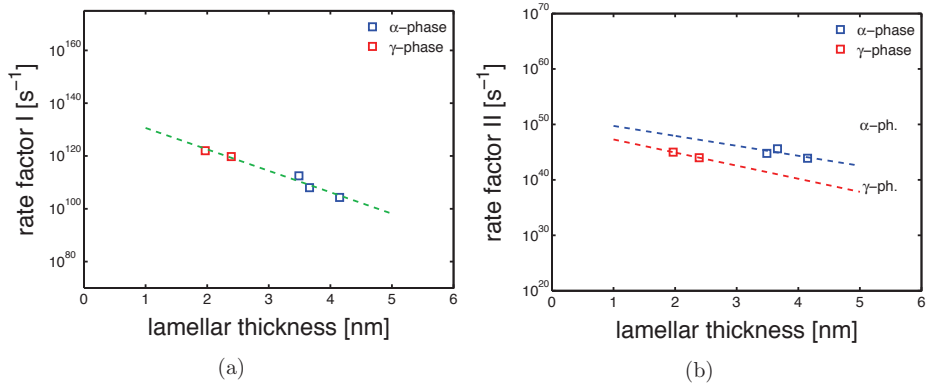


Figure 4.20: a) Rate factor I ($\dot{\epsilon}_{0,I}$) and b) rate factor II ($\dot{\epsilon}_{0,II}$) as functions of lamellar thickness. Lines are guides to the eye.

the deformation kinetics and time-to-failure of PA6 processed with different histories. It is important to remark that in the case of “real-life” applications, products are designed to work upon load largely below the yield stress, hardly in dry conditions and often at high temperatures. Thus, the most frequent failure mode would be governed by intra-lamellar deformation, i.e. the process I; consequently, the prediction would be governed by a V^* and ΔU which are not dependent on the crystallographic phase.

4.5 Conclusions

In this work, the influence of thermal history on the structure of PA6 was investigated on regards to the mechanical properties (short and long term failure) of samples tested at different temperature and relative humidity. The investigation has led to several conclusions:

- the thermal history, i.e. the solidification procedure, has a crucial effect on the polymorphism and subsequently on the stress-strain response. By observing the three extreme cases (α -I, γ -I and Q-I), differences in strain rate- and temperature-dependence of the stress-strain response were found. The α -I samples have shown the least dependence on strain rate (see figure 4.6a) and temperature (see figure 4.8), while Q-I resulted the most dependent on strain rate and temperature, and γ -I has shown a moderate dependence on strain rate and temperature.
- by quenching from the molten state, completely amorphous samples (Q-I) were obtained; these samples are extremely sensitive to temperature and relative humidity. Heating a Q-I sample above ≈ 50 °C, cold crystallization is obtained. Please note that this phenomenon is time- temperature- dependent, therefore according to the temperature and time span of testing, different stress strain response is obtained. Also in case of exposition to moisture, cold crystallization occurs even at relative humidity of 35%.
- the Ree-Eyring equation was successfully applied to describe the yield kinetics of samples α -I and γ -I. This was possible by employing two set of parameters, with identical V^* and ΔU for the process I and different V^* and ΔU for the process II.
- a modification of the Ree-Eyring equation to include the effect of relative humidity on the glass transition was applied successfully on all the investigated samples (a part for the quenched ones). Moreover, by the use of the critical strain concept, the time-to-failure of samples conditioned at different relative humidity were described.
- similar to i-PP, a correlation between the rate factors $\dot{\epsilon}_0$ and the lamellar thickness was found. For a given activation volume and activation energy, the corresponding $\dot{\epsilon}_0$ is dependent on the lamellar thickness (l_c).
- the effects of relative humidity on the crystallographic properties (i.e. lamellar thickness, crystallinity and crystal phase) are considered negligible at the scope of description of mechanical properties.

4.6 Acknowledgments

This work is part of the Research Program of the Dutch Polymer Institute DPI, Eindhoven, the Netherlands, project number #786.

Chapter 5

Injection molding of polyamide 6: influence of mold temperature on the yield and failure kinetics at different environmental conditions

Abstract

The effect of the mold temperature on the mechanical properties of injection molded polyamide 6 samples was investigated. The yield and failure kinetics were studied by performing tensile and creep tests at several temperature and relative humidities. A large influence of the mold temperature on structure formation was observed. Also the influence of pressure and shear flow during crystallization was taken in consideration. As far as the mechanical properties are concerned, a strong influence of temperature and relative humidity on the yield stress and time-to-failure was found. An empirical model, able to describe the yield and failure kinetics, was applied to the experimental results with regards to the crystalline phase present in the sample. It is observed that, for high mold temperatures, the samples morphology is more stable to humidity and temperature than in the case of low mold temperatures and this effects could be successfully described by the model. The samples molded at low temperatures showed a strong evolution of the crystallographic properties when exposed to high temperature and high relative humidity; which makes the final description rather complicated.

5.1 Introduction

Injection molding is the most widely used technique to produce polymeric products. It is particularly preferred because of advantages such as fast production cycles, suitability for mass production and the versatility of product shapes. However, injection molding holds some challenges, interesting for users, engineers and polymer scientists. In fact, this technique involves high pressure, elevated shear flow and inhomogeneous transient temperature fields during solidification. The effect of the mold temperature on the mechanical properties is a widely studied topic in polymer engineering. In the case of amorphous polymers, the main influence of mold temperature on the yield stress is attributed to aging; a higher age of the material corresponds to higher yield stress [17]. In the case of semi-crystalline polymers, the topic becomes more complicated. It is well known that injection molded samples do not have an homogeneous morphology along the sample thickness and position [81–83]. Ideally, due to different conditions during solidification, three different morphologies can be detected in the sample thickness: i) the outermost layer (also called skin layer) is subjected to fast cooling, that lead to amorphous or slightly crystalline material; ii) the central layer (also called core layer) solidifies under high pressure and slow cooling rate, generally leading to high crystallinity; iii) the inter-phase between the skin and core layer is called the shear layer, which is subjected to high shear rates that can play an important role in the crystallization kinetics [84]. Because of this shear flow, a highly oriented morphology can be formed in the shear layer which can give rise to a strong mechanical anisotropy [83]. The morphology of injection molded nylon 6 was reported in literature [81, 85]. These studies led to a common main conclusion: the metastable γ -mesophase (obtainable for moderate cooling rates [7]) is predominant near the surface of the sample, while the most stable α -phase (obtained by slow cooling [7]) takes over towards the center of the sample. The effect of this inhomogeneous morphology distribution on mechanical properties is hardly studied while these are of vital importance to the end-users. Therefore, in this study, the effect of mold temperature on the mechanical properties of polyamide 6 is investigated. The samples for mechanical testing were conditioned at different temperatures and different relative humidities.

5.2 State of the art

In previous studies, the authors have investigated the influence of structural properties (crystalline phase and lamellar thickness), temperature and relative humidity on the yield kinetics and time-to-failure of polyamide 6 processed under quiescent conditions. Firstly, the Ree-Eyring equation, normally used to describe the yield kinetics as a function of temperature and strain rate, was modified in order to include the effect of relative humidity [79]. To

accomplish this, the “apparent” temperature (\tilde{T}) was introduced:

$$\tilde{T} = T + (T_{g,dry} - T_{g,wet}) \quad (5.1)$$

where T is the actual temperature, $T_{g,dry}$ is the glass transition temperature at the dry state and $T_{g,wet}$ is the T_g after conditioning. Next, this “apparent” temperature is substituted in the Ree-Eyring equation:

$$\sigma_y(\dot{\epsilon}, \tilde{T}) = \frac{k\tilde{T}}{V_I^*} \sinh^{-1} \left(\frac{\dot{\epsilon}}{\dot{\epsilon}_{0,I}} \exp \left(\frac{\Delta U_I}{R\tilde{T}} \right) \right) + \frac{k\tilde{T}}{V_{II}^*} \sinh^{-1} \left(\frac{\dot{\epsilon}}{\dot{\epsilon}_{0,II}} \exp \left(\frac{\Delta U_{II}}{R\tilde{T}} \right) \right) \quad (5.2)$$

where $\dot{\epsilon}_{0,i}$, ΔU_i and V_i^* are the rate factor, the activation energy and the activation volume related to the i process. These processes are related to two different deformation mechanisms; process I to intra-lamellar deformation and process II to inter-lamellar deformation. Subsequently, this work focused on applying the model also in case of different crystal phases with varying lamellar thicknesses (l_c). For the two different polymorphs, two sets of parameters were defined, one for α -phase and one for γ -mesophase. Remarkably, the first process of both the polymorphs could be described with identical activation energy (ΔU_I) and activation volume (V_I^*) [86]. A relation between the lamellar thickness (l_c) and the rate factors ($\dot{\epsilon}_{0,i}$) was found [86]. Thus, by selecting the right set of parameters related to the crystal phase present, the yield kinetics of different samples with different l_c can be described. The parameters defined for α -phase and γ -mesophase are listed in tables 5.1 and 5.2, respectively.

	$V^* [m^3]$	$\Delta U [J mol^{-1}]$
I	9.e-27	1.e6
II	6.e-27	3.2.e5

Table 5.1: Ree-Eyring parameters defined for α -phase.

	$V^* [m^3]$	$\Delta U [J mol^{-1}]$
I	9.e-27	1.e6
II	1.9.e-27	3.e5

Table 5.2: Ree-Eyring parameters defined for γ -mesophase.

Moreover, by the use of the “critical strain” concept, the prediction made for the yield kinetics can be reconverted in prediction for the time-to-failure [40, 42, 80]. The time-to-failure (t_f) is estimated by the equation:

$$t_f(\sigma, T) = \frac{\epsilon_{cr}}{\dot{\epsilon}_{pl}(\sigma, T)} \quad (5.3)$$

in which ϵ_{cr} is the critical strain and $\dot{\epsilon}_{pl}$ is the plastic flow rate as function of load and temperature obtained by the yield kinetics, see equation 5.2.

5.3 Experimental

5.3.1 Material

The material employed in this work was a polyamide 6 (Akulon K122) kindly provided by DSM (NL). This PA6 has a viscosity-average molar mass (M_v) of about 24.9 kg/mol.

5.3.2 Sample preparation

To dry the pellets prior to processing, the material was placed in a vacuum oven at a temperature of 110°C for 12hr. Next, the injection molding procedure was performed with the following parameters: temperature profile from the hopper to the nozzle, 70°C, 230°C, 240°C, 250°C, 245°C and 240°C; injection flow, 90 cm³/s; maximum injection pressure, 500 bar; holding pressure, 500 bar; cooling time 30 s. Moreover, four different mold temperatures were used: 35, 85, 130 and 160°C. The samples are 1 mm thick squared plates with side lengths of 70 mm. The injection gate was situated orthogonally to the plate plane, see figure 5.1. Dog-bone shape samples were cut by the mean of a cutting die, according to the ISO527 type 1BA (main dimensions: width 5mm, length 22mm). The samples were cut in parallel and perpendicular direction compared to the flow, see figure 5.1.

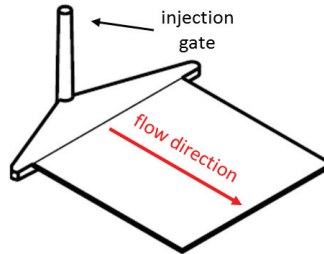


Figure 5.1: Schematic representation of a sample obtained by injection molding (70×70×1 mm).

As supporting experiments, also sheets with a thickness of 0.5mm were prepared by compression molding. The material was melted at 265°C for 5 minutes, while a force of about 10kN was applied, then it was rapidly moved to a cold press set at 80-120-140-160-180°C where the material was solidified in quiescent condition for 3 minutes.

5.3.3 Sample conditioning

The samples were conditioned at room temperature (23°C) at four different relative humidities: RH0% (dry) using a vacuum chamber at room temperature, RH35% and RH75% by using chambers containing supersaturated solutions of sodium chloride and magnesium chloride hexahydrate respectively; RH50% was obtained in an environmental chamber. The samples were kept in the conditioning environment up to saturation (≈ 30 days). The absorbed water fraction was calculated by the following equation:

$$W\% = \left(\frac{W_i - W_0}{W_0} \right) \times 100 \quad (5.4)$$

where W_0 is the weight of the sample in dry conditions and W_i is the weight at the time t_i . The saturation was identified as the level of water fraction after which a plateau is reached. A better definition of the water fraction is considered to be the normalized water fraction in which the water fraction is normalized for the fraction of amorphous phase:

$$W_n \% = \frac{W\%}{1 - \chi_c} \times 100 \quad (5.5)$$

where χ_c is the crystallinity and $W\%$ is the water fraction.

5.3.4 Mechanical tests

To investigate the yield and failure kinetics, uniaxial tensile and creep tests were performed using a Zwick Universal Testing Machine equipped with a 1kN load-cell and an environmental chamber with which temperature and relative humidity were controlled. Relative humidity ranged from RH35% to RH75%, strain rates from 10^{-5} s^{-1} up to $3 \cdot 10^{-2} \text{ s}^{-1}$ and temperatures from 23 to 120°C. Each experiment was performed at least two times. As far as the tensile tests are concerned, a pre-load of 0.1 MPa was applied prior the test with a speed of 1mm/min. Subsequently the test was performed with constant strain rate up to an engineering strain of $\approx 50\%$. The creep tests were performed at room temperature (23°C) and three relative humidities (RH35%, RH50% and RH75%). The load was applied within 10 s, then it was kept constant up to failure. At low humidity/temperature, failure occurs by necking, implying that the deformation increases rapidly giving a clear time-to-failure; at high humidity/temperature, deformation may occur homogeneously. In all cases a strain of 35% was chosen as a reference strain for failure.

5.3.5 X-ray diffraction

To investigate the influence of different mold temperatures on structure, X-ray diffraction experiments were performed. First, wide angle X-ray diffraction (WAXD) measurements were done using a Ganesha X-ray instrument equipped with a GeniX-Cu ultra low divergence source ($\lambda = 1.54 \text{ \AA}$) and a Pilatus 300K silicon pixel detector (487 x 619 pixels of $172 \times 172 \mu\text{m}^2$). The patterns obtained were radially integrated and the weight percentage crystallinity was estimated by:

$$\chi_c = \frac{T - A}{T} \quad (5.6)$$

where T is the total scattered intensity and A is the scattering from the amorphous halo. The amorphous halo was retrieved performing WAXD on a completely amorphous sample obtained by quenching the material in water with ice and NaCl. However, especially in the case of injection molding, the material can crystallize in a mixture of α and γ . Thus the total crystallinity calculated by equation 5.6 may actually consist of a fraction related to the

α -phase and another fraction related to γ -mesophase. Therefore, a deconvolution analysis is performed. It consist of an analytical fitting of Lorentzian's functions to the characteristics peaks. Next, all the function areas are summed up to the amorphous halo area, and the resulting pattern is compared to the experimental result. The α -phase and γ -mesophase fractions follow from:

$$\chi_{c,\alpha} = \frac{A_\alpha}{A_m} \quad \text{and} \quad \chi_{c,\gamma} = \frac{A_\gamma}{A_m} \quad (5.7)$$

where A_α and A_γ are the total area of the Lorentzian functions for the α and γ peaks, and A_m is the total area of the measured pattern. Also, small angle X-ray scattering (SAXS) was performed on the same setup described for WAXD, only the samples to detector distance was increased. With SAXS, the difference of electronic density are detected, i.e. the distance covered by a lamella and an amorphous layer. This is called the long period (L_b). After applying Lorentz [68] and thermal density fluctuation [69] corrections, the long period is calculated with:

$$L_b = \frac{2\pi}{d^*} \quad (5.8)$$

where d^* is the peak position expressed in inversed nanometer (nm^{-1}). Next, the lamellar thickness (l_c) is estimated by:

$$l_c = \chi_{vol} \cdot l_b \quad (5.9)$$

where χ_{vol} is the volumetric crystallinity percentage, which takes into account the different density of amorphous phase and the two polymorphs (α and γ):

$$\chi_{vol} = \frac{\frac{\chi_c}{\rho_c}}{\frac{\chi_c}{\rho_c} + \frac{100 - \chi_c}{\rho_a}} \quad (5.10)$$

where ρ_c is the density of the crystal (1.21 g/cm^3 for α -phase [21], 1.16 g/cm^3 for γ -mesophase [21]), ρ_a the density of the amorphous (1.09 g/cm^3 [21]) and χ the mass crystallinity. To investigate the influence of shear flow during crystallization, an azimuthal integration (180°) of the SAXS patterns was performed. The Herman's orientation factor [87, 88] was calculated:

$$f_H = \frac{3\langle \cos^2 \phi \rangle - 1}{2} \quad (5.11)$$

where ϕ is the angle between the crystallographic axis and a reference axis, e.g. the machine direction, and $\langle \cos^2 \phi \rangle$ is the average value of cosine square of this angle. $\langle \cos^2 \phi \rangle$ is defined as:

$$\langle \cos^2 \phi \rangle = \frac{\int_0^{\pi/2} I(\phi) \cos^2 \phi \sin \phi \, d\phi}{\int_0^{\pi/2} I(\phi) \sin \phi \, d\phi} \quad (5.12)$$

where $I(\phi)$ is the measured intensity at a given angle ϕ .

5.3.6 Dynamical mechanical thermal analysis

To investigate the influence of processing and relative humidity on the glass transition temperature, a TA instruments Q800 was used to perform dynamical mechanical thermal analysis (DMTA). Flat rectangular samples (main sizes 0.5×5 mm) were tested performing a ramp of temperature from -40°C to 120°C with a heating speed of 3°C/min and a frequency of 1 Hz. The glass transition temperature was defined as the peak of the $\tan(\delta)$ curve.

5.3.7 Dilatometry - PVT

A dilatometer (PVT) able to measure the specific volume of polymers as a function of cooling rate, shear flow, pressure and temperature, was employed [89]. It consists of a pressure cell which combines a traditional “piston-die” type dilatometer with a Couette geometry rheometer. The experiments were performed on ring-shaped samples produced by a mini injection molding machine (Babyplast), with main dimensions: 22 mm outer diameter, 21 mm inner diameter and height of 2.5 mm. To completely erase the thermal history, the sample was heated at 250°C and kept at this temperature for 10 minutes. Then, the cooling procedure was performed for isobaric conditions. Two kind of cooling procedures were applied, ambient cooling ($\approx 0.1^\circ\text{C/s}$) and air cooling ($\approx 1^\circ\text{C/s}$). The pressure was varied in a range from 100 bar to 800 bar and the shear flow in range from 0 s^{-1} to 180 s^{-1} . The influence of shear flow was studied at 200 bar and the shear impulse was applied at 200°C.

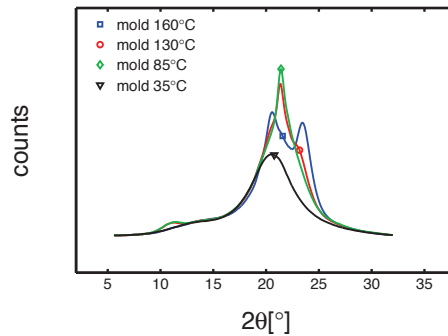
5.4 Results and discussion

5.4.1 Samples characterization

The first step of this study was a crystallographic characterization performed by WAXD and SAXS experiments (details about these techniques are reported in section 5.3.5). WAXD experiments were performed on dry samples to understand the influence of mold temperature. In figure 5.2a, the integrated patterns are reported. It is observed that the mold temperature plays a crucial role on the crystallization: i) at 35°C an almost completely amorphous sample is obtained, ii) at 85°C a predominantly γ -mesophase sample is obtained, iii) at 130°C a mixture of α -phase and γ -mesophase are found and iv) at 160°C a fully α -phase sample is obtained. In figure 5.3b, the results of the deconvolution analysis for dry samples molded at different temperature are shown.

Since it is very common in injection molding that the cross-section displays a variation in morphology, it is important to note that the results of the X-ray analysis are all average over the thickness of the sample.

In figure 5.3a, the deconvolution analysis of samples compression molded at different temperatures are presented. Comparing the results shown in figure 5.3b and 5.3a it possible



(a)

Figure 5.2: WAXD integrated patterns of samples molded at different temperatures; experiments performed at room temperature (23°C) and dry condition.

to notice that in the case of injection molding a full α -phase sample is obtained at a mold temperature of 160°C, while in the case of compression molding mold temperature 160°C a mixture of α and γ was measured. In order to study this effect, we have performed supporting PVT experiments.

Supporting experiments - PVT

A dilatometer (PVT) was employed in order to perform cooling procedures that simulated processing conditions, i.e. crystallization during cooling at high pressures and subjected to shear flows. In figure 5.4a an illustrative example of a PVT result is presented. The sample was cooled at $\approx 1^\circ\text{C}/\text{s}$, with a constant pressure of 200 bar and no shear. The marker (circle) at about 172°C (see figure 5.4a) is defined as the crystallization onset, which is the main outcome of this experiment. As far as the influence of pressure on the crystallization onset temperature is concerned, cooling at two different speeds (0.1 and $1^\circ\text{C}/\text{s}$) was performed for several pressures (from 100 to 800 bar). The crystallization onset for these conditions is plotted as a function of applied pressures, see figure 5.5a. The results show a marked increase of crystallization onset of about 17°C from the minimum to the maximum applied pressure in both the investigated cooling rates.

In the case of crystallization with applied shear flow and constant pressure (100 bar), the crystallization onset increases only a few degrees. Therefore, it is concluded that the different crystallization behavior observed in the injection molding processing, compared to the one seen for compression molding, is mainly due to the effect of pressure which increases the crystallization temperature for a given cooling rate.

Next, SAXS experiments were performed on the dry samples processed at different mold

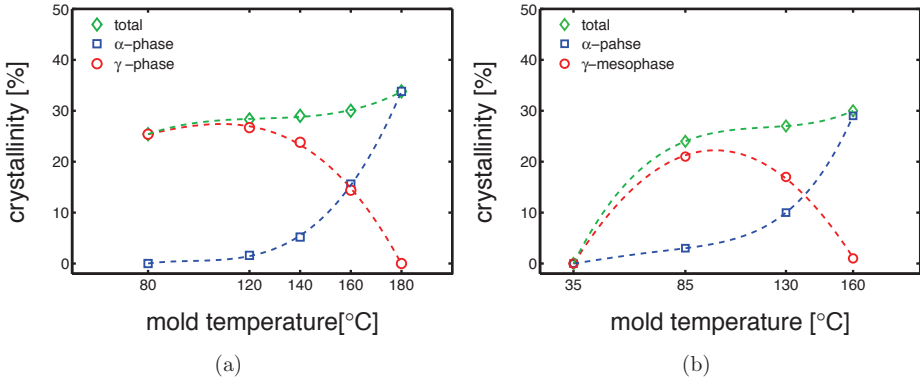


Figure 5.3: Deconvolution analysis of WAXD patterns. Crystallinity, α and γ fractions as functions of mold temperature. a) Case: compression molding, b) case: injection molding.

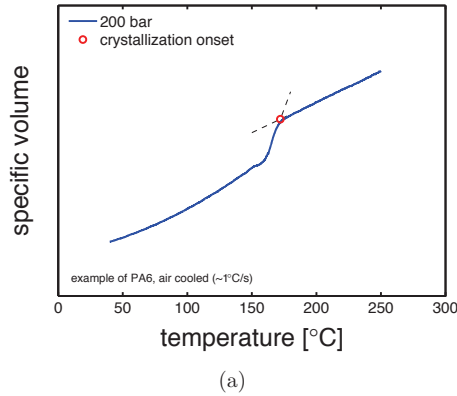


Figure 5.4: Dilatometry-PVT experiment, cooling at $\approx 1^\circ\text{C/s}$ and 200 bar with no shear flow. The circle indicates the crystallization onset temperature.

temperatures. In figure 5.6a, the results of radial integration of the SAXS patterns, which give the required information for to estimating the average long period (l_b) and, as explained in section 5.3.5, the average lamellar thickness (l_c). Figure 5.6b shows the lamellar thickness values as functions of mold temperature; the highest l_c (≈ 2.3 nm) is obtained with mold temperature 160°C and the minimum (≈ 1.6 nm) at mold temperature 85°C.

Effect of flow on the molecular orientation

As mentioned in the introduction, flow may lead to molecular orientation and this could affect the mechanical properties. To investigate the whether or not orientation was present,

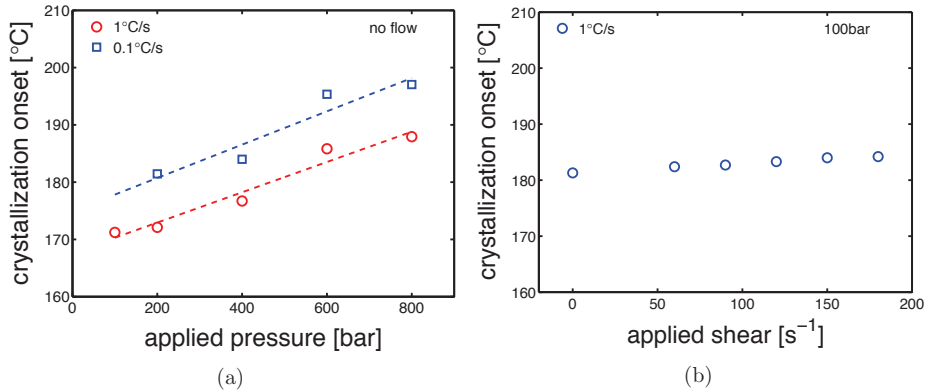


Figure 5.5: (a). Crystallization onset temperature obtained by cooling upon different pressures and cooling rates. Lines are just guides to the eye. b) Crystallization onset temperature obtained by cooling upon different shear flow rates and 100 bar.

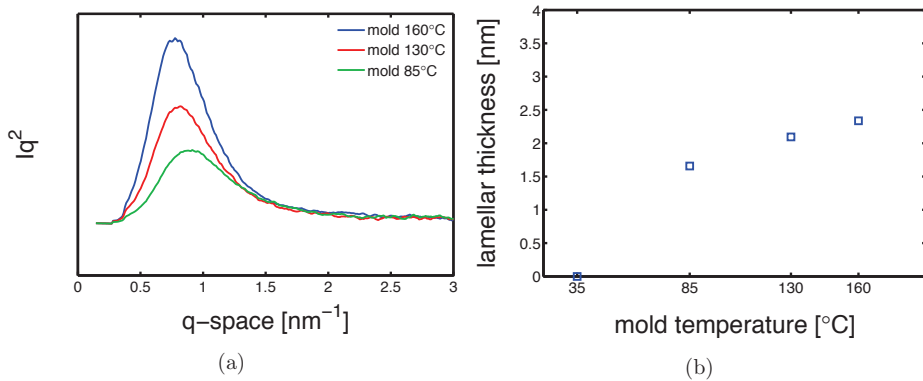


Figure 5.6: (a) SAXS integrated patterns of samples molded at different temperatures; experiments performed at room temperature (23°C) and dry condition. b) Lamellar thickness as a function of mold temperature; experiments performed at room temperature (23°C) and dry condition.

an azimuthal integration of the SAXS pattern was performed. In figure 5.7a three examples of azimuthal integration of samples produced at different mold temperatures and conditioned at RH0% (dry) at room temperature, are shown. A varying orientation is observed for all the three samples; in particular the mold temperature 85°C shows two clear maximums at approximately 90° and 270°. In figure 5.7b the Herman's orientation factor is plotted as a function of mold temperature; the Herman's orientation factor is zero for a fully random orientation, and 1 or -0.5 for a sample fully oriented parallel and perpendicular to the machine direction, respectively.

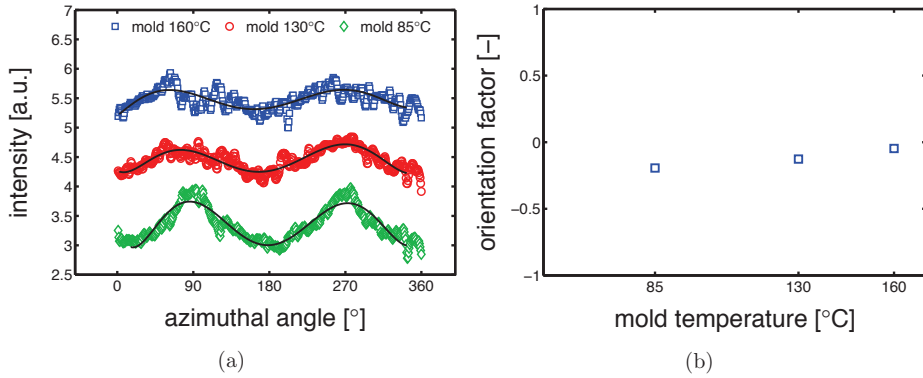


Figure 5.7: a) Azimuthal integration over a range from 0° to 180° of samples at dry conditions and room temperature. The solid lines are guide to the eye. b) Herman's orientation factor as a function of mold temperature.

The results in figure 5.7b show a modest orientation in the case of a mold temperature of 85°C, while an almost fully random sample is obtained by performing injection molding at higher temperatures (130°C and 160°C). Therefore, the mechanical properties of samples cut in parallel and perpendicular direction compare to the flow direction, were tested by tensile tests at different strain rates. The stress-strain response of “parallel” and “perpendicular” sample molded at 160°C are presented in figure 5.8a. Astonishingly, both the “parallel” and “perpendicular” samples showed approximately the same yield stress (± 1 MPa), see figure 5.8b. The same observations were made for the samples molded at 85°C, see figures 5.9a and 5.9b. Observing the behavior post-yield in figure 5.8a, it is possible to see a difference between “parallel” and “perpendicular” samples. However, the post-yield behavior of tensile tests can not be controlled, because of the strain localization which takes place after yield.

5.4.2 Yield kinetics

Because of the absence of effect of the orientation on the mechanical properties, the study continued on “parallel” samples only. The mechanical characterization continued with the investigation of yield kinetics for dry conditions. Uniaxial tensile test were performed in a range of temperatures from 23°C to 80°C and strain rates from $3 \cdot 10^{-4}$ up to $3 \cdot 10^{-2} s^{-1}$. In figures 5.10a, 5.10b, 5.11a and 5.11b, examples of stress-strain response at different temperatures are presented for mold temperature of 160°C, 130°C, 85°C and 35°C respectively. As expected, the yield stress increases for increasing strain rates and decreases for increasing temperature. However, this statement does not hold for the samples molded at 35°C. For these, the increase of temperature from 23°C to 47.5°C leads rapidly to a dramatic drop of yield stress (from ≈ 70 MPa to ≈ 5 MPa), while increasing the temperature to above T_g , the measured yield stress

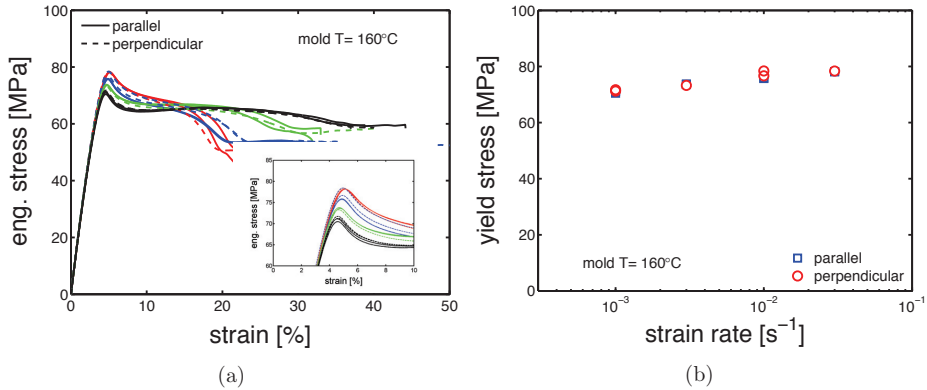


Figure 5.8: a) Tensile tests at strain rate from 10^{-3} s^{-1} to $3 \cdot 10^{-2} \text{ s}^{-1}$ at 23°C ; comparison between samples cut in parallel (solid lines) and perpendicular (dashed lines) direction compare to the flow. b) Yield stress as a function of strain rate. Samples molded at 160°C .

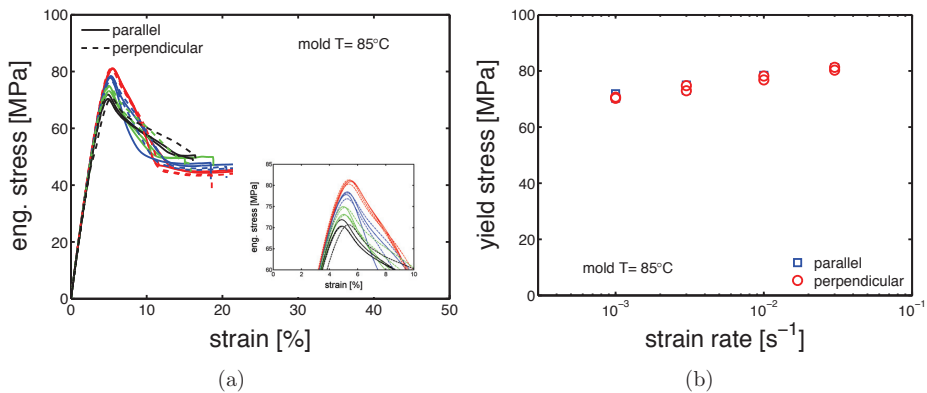


Figure 5.9: a) Tensile tests at strain rate from 10^{-3} s^{-1} to $3 \cdot 10^{-2} \text{ s}^{-1}$ and 23°C ; comparison between samples cut in parallel (solid lines) and perpendicular (dashed lines) direction compare to the flow. b) Yield stress as a function of strain rate. Samples molded at 85°C .

risers up to $\approx 20 \text{ MPa}$, see figure 5.11b. This is a clear indication of the evolution of the sample state. Indeed, the samples molded at 35°C are almost completely amorphous samples, see figure 5.2a. Heating an amorphous samples above its T_g causes cold crystallization and, consequently an enhancement of the yield stress is obtained. This effect is also visible in the DMTA experiments which are presented later on (see figure 5.16a). The results for a mold temperature of 160°C showed the weakest dependence on testing temperature and strain rate, while 85°C showed the strongest.

In figures 5.12a, 5.12b, 5.13a and 5.13b, the yield kinetics (yield stress as a function of

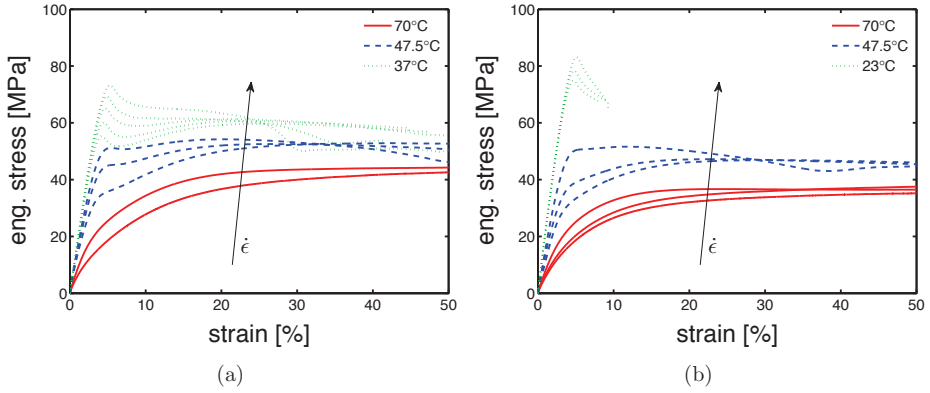


Figure 5.10: Stress-strain response at different temperatures and strain rates of samples molded at a) 160°C and b) 130°C.

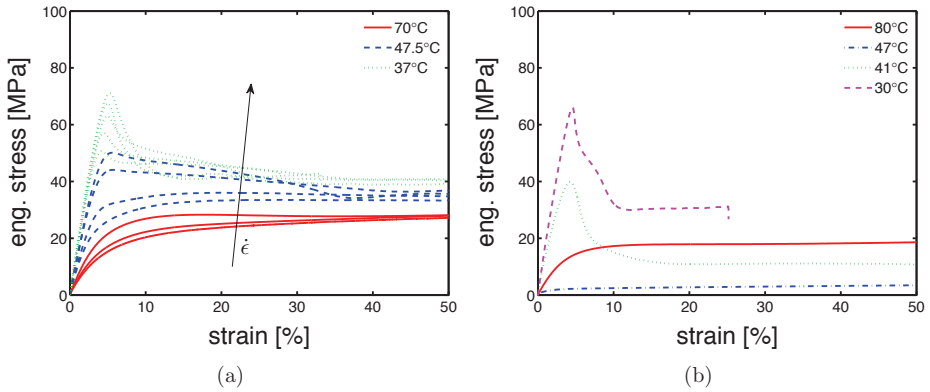


Figure 5.11: Stress-strain response at different temperatures and strain rates of samples molded at a) 85°C and b) 35°C.

strain rate) of dry samples are given. For the cases of samples molded at 160°C and 130°C, in which α -phase (160°C) and γ -mesophase (130°C) are predominant, predictions based on equation 5.2 (\tilde{T} is just the testing temperature since $T_{g,i} = T_{g,dry}$) using parameters listed in table 5.1 for mold 160°C and table 5.2 for 130°C are given by the lines in figures 5.12a and 5.12b. The rate factors are defined accordingly to the best fitting, see tables 5.3, 5.4 and 5.5. The lines match the experimental results rather well for these two cases. However, for a mold temperature of 85°C, a clear mismatch between the prediction and the experimental results is found, see figure 5.13a. In this case, the parameters related to γ -mesophase are employed. However, it is evident that the strain rate and temperature dependence of the yield stress

	$\dot{\epsilon}_0$ [s^{-1}]
I	$7 \cdot e119$
II	$6 \cdot e45$

Table 5.3: Ree-Eyring parameters: rate factors for samples molded at 160°C.

	$\dot{\epsilon}_0$ [s^{-1}]
I	$1 \cdot e123$
II	$4 \cdot e45$

Table 5.4: Ree-Eyring parameters: rate factors for samples molded at 130°C.

	$\dot{\epsilon}_0$ [s^{-1}]
I	$1 \cdot e130$
II	$6 \cdot e45$

Table 5.5: Ree-Eyring parameters: rate factors for samples molded at 85°C.

is stronger than in the case of a mold temperature of 130°C and 160°C. This difference is even more clear for the results obtained at 37°C, see figure 5.13a. Figure 5.11b shows the stress-strain response of samples molded at 35°C; the results obtained in this case are far from what found for a mold temperatures of 130°C and 160°C.

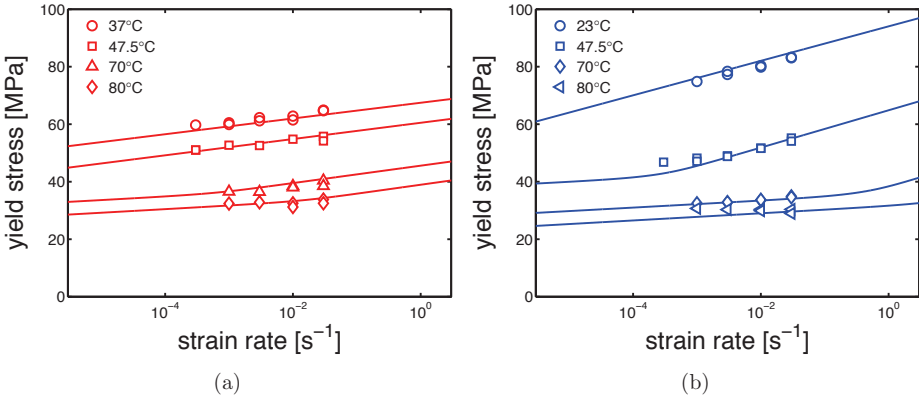


Figure 5.12: Yield kinetics (yield stress as a function of strain rate) of samples in dry condition, molded at a) 160°C b) 130°C. Lines are the the results of the Ree-Eyring equation.

Remarkably, comparing results for a mold temperature of 85°C (figure 5.13a) and a mold temperature of 35°C (figure 5.13b), a very similar strain rate dependence (slope) of the yield stress is found at low temperatures, see figure 5.15a. The reason of this behavior might be found by considering the samples inhomogeneity. As previously explained, injection molding samples show a non-homogeneous morphology along the thickness. It is likely that, in the case of mold temperature 85°C, the skin layer (i.e. the outermost layer) is thicker than in the case of 130°C and 160°C, and thus a predominant contribution of the skin layer leads to a behavior closer to an amorphous sample rather than a semi-crystalline.

5.4.3 Structures-properties relations for modelling

As mentioned in section 5.2, a previous study on samples crystallized quiescently, a relation between the lamellar thickness and the rate factors ($\dot{\epsilon}_{0,I,II}$) was proposed. In figures 5.14a

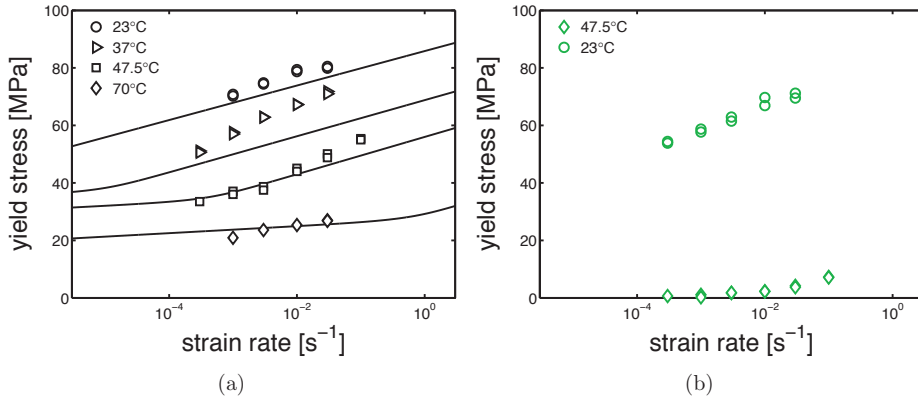


Figure 5.13: Yield kinetics (yield stress as a function of strain rate) of samples in dry condition, molded at a) 85°C b) 35°C. Lines are the the results of the Reo-Eyring equation.

and 5.14b, the rate factors I and II defined for the samples processed by injection molding are plotted as functions of lamellar thickness together with the rate factors obtained for compression molding. In the case of the rate factor I, the injection molding markers are in good agreement with the trend obtained in the case of compression molding, see 5.14a. Plotting the $\dot{\epsilon}_{0,II}$ obtained for injection molding samples as a function of lamellar thickness, values are in line with trend found for compression molding, see figure 5.14b. However, because of the mixture of α and γ crystals present in the sample molded by injection molding, the trends might results not perfectly in line with the polymorph division (see dashed lines in figure 5.14b).

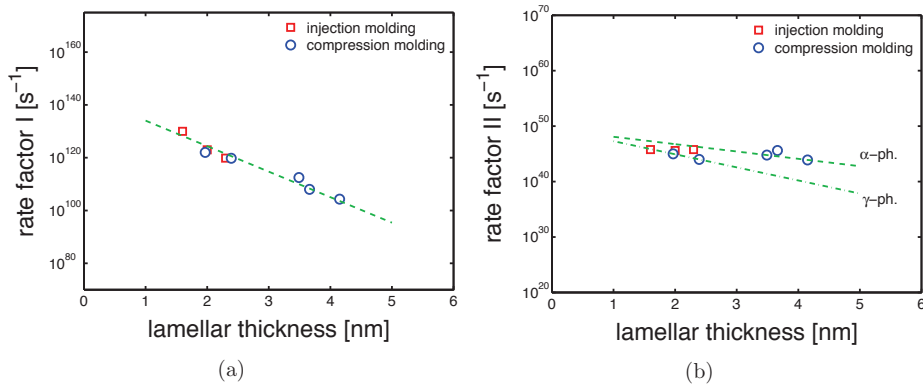


Figure 5.14: a) Rate factor I and b) rate factor II as functions of lamellar thickness. Lines are guides to the eye.

5.4.4 Influence of temperature

In figure 5.15b, the yield stress obtained by tensile test at strain rate 10^{-2} s^{-1} is plotted as a function of temperature in a range from 23°C to 120°C . This figure shows clearly the behavior of the samples molded at 35°C when tested at higher temperatures: at temperatures lower than $\approx 40^\circ\text{C}$ yield stress is slightly lower than the other samples molded at higher temperatures. Above $\approx 40^\circ\text{C}$ the yield stress decreases rapidly down to a minimum of about 5 MPa at 47.5°C ; increasing the temperature further, the yield stress increases again and at about 80°C it reaches a plateau that continues up to the highest temperature investigated (120°C). The samples molded at 130°C and 160°C show a similar behavior if plotted as function of temperature. The absolute value is slightly higher in the case of a mold temperature 160°C and 130°C . This is due to a larger lamellar thickness. At testing temperatures between 23°C and $\approx 45^\circ\text{C}$, the samples molded at 85°C show an yield stress comparable with mold 130°C and 160°C ; above $\approx 45^\circ\text{C}$, the yield stress drops moderately till a minimum at is reached 120°C , see figure 5.15b.

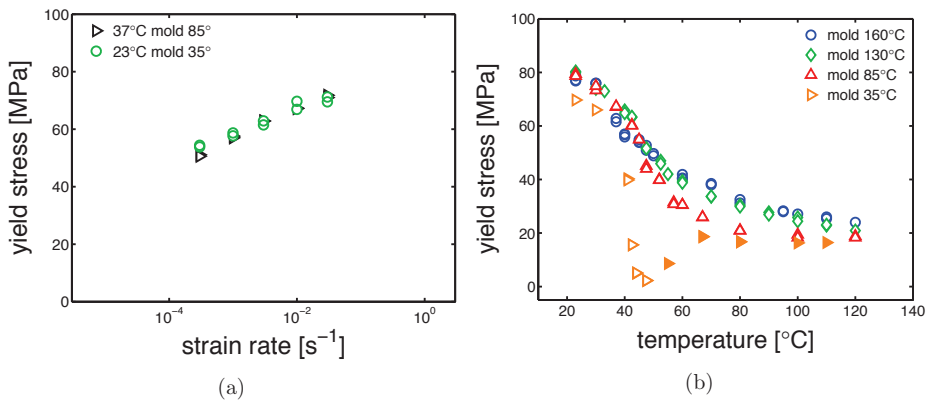


Figure 5.15: a) Comparison between the yield kinetics of samples molded at 85°C and 35°C . b) Yield stress as a function of temperature. In the case of the samples molded at 35°C , the transition from unfilled to filled markers, is due to the fact that after $\approx 45^\circ\text{C}$ the samples start to cold-crystallize. Thus, the filled markers are not really representative of the samples molded at 35°C but an evolution of those. Strain rate 10^{-2} s^{-1} .

5.4.5 Influence of the conditioning environment

The glass transition temperatures were measured by DMTA, after conditioning at a relative humidity 35, 50 and 75% at room temperature (23°C). The results are shown in figures 5.16a, 5.16b, 5.17a and 5.17b. The T_g values are reported in table 5.6. In figure 5.16a, the cold crystallization previously mentioned, is clearly visible by observing the curve related to the

dry sample at $\approx 60^\circ\text{C}$.

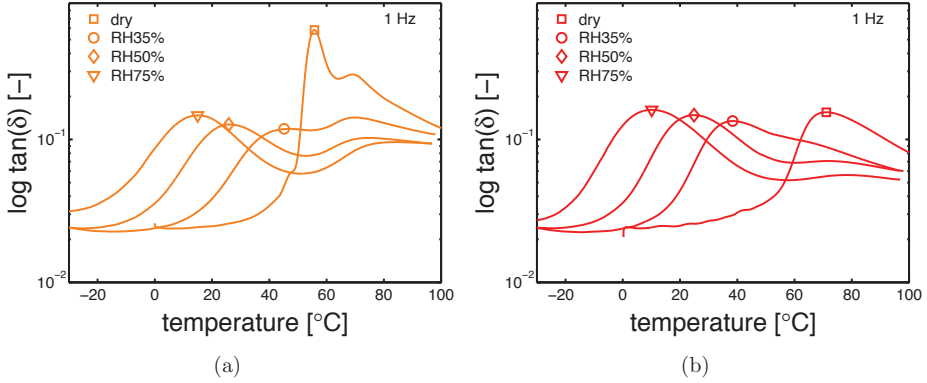


Figure 5.16: DMTA experiments for samples conditioned at different relative humidities, $\tan(\delta)$ as a function temperature for samples molded at a) 35°C and b) 85°C . Markers indicate the measured T_g 's.

The DMTA results for the samples that are conditioned at different humidities are vital in order to determine the “apparent” temperature (equation 5.1), see section 5.2. The markers indicate the estimated glass transition temperatures.

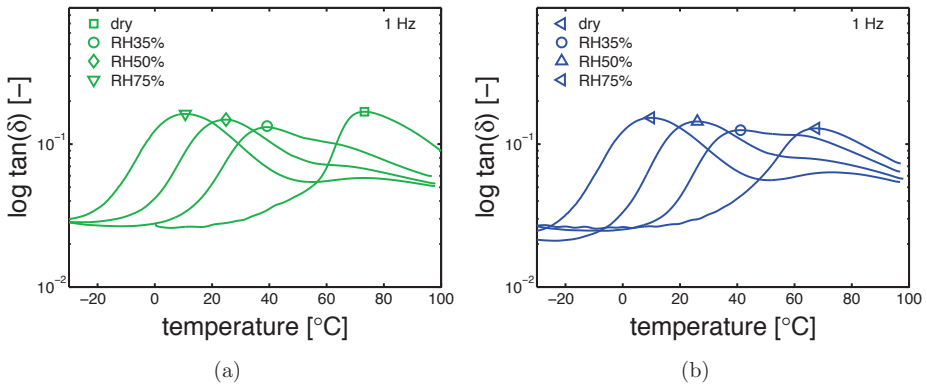


Figure 5.17: DMTA experiments for samples conditioned at different relative humidities, $\tan(\delta)$ as a function temperature for samples molded at a) 130°C and b) 160°C . Markers are the selected T_g .

The glass transition temperatures are given as a function of the relative humidity (during conditioning), see figure 5.18a. The largest differences in glass transition temperature are found in the case of a mold temperature 35°C and dry condition. After conditioning, all the samples show a very similar T_g . The measured T_g are reported in table 5.6. Finally, the glass transition temperatures can be also plotted as functions of normalized water fraction (see

equation 5.5), which takes into account that only the amorphous fraction can absorb water [12]. Figure 5.18b shows that, when plotting T_g as a function of normalized water fraction, all the results are captured by a monotonic descending trend line.

Table 5.6: Glass transition temperature [°C].

sample	dry	35RH%	50RH%	75RH%
mold 160°C	68	41	26	10
mold 130°C	73	39	25	11
mold 85°C	71	38	25	10
mold 35°C	56	45	26	15

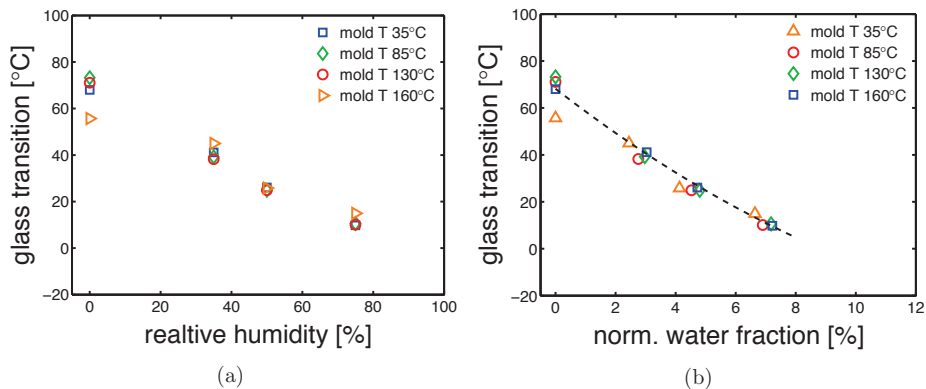


Figure 5.18: Glass transition temperatures as functions of a) relative humidities and b) normalized absorbed water fraction. The line is a guide to the eye.

Hydration-induced crystallographic evolution

In order to check the influence of hydration on the crystallographic properties, WAXD experiments were carried out on conditioned samples. In figures 5.19a, 5.20a, 5.21a and 5.22a, the integrated patterns are shown for the case of mold 160°C, 130°C, 85°C and 35°C; the corresponding deconvolution analysis of these patterns are given in figure 5.19b, 5.20b, 5.21b and 5.22b. The drop of glass transition, due to water absorption, has different effects depending on the starting morphology. In the case of a mold temperature of 160°C only a slight increase of crystallinity is recorded, most probably due to secondary crystallization. The samples molded at 130°C show a partial transformation from γ to α -phase and a slight increase of the overall crystallinity. Similar behavior is seen in the case of mold temperature 85°C, see figure 5.21b. Finally, in the case of 35°C, the cold crystallization leads, initially, to the crystallization of γ -mesophase (at RH35%) and at higher relative humidity also the α -phase is crystallized.

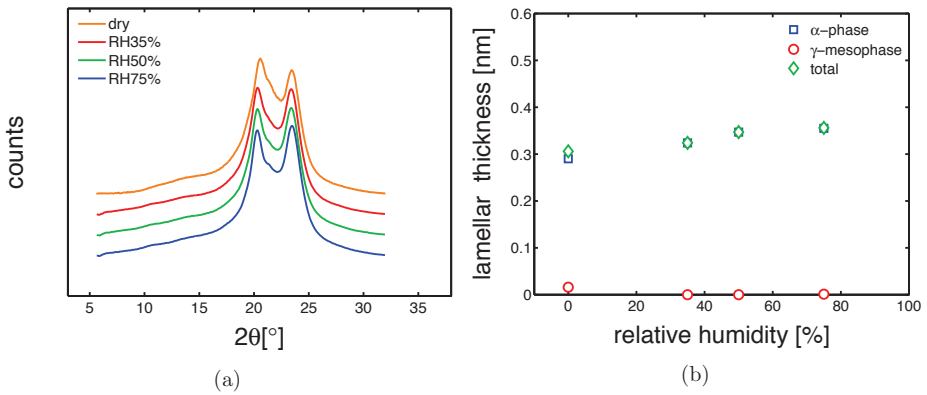


Figure 5.19: a) Wide angle X-ray diffraction integrated patterns, samples molded at 160°C and conditioned at different humidities. b) Deconvolution analysis of the integrated WAXD patterns, crystalline, α and γ fraction as a function of relative humidity.

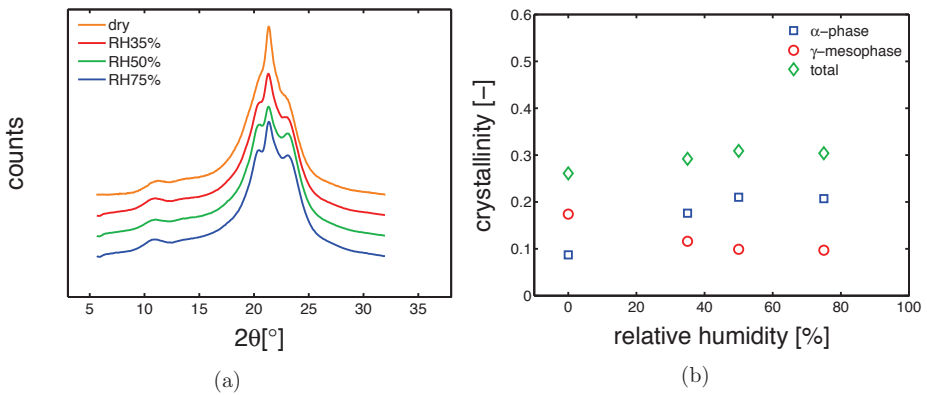


Figure 5.20: a) Wide angle X-ray diffraction integrated patterns, samples molded at 130°C and conditioned at different humidities. b) Deconvolution analysis of the integrated WAXD patterns, crystalline, α and γ fraction as a function of relative humidity.

Effect of water absorption on the mechanical response

After conditioning and determination of the glass transition temperature, uniaxial tensile tests were performed in environments with controlled temperature and relative humidity. The temperature was kept constant at 23°C and three relative humidities were selected, RH35%, RH50% and RH75%. In figure 5.23a, an example of the effect of humidity on the stress-strain response of samples molded at 130°C is presented. As already mentioned, the increase of relative humidity leads to a decrease of mechanical response. The yield stress values

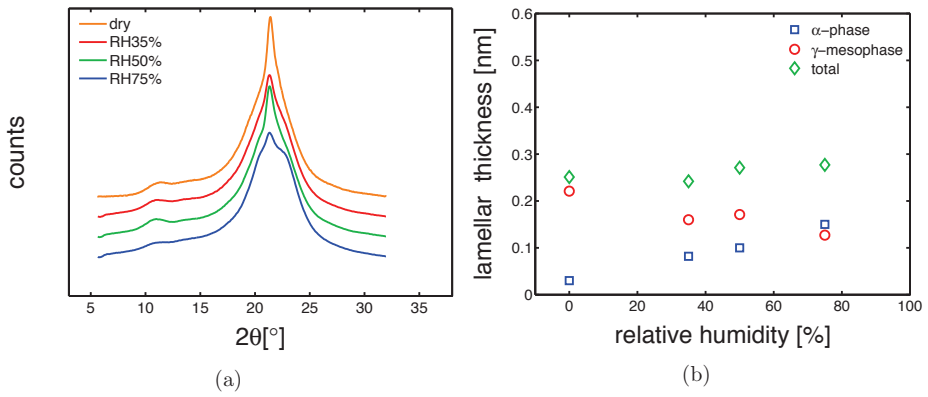


Figure 5.21: a) Wide angle X-ray diffraction integrated patterns, samples molded at 85°C and conditioned at different humidities. b) Deconvolution analysis of the integrated WAXD patterns, crystalline, α and γ fraction as a function of relative humidity.

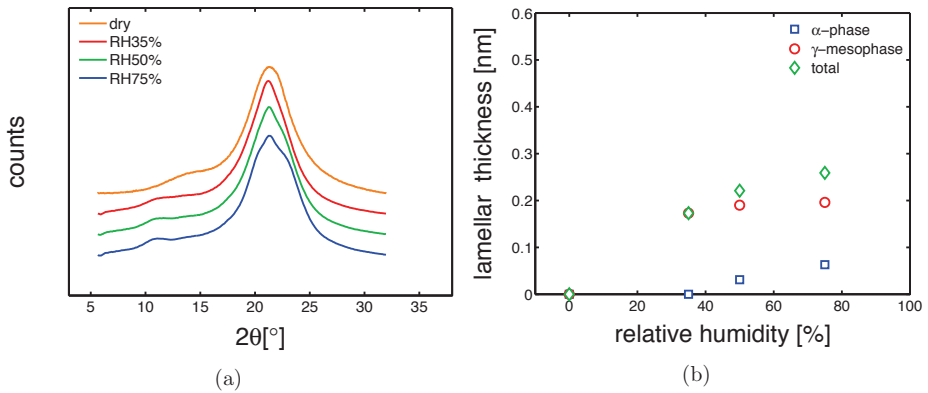


Figure 5.22: a) Wide angle X-ray diffraction integrated patterns, samples molded at 35°C and conditioned at different humidities. b) Deconvolution analysis of the integrated WAXD patterns, crystalline, α and γ fraction as a function relative humidity.

obtained at different relative humidity are plotted as function of the applied strain rate, see figure 5.23b. The symbols are the values obtained experimentally, whereas the lines are the predictions based on the equation 5.2 in which, in order to include the influence of RH% on the mechanical properties, the temperature was replaced by the “apparent” temperature equation. TGhe agreement is excellent. The yield kinetics for samples molded at 160°C and 85°C are shown in figures 5.24a and 5.24b, respectively. As in the case of dry samples, the predictions made for samples molded at 160°C and 130°C match quite well the experimental

results. Even for the 85°C mold temperature case, for which the agreement between model and experiment was not satisfactory for dry condition the description (lines) are not too far from the experimental results. Our explanation for this result is the effect of hydration on the crystallographic properties. As explained previously, because of the drop of glass transition due to hydration, cold crystallization is observed in the case of amorphous (quenched) samples. Thus, the amorphous skin layer of the samples molded at 85°C are likely to cold-crystallize in γ -mesophase, see figure 5.22b. Consequently, a decreased amorphous contribution on the mechanical properties is obtained and by the use of the parameters for γ -phase, a rather good description is obtained. Moreover, the hydration-induced drop of T_g decreases the mechanical contribution of the amorphous regions.

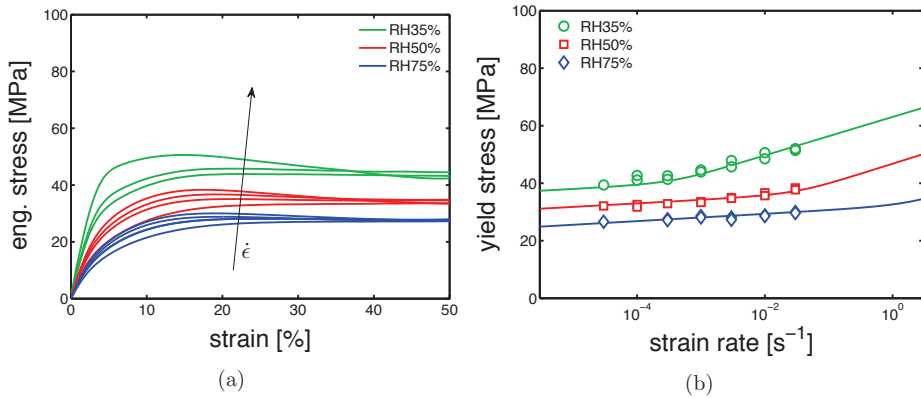


Figure 5.23: a) Stress-strain response of samples conditioned at different relative humidities and tested at strain rate in a range from $3 \cdot 10^{-5} \text{ s}^{-1}$ to $3 \cdot 10^{-2} \text{ s}^{-1}$. b) Yield stress kinetics of samples molded at 130°C.

5.4.6 Creep tests

Finally, creep test at different relative humidity were performed. The samples were tested at 23°C and different loads were applied. The time-to-failure (t-t-f) was defined as the time to reach a strain of 35%, and the plastic flow rate is calculated by selecting the minimum in the Sherby-Dorn plot [43]. Subsequently, from the plastic flow rates, plotted as functions of the corresponding measured time-to-failure in a bi-logarithmic plot, the critical strain (ϵ_{cr}) is determined, as explained in [42, 79, 86]. Different ϵ_{cr} were estimated for different thermal histories (i.e. mold temperatures) and different conditioning (RH%); for each mold temperature, an average critical strain (ϵ_{cr}) was defined, see table 5.7.

Next, using the predictions made for the yield kinetics, equation 5.3 was applied. In figures 5.25a, 5.25b and 5.26, the results of creep tests at different relative humidity and

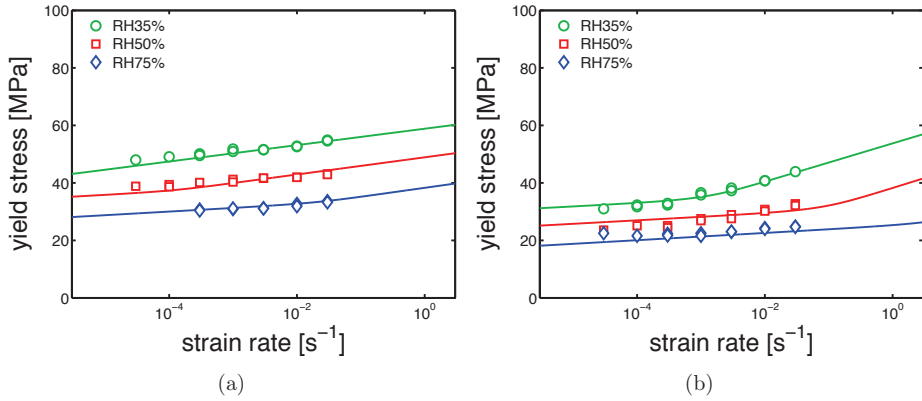


Figure 5.24: Yield stress kinetics of samples conditioned at 23°C different relative humidities and molded at a) 160°C and b) 85°C.

	mold 35°C	mold 85°C	mold 130°C	mold 160°C
ϵ_{cr}	-	0.15	0.28	0.11

Table 5.7: Average critical strains obtained at different relative humidities.

several applied load are shown for the samples injection molded at 160°C, 130°C and 85°C, respectively.

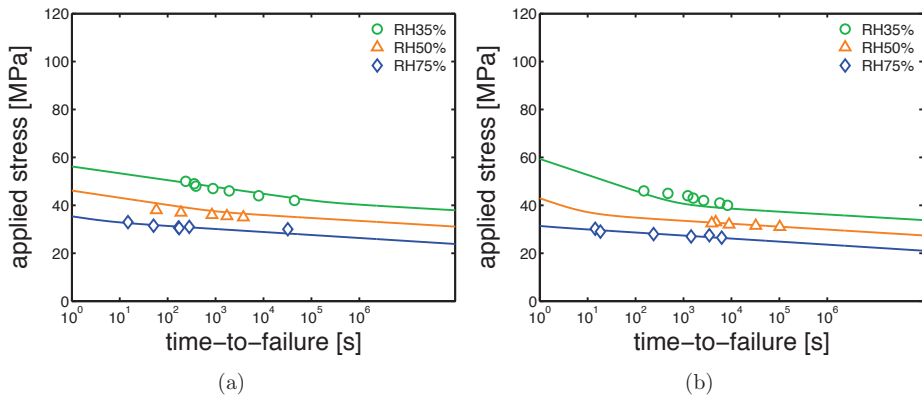


Figure 5.25: Creep tests, applied load as a function of time-to-failure for samples conditioned at different relative humidities and room temperature. The lines are the results of equation 5.3. a) Mold temperature 160°C and b) 130°C.

The experimental results for mold temperatures of 160°C and 130°C are well described by

the model (see figure 5.25a and 5.25b). However, in the case of a mold temperature of 85°C, the predictions made for the samples conditioned at relative humidity 35%, do not match the experimental values, see figure 5.26. We can only speculate about this mismatch.

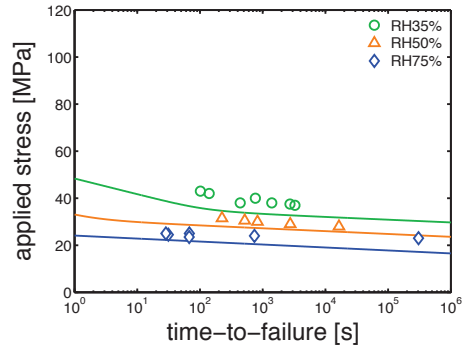


Figure 5.26: Creep tests, applied load as a function of time-to-failure for samples conditioned at different relative humidities and room temperature. The lines are the results of equation 5.3. Mold temperature 85°C.

5.5 Conclusions

In this study, an industrial injection molding machine was used to produce polyamide 6 samples with different crystallographic properties. The mold temperature was varied in a range from 35 to 160°C. A clear influence of mold temperature on the crystallization was detected. In the investigated range of temperatures, different crystallinity values, lamellar thicknesses and crystal polymorphs were obtained. Moreover, also the effect of shear flow and pressure during crystallization were studied by dilatometry (PVT). This led to the conclusion that the well known shift of the crystallization to higher temperature is dominant, while shear flow has a minor effect on crystallization kinetics. The effect of pressure during injection molding was particularly highlighted by a deconvolution analysis performed on WAXD patterns obtained for samples made with different mold temperatures that were compared with samples obtained by compression molding (in which pressure and shear flow are negligible). It was found that in the case of injection molding, even at a mold temperature of 160°C, a fully α -phase sample was obtained; while in the case of compression molding at the same temperature, a mixture of α and γ was obtained. This effect was ascribed to the high pressure present during cooling in the case of injection molding. By azimuthal integration, the presence of molecular orientation was measured. A weak orientation was found but, remarkably, the mechanical properties did not show an influence of the orientation. The mechanical properties were tested by uniaxial tensile tests and uniaxial creep tests at several temperature in dry condition and at room temperature with varying relative humidity. The Eyring's flow model, modified with the apparent temperature and combined with the concept of critical strain, were employed in order to describe the results obtained by tensile and creep tests. This was partially successful. In the case of samples molded at 160°C and 130°C, the model was successfully applied by the use of parameters previously determined as characteristic in the case of α -phase and γ -mesophase, respectively. In the case of mold temperature 85°C, it was hypothesized that the inhomogeneous morphology (intrinsically induced by the molding technique) led to a too large contribution of the amorphous layer (skin layer). Finally, in the case of mold temperature 35°C, in which completely amorphous samples were obtained, a description was not achieved due to the continuous development of the micro-structure.

5.6 Acknowledgments

This work is part of the Research Program of the Dutch Polymer Institute DPI, Eindhoven, the Netherlands, project number #786. The authors thank the "Institute for Complex Molecular Systems" (ICMS) of Eindhoven, The Netherlands for providing the X-ray facility and Marco M.R.M Hendrix for assisting the experiments.

Chapter 6

Conclusions and recommendations

This thesis aimed to understand the relations between structure and properties in polyamide 6, moved specifically by the need to develop an experimental knowhow that will be the base for a complete unified model able to predict properties starting from a given thermal history. In this chapter, the main conclusions and recommendations are given.

6.1 Conclusions

Prediction of plasticity-controlled failure in polyamide 6: influence of temperature and relative humidity

- The mechanical response of PA6 is characterized by the presence of two different molecular processes: an intra-lamellar (process I) and an inter-lamellar (process II).
- To capture the pronounced influence of humidity, the Ree-Eyring equation had to be modified in order to include the influence of relative humidity. The modification consisted in the replacement of the temperature with the “apparent temperature” (\tilde{T}). The \tilde{T} equation associates the hydration-induced drop of the glass transition temperature with an “apparent” enhancement of temperature. By this model, a successful description of the yield kinetics obtained experimentally by tensile test at different temperatures and relative humidity, was achieved.
- The “critical strain” concept was adopted and combined with the modified Ree-Eyring equation, allowing a successful description of creep tests performed at different relative humidities.

Glass transition temperature versus structure of polyamide 6: a flash-DSC study

- The glass transition temperature of dry samples solidified in different ways, was studied by the mean of a fast scanning calorimeter (flash-DSC). An influence of the solidification procedure on T_g was experimentally demonstrated.

- The influence of the solidification procedure on the T_g was attributed to the formation of the rigid amorphous fraction (RAF). Generally, higher RAF content leads to higher T_g . Two equations able to predict the content of RAF and mobile amorphous fraction MAF for a given lamellar thickness (l_c), space filling index (ξ) and crystallinity degree (χ_c) were proposed. The equations are based on the simple idea that, the RAF content is related to the crystal surface available for RAF formation.
- Another equation that links the RAF-MAF ratio with the glass transition temperature was proposed. With this, the final glass transition temperature was calculated accordingly to the RAF-MAF ratio and two parameters: the T_g of the mobile amorphous phase (obtained experimentally) and the T_g of the rigid amorphous phase which was set as an arbitrary parameter.

Structure-properties relations in polyamide 6 processed in quiescent condition: influence of the thermal history on the deformation and failure kinetics

- The investigation showed that α -phase had the highest mechanical response, even at high temperatures, while the response of the amorphous samples was strongly affected by temperature increase and the γ -mesophase samples showed an intermediate response.
- The influence of humidity absorption on the crystallographic properties was studied by WAXD and SAXS. The experimental results showed that α is the most stable phase, while γ is subjected to partial transformation upon hydration. The amorphous samples have shown the occurrence of cold crystallization, which at low RH% led to crystallization of γ -mesophase while α -phase was predominant at high RH%.
- The model proposed in chapter 2 was applied to the case of different polymorphism and lamellar thicknesses. In order to make this possible, two sets of Eyring parameters, identical for the intra-lamellar deformation process and different for the inter-lamellar ones, were defined. The relation between l_c and the yield stress was captured by varying the rate factors. Plotting the rate factors as functions of the corresponding lamellar thickness, a linear trend was found.

Injection molding of polyamide 6: influence of mold temperature on the yield and failure kinetics at different environmental conditions

- The role of mold temperature in injection molding processing was studied with respect to the structures and the mechanical response. A strong influence of mold T on structures was found: i) low mold temperatures ($\approx 35^\circ\text{C}$) led to (almost) completely amorphous samples, characterized by a micro-structure strongly influenced by hydration and temperature; ii) for intermediate mold temperatures (80-130°C), a mixture of α and γ was found. In this case, the γ -mesophase partially transform into the more stable α -phase

upon hydration ; iii) at high temperature ($\approx 160^\circ\text{C}$), the samples crystallized in the most stable α -phase. For tests at low temperatures (23°C to $\approx 45^\circ\text{C}$), the mechanical responses of all the samples were found alike (a part for 35°C). For tests at higher temperatures ($>45^\circ\text{C}$) the mechanical response scaled mainly with the lamellar thickness. The higher the lamellar thickness, the higher the yield stress.

- The effect of pressure and shear flow on the crystallization was investigated. A clear influence of pressure on the crystallization onset was found; high pressure led to higher crystallization T. These explain the predominance of α -phase in samples crystallized at temperatures at which in the case of compression molding, mainly γ is obtained.
- The application of the model introduced in chapter 2 was possible for the samples molded at 160°C and 130°C but only partially at 85°C . The reason of this partial success is attributed the inhomogeneous morphology of the samples; in particular the hypothesized presence of a thick amorphous skin layer in the case of sample molded at 85°C , which led to a response closer to an amorphous sample rather than a γ one.
- From a performance point of view, it is stated that the use of high mold temperatures lead to high mechanical response (yield and time-to-failure) and, in particular, to less temperature and moisture dependent response.

6.2 Recommendations

In this section, some recommendations or future works are proposed:

- In chapter 2 the Ree-Eyring equation was used to describe the results of yield stress at dry condition, fixed strain rate and a wide range of temperatures. In this instance, two recommendations are proposed: i) the strain localization phenomenon (necking) strongly influence the engineering stress-strain response, thus it is recommended to extend the study to true stress-true strain (compression test). ii) The yield stress showed a flattening at high temperatures which was due to lamellar thickening. In future, a further modification of the Ree-Eyring eq. to include the effect of temperature on the lamellar thickness (so called annealing), should be made.
- in chapter 3, two equations able to predict the fractions of RAF and MAF as functions of crystallinity, lamellar thickness and RAF thickness, are proposed. In the non-isothermal case, crystallization takes place in a range of temperatures, leading to a distribution of lamellar thickness. By a supplementary model, the presence of this distribution could be taken into account, giving rise to more accurate prediction of RAF-MAF content. Moreover, the RAF thickness, which was selected as a parameter in this thesis, might be estimated by NMR (Nuclear Magnetic Resonance).

- in chapter 4, the mechanical response of samples processed in several ways was tested in different environments. The quenched samples showed a time- temperature- humidity-activated cold crystallization. To predict the level of crystallinity and l_c of cold crystallized samples, the kinetics of this phenomenon could be studied and linked to the increase of yield stress at the scope to be included in the model.
- Chapter 5 was dedicated to a more industrial application, i.e. injection molding. This techniques revealed a main toughness: the morphological inhomogeneity of the samples. This is piratically unavoidable when producing the samples by such a complex processing. However, it is pointed out that, in case of high mold temperatures, the samples appeared to be more homogeneous, allowing a better prediction of the mechanical response. Moreover, at high mold T (for instance 160°), higher χ_c and l_c are formed, consequently higher yield stress and longer time-to-failure are obtained. Thus, the use of high mold temperatures is highly recommended.

References

- [1] Global industry analysts, nylon, a global strategic business report. *http : //www.strategyr.com/NylonMarketReport.asp*, 2010.
- [2] Ceresana. Market study: Engineering plastics (2nd ed.). Technical report, Ceresana Market Intelligence. Consulting., 2016.
- [3] J.A. Brydson. 18 - polyamides and polyimides. In J.A. Brydson, editor, *Plastics Materials (Seventh Edition)*, pages 478 – 530. Butterworth-Heinemann, Oxford, seventh edition edition, 1999.
- [4] Melvin I Kohan et al. *Nylon plastics handbook*, volume 378. Hanser Munich, 1995.
- [5] L. R. Schroeder and S. L. Cooper. Hydrogen bonding in polyamides. *Journal of Applied Physics*, 47(10):4310–4317, 1976.
- [6] E. Vinken, A.E. Terry, S. Hoffmann, B. Vanhaecht, C.E. Koning, and S. Rastogi. Influence of hydrogen bonding on the conformational changes, the brill transition, and lamellae thickening in (co)polyamides. *Macromolecules*, 39(7):2546–2552, 2006.
- [7] D. Cavallo, L. Gardella, G.C. Alfonso, G. Portale, L. Balzano, and R. Androsch. Effect of cooling rate on the crystal/mesophase polymorphism of polyamide 6. *Colloid Polym. Sci.*, 289(9):1073–1079, 2011.
- [8] T.S. Ellis. Moisture-induced plasticization of amorphous polyamides and their blends. *J. Appl. Polym. Sci.*, 36(3):451–466, 1988.
- [9] N.S. Murthy and W.J. Orts. Hydration in semicrystalline polymers: Small-angle neutron scattering studies of the effect of drawing in nylon-6 fibers. *J. Polym. Sci. Part B Polym. Phys.*, 32(16):2695–2703, 1994.
- [10] N. Reuvers, H. Huinink, and O. Adan. Water plasticizes only a small part of the amorphous phase in nylon-6. *Macromol. Rapid Commun.*, 34(11):949–953, 2013.
- [11] H.W. Starkweather. The sorption of water by nylons. *Journal of Applied Polymer Science*, 2(5):129–133, 1959.

- [12] N.S. Murthy. Hydrogen bonding, mobility, and structural transitions in aliphatic polyamides. *J. Polym. Sci., Part B: Polym. Phys.*, 44(13):1763–1782, 2006.
- [13] N.S. Murthy. Glass Transition Temperature and the Nature of the Amorphous Phase in Semicrystalline Polymers: Effects of Drawing, Annealing and Hydration in Polyamide 6. *Int. J. Polym. Mater.*, 50(3-4):429–444, 2001.
- [14] N. Jia, H.A. Fraenkel, and V.A. Kagan. Effects of moisture conditioning methods on mechanical properties of Injection molded Nylon 6. *J. Reinf. Plast. Compos.*, 23(7):729–737, 2004.
- [15] A. Launay, Y. Marco, M.H. Maitournam, and I. Raoult. Modelling the influence of temperature and relative humidity on the time-dependent mechanical behaviour of a short glass fibre reinforced polyamide. *Mech. Mater.*, 56:1–10, 2013.
- [16] N.S. Murthy, M. Stamm, J.P. Sibilica, and S. Krimm. Structural changes accompanying hydration in nylon 6. *Macromolecules*, 22(3):1261–1267, 1989.
- [17] L.E. Govaert, T.A.P. Engels, E.T.J. Klompen, G.W.M. Peters, and H.E.H. Meijer. Processing-induced properties in glassy polymers: Development of the yield stress in pc. *International Polymer Processing*, 20(2):170–177, 2005.
- [18] T.A.P. Engels, L.E. Govaert, G.W. M. Peters, and H.E. H. Meijer. Processing-induced properties in glassy polymers: Application of structural relaxation to yield stress development. *Journal of Polymer Science Part B: Polymer Physics*, 44(8):1212–1225, 2006.
- [19] C.M. Hsiung and M. Cakmak. Effect of processing conditions on the structural gradients developed in injection-molded poly(aryl ether ketone) (paek) parts. i. characterization by microbeam x-ray diffraction technique. *Journal of Applied Polymer Science*, 47(1):125–147, 1993.
- [20] M.R. Kantz, H.D. Newman, and F.H. Stigale. The skin-core morphology and structure-property relationships in injection-molded polypropylene. *Journal of Applied Polymer Science*, 16(5):1249–1260, 1972.
- [21] T.D. Fornes and D.R. Paul. Crystallization behavior of nylon 6 nanocomposites. *Polymer*, 44(14):3945–3961, 2003.
- [22] V. Brucato, S. Piccarolo, and V. La Carrubba. An experimental methodology to study polymer crystallization under processing conditions . The influence of high cooling rates. *Chem. Eng. Sci.*, 57:4129–4143, 2002.
- [23] V. La Carrubba, V. Brucato, and S. Piccarolo. Influence of ”controlled processing conditions” on the solidification of iPP, PET and PA6. *Macromol. Symp.*, 180(1):43–60, 2002.

- [24] D.P. Russell and P.W.R. Beaumont. Structure and properties of injection-moulded nylon-6: Part 1 Structure and morphology of nylon-6. *Journal of Materials Science*, 15:197–207, 1980.
- [25] L. Penel-Pierron, R. Séguéla, J. M. Lefebvre, V. Miri, C. Depecker, M. Jutigny, and J. Pabiot. Structural and mechanical behavior of nylon-6 films. II. Uniaxial and biaxial drawing. *J. Polym. Sci. Part B Polym. Phys.*, 39(11):1224–1236, 2001.
- [26] D.R. Holmes, C.W. Bunn, and D.J. Smith. The crystal structure of polycaproatamide : Nylon 6. *J. Polym. Sci.*, 17:159–177, 1955.
- [27] R. Puffr and J. Šebenda. On the structure and properties of polyamides. XXVII. The mechanism of water sorption in polyamides. *J. Polym. Sci. Part C Polym. Symp.*, 16(1):79–93, 2007.
- [28] I. Boukal. Effect of water on the mechanism of deformation of nylon 6. *J. Appl. Polym. Sci.*, 11(8):1483–1494, 1967.
- [29] V. Miri, O. Persyn, J.-M. Lefebvre, and R. Seguela. Effect of water absorption on the plastic deformation behavior of nylon 6. *Eur. Polym. J.*, 45(3):757–762, 2009.
- [30] H.K. Reimschuessel. Relationships on the effect of water on glass transition temperature and Young’s modulus of nylon 6. *J. Polym. Sci. Polym. chemisrty Ed.*, 16(6):1229–1236, 1978.
- [31] N.S. Murthy, Z.-G. Wang, M.K. Akkapeddi, and B.S. Hsiao. Isothermal crystallization kinetics of nylon 6, blends and copolymers using simultaneous small and wide-angle X-ray measurements. *Polymer*, 43(18):4905–4913, 2002.
- [32] A. Ramkumar and R. Gnanamoorthy. Axial fatigue behaviour of polyamide-6 and polyamide-6 nanocomposites at room temperature. *Compos. Sci. Technol.*, 68(1516):3401–3405, 2008.
- [33] S.C. Bellemare, M.N. Bureau, J. Denault, and J.I. Dickson. Fatigue crack initiation and propagation in polyamide-6 and in polyamide-6 nanocomposites. *Polym. Compos.*, 25(4):433–441, 2004.
- [34] R.W. Lang, A. Stern, and G. Doerner. Applicability and limitations of current lifetime prediction models for thermoplastics pipes under internal pressure. *Die Angewandte Makromolekulare Chemie*, 247(1):131–145, 1997.
- [35] M.D. Skibo, R.W. Hertzberg, J.A. Manson, and S.L. Kim. On the generality of discontinuous fatigue crack growth in glassy polymers. *J. Mater. Sci.*, 12(3):531–542, 1977.

- [36] F. Ramsteiner and T. Armbrust. Fatigue crack growth in polymers. *Polym. Test.*, 20(3):321–327, 2001.
- [37] R.W. Hertzberg and J.A. Manson. *Fatigue of engineering plastics*. Academic press, 1980.
- [38] P.E. Tomlins, B.E. Read, and G.D. Dean. The effect of temperature on creep and physical ageing of poly(vinyl chloride). *Polymer*, 35(20):4376–4381, 1994.
- [39] N. Verheulpen-Heymans and J.C. Bauwens. Effect of stress and temperature on dry craze growth kinetics during low-stress creep of polycarbonate. *J. Mater. Sci.*, 11(1):7–16, 1976.
- [40] C. Bauwens-Crowet, J.-M. Ots, and J.-C. Bauwens. The strain-rate and temperature dependence of yield of polycarbonate in tension, tensile creep and impact tests. *J. Mater. Sci.*, 9(7):1197–1201, 1974.
- [41] H. Eyring. Viscosity, plasticity, and diffusion as examples of absolute reaction rates. *The Journal of Chemical Physics*, 4(4):283–291, 1936.
- [42] M.J.W. Kanters, K. Remerie, and L.E. Govaert. A new protocol for accelerated screening of long-term plasticity-controlled failure of polyethylene pipe grades. *Polym. Eng. Sci.*, 56(6):676–688, 2016.
- [43] O.D. Sherby and J.E. Dorn. Anelastic creep of polymethyl methacrylate. *J. Mech. Phys. Solids*, 6(2):145–162, 1958.
- [44] J.A. Roetling. Yield stress behaviour of isotactic polypropylene. *Polymer*, 7(7):303–306, 1966.
- [45] C. Bauwens-Crowet, J.C. Bauwens, and G. Homés. Tensile yield-stress behavior of glassy polymers. *Journal of Polymer Science Part A-2: Polymer Physics*, 7(4):735–742, 1969.
- [46] T.B. Van Erp, C.T. Reynolds, T. Peijs, J.A.W. Van Dommelen, and L.E. Govaert. Prediction of yield and long-term failure of oriented polypropylene: Kinetics and anisotropy. *J. Polym. Sci., Part B: Polym. Phys.*, 47(20):2026–2035, 2009.
- [47] S. Shoji H. Kawai, H. Takeji and F. Ken-Ich. Dynamic X-ray diffraction studies of spherulitic poly-alpha-olefins in relation to the assignments of alpha and beta mechanical dispersions. *Polymer Engineering & Science*, 24(5):361–372, 1984.
- [48] R. Hiss, S. Hobeika, C. Lynn, and G. Strobl. Network stretching, slip processes, and fragmentation of crystallites during uniaxial drawing of polyethylene and related copolymers. A comparative study. *Macromolecules*, 32(13):4390–4403, 1999.

-
- [49] M.C. Boyce, D.M. Parks, and A.S. Argon. Large inelastic deformation of glassy polymers. Part I: rate dependent constitutive model. *Mech. Mater.*, 7(1):15–33, 1988.
- [50] S.H.M. Söntjens, T.A.P. Engels, T.H. Smit, and L.E. Govaert. Time-dependent failure of amorphous poly-d,l-lactide: Influence of molecular weight. *J. Mech. Behav. Biomed. Mater.*, 13:69–77, 2012.
- [51] X. Jin, T. S. Ellis, and F. E. Karasz. The effect of crystallinity and crosslinking on the depression of the glass transition temperature in nylon 6 by water. *Journal of Polymer Science: Polymer Physics Edition*, 22(10):1701–1717, 1984.
- [52] Y.P. Khanna, W.P. Kuhn, and W.J. Sichina. Reliable Measurements of the Nylon 6 Glass Transition Made Possible by the New Dynamic DSC. *Macromolecules*, 28(8):2644–2646, 1995.
- [53] I. Kolesov, D. Mileva, and R. Androsch. Mechanical behavior and optical transparency of polyamide 6 of different morphology formed by variation of the pathway of crystallization. *Polym. Bull.*, 71(3):581–593, 2014.
- [54] I. Kolesov and R. Androsch. The rigid amorphous fraction of cold-crystallized polyamide 6. *Polymer*, 53(21):4770–4777, 2012.
- [55] B. Wunderlich. Reversible crystallization and the rigid-amorphous phase in semicrystalline macromolecules. *Prog. Polym. Sci.*, 28(3):383–450, 2003.
- [56] C. Schick. Differential scanning calorimetry (DSC) of semicrystalline polymers. *Anal. Bioanal. Chem.*, 395(6):1589–1611, 2009.
- [57] M. Arnoult, E. Dargent, and J.F. Mano. Mobile amorphous phase fragility in semicrystalline polymers: Comparison of {PET} and {PLLA} . *Polymer*, 48(4):1012–1019, 2007.
- [58] C. Schick, A. Wurm, and A. Mohamed. Vitrification and devitrification of the rigid amorphous fraction of semicrystalline polymers revealed from frequency-dependent heat capacity. *Colloid Polym. Sci.*, 279(8):800–806, 2001.
- [59] R. Androsch and B. Wunderlich. The link between rigid amorphous fraction and crystal perfection in cold-crystallized poly(ethylene terephthalate) . *Polymer*, 46(26):12556–12566, 2005.
- [60] D. Mileva, R. Androsch, E. Zhuravlev, and C. Schick. Morphology of mesophase and crystals of polyamide 6 prepared in a fast scanning chip calorimeter. *Polymer*, 53(18):3994–4001, 2012.

- [61] K.-H. Illers. Polymorphie, kristallinitat und schmelzwarme von poly(ϵ -caprolactam), 2. Kalorimetrische untersuchungen. *Die Makromolekulare Chemie*, 179(2):497–507, 1978.
- [62] S.Z.D. Cheng, R. Pan, and B. Wunderlich. Thermal analysis of poly(butylene terephthalate) for heat capacity, rigid-amorphous content, and transition behavior. *Die Makromolekulare Chemie*, 189(10):2443–2458, 1988.
- [63] H. Chen and P. Cebe. Investigation of the rigid amorphous fraction in Nylon-6. *J. Therm. Anal. Calorim.*, 89(2):417–425, 2007.
- [64] J. Menczel and B. Wunderlich. Phase transitions in mesophase macromolecules: The transitions of poly(p-acryloyloxybenzoic acid). *Polymer*, 22(6):778–782, 1981.
- [65] M.C. Righetti and E. Tombari. Crystalline, mobile amorphous and rigid amorphous fractions in poly(l-lactic acid) by tmdsc. *Thermochimica Acta*, 522(1):118 – 127, 2011. Special Issue: Interplay between Nucleation, Crystallization, and the Glass Transition.
- [66] M.C. Righetti, D. Prevosto, and E. Tombari. Time and temperature evolution of the rigid amorphous fraction and differently constrained amorphous fractions in plla. *Macromolecular Chemistry and Physics*, 217(18):2013–2026, 2016.
- [67] D. Baeten, V.B.F. Mathot, T.F.J. Pijpers, O. Verkinderen, G. Portale, P. Van Puyvelde, and B. Goderis. Simultaneous synchrotron WAXD and fast scanning (chip) calorimetry: On the (isothermal) crystallization of HDPE and PA11 at high supercoolings and cooling rates up to 200°C/s. *Macromol. Rapid Commun.*, 36(12):1184–1191, 2015.
- [68] F.J. Baltá-Calleja and C.G. Vonk. *X-ray scattering of synthetic polymers*. Number v. 8 in Polymer science library. Elsevier, 1989.
- [69] A.J. Ryan, W. Bras, G.R. Mant, and G.E. Derbyshire. A direct method to determine the degree of crystallinity and lamellar thickness of polymers: application to polyethylene. *Polymer*, 35(21):4537–4544, 1994.
- [70] M. van Drongelen, T. Meijer-Vissers, D. Cavallo, G. Portale, G. Vanden Poel, and R. Androsch. Microfocus wide-angle x-ray scattering of polymers crystallized in a fast scanning chip calorimeter. *Thermochimica Acta*, 563:33 – 37, 2013.
- [71] Q. Zia, D. Mileva, and R. Androsch. Rigid amorphous fraction in isotactic polypropylene. *Macromolecules*, 41(21):8095–8102, 2008.
- [72] H.J.M. Caelers, L.E. Govaert, and G.W.M. Peters. The prediction of mechanical performance of isotactic polypropylene on the basis of processing conditions. *Polymer*, 83:116–128, 2016.

-
- [73] V. Brucato, S. Piccarolo, and G. Titomanlio. Crystallization kinetics in relation to polymer processing. *Makromolekulare Chemie. Macromolecular Symposia*, 68(1):245–255, 1993.
- [74] S.S. Pesetskii, B. Jurkowski, Y.A. Olkhov, S.P. Bogdanovich, and V.N. Koval. Influence of a cooling rate on a structure of PA6. *Eur. Polym. J.*, 41(6):1380–1390, 2005.
- [75] T.B. van Erp, D. Cavallo, G.W.M. Peters, and L.E. Govaert. Rate-, temperature-, and structure-dependent yield kinetics of isotactic polypropylene. *Journal of Polymer Science Part B: Polymer Physics*, 50(20):1438–1451, 2012.
- [76] R. Popli and L. Mandelkern. Influence of structural and morphological factors on the mechanical properties of the polyethylenes. *Journal of Polymer Science Part B: Polymer Physics*, 25(3):441–483, 1987.
- [77] M. Elmajdoubi and T. Vu-Khanh. Effect of cooling rate on fracture behavior of polypropylene. *Theoretical and Applied Fracture Mechanics*, 39(2):117 – 126, 2003.
- [78] T. Ree and H. Eyring. Theory of Non-Newtonian Flow. I. Solid Plastic System. *Journal of Applied Physics*, 26(7):793–800, 1955.
- [79] E. Parodi L. E. Govaert, G. W. M. Peters. *Prediction of plasticity-controlled failure in polyamide 6: influence of temperature and relative humidity*. PhD thesis, Chapter 2, 2017.
- [80] H.A. Visser, T.C. Bor, M. Wolters, T.A.P. Engels, and L.E. Govaert. Lifetime assessment of load-bearing polymer glasses: An analytical framework for ductile failure. *Macromol. Mater. Eng.*, 295(7):637–651, 2010.
- [81] D.P. Russell and P.W.R. Beaumont. Structure and properties of injection-moulded nylon-6. *Journal of Materials Science*, 15(1):197–207, 1980.
- [82] F. Ghiam and J.L. White. Phase morphology of injection-molded blends of nylon-6 and polyethylene and comparison with compression molding. *Polym. Eng. Sci.*, 31(2):76–83, 1991.
- [83] T.B. Van Erp, L.E. Govaert, and G.W.M. Peters. Mechanical performance of injection-molded poly(propylene): Characterization and modeling. *Macromolecular Materials and Engineering*, 298(3):348–358, 2013. cited By 6.
- [84] B.A.G. Schrauwen, L.C.A. Breemen, A.B. Spoelstra, L.E. Govaert, G.W.M. Peters, and H.E.H. Meijer. Structure, deformation, and failure of flow-oriented semicrystalline polymers. *Macromolecules*, 37(23):8618–8633, 2004.

- [85] B. Yalcin, D. Valladares, and M. Cakmak. Amplification effect of platelet type nanoparticles on the orientation behavior of injection molded nylon 6 composites. *Polymer*, 44(22):6913 – 6925, 2003.
- [86] E. Parodi L. E. Govaert, G. W. M. Peters. *Structure-properties relations in polyamide 6 processed in quiescent condition: influence of the thermal history on mechanical performance*. PhD thesis, Chapter 4, 2017.
- [87] J. J. Hermans, P. H. Hermans, D. Vermaas, and A. Weidinger. Quantitative evaluation of orientation in cellulose fibres from the x-ray fibre diagram. *Recueil des Travaux Chimiques des Pays-Bas*, 65(6):427–447, 1946.
- [88] Sanjay Rastogi, Yefeng Yao, Sara Ronca, Johan Bos, and Joris van der Eem. Unprecedented high-modulus high-strength tapes and films of ultrahigh molecular weight polyethylene via solvent-free route. *Macromolecules*, 44(14):5558–5568, 2011.
- [89] R. Forstner, G. W. M. Peters, and H. E. H. Meijer. A novel dilatometer for pvt measurements of polymers at high cooling - and shear rates. *IPP*, 24(2):114–121, May 2009.

Samenvatting

Engineering plastics worden veelvuldig gebruikt voor onderdelen die mechanisch worden belast en dus spelen faalgedrag en levensduur een belangrijke rol. De betrouwbaarheid kan op dit moment alleen worden ingeschat door het uitvoeren van testen aan de producten zelf; een kostbare en tijdrovende procedure waardoor productoptimalisatie en anticiperen op markteisen problematisch is.

Het doel van dit onderzoek is om nieuwe experimentele methoden en procedures te ontwikkelen voor het meten van cruciale materiaaleigenschappen van Nylon 6. Deze kunnen worden gebruikt om nauwkeurige voorspellingen te doen van de levensverwachting van mechanische belaste onderdelen. Hierbij wordt ook de interactie tussen productkwaliteit en de vormgevingscondities in rekening gebracht, waardoor het mogelijk wordt om al in een vroeg stadium van het productontwerp optimalisatie door te voeren. Dit zal leiden tot lichtere, meer betrouwbare producten, een kortere time-to-market en betere service.

De complexiteit van dit onderzoek is gelegen in polymorfisme en de vocht-genduceerde verlaging van de glasovergangstemperatuur (T_g) van Nylon 6. Deze twee fenomenen kunnen grote variaties in eigenschappen veroorzaken en dus ook in de productkwaliteit en komen daarom uitgebreid aan de orde.

Eerst wordt een semi-empirische methode ontwikkeld die geschikt is voor het voorspellen van plastisch gedomineerd falen van Nylon 6 voor verschillende vochtigheid condities. De methode is gebaseerd op een gemodificeerde Ree-Eyring expressie. De gewone versie van deze expressie beschrijft de kinetiek van plastische deformatie als functie van temperatuur en deformatiesnelheid. Het effect van de verlaging van T_g ten gevolge van waterabsorptie is in rekening gebracht door de echte temperatuur te vervangen door een schijnbare temperatuur die een functie is van het vochtgehalte. Deze modificatie is gebaseerd op de hypothese dat het verschil tussen T_g en de echte temperatuur bepalend is voor het mechanisch gedrag. Dit model is eerst getest op samples die op dezelfde wijze zijn gemaakt, namelijk bij een constante temperatuur van 80°C wat leidt tot kristallisatie in de γ -fase. Om de relatie tussen structuur en eigenschappen te verhelderen zijn daarna samples getest die met een verschillende thermische geschiedenis zijn gemaakt door middel van compressie en van spuitgieten.

Vervolgens is de invloed van vormgevingsproces op structuurformatie onderzocht. Eerst is de kristallisatie kinetiek gemeten met behulp van Flash-DSC (ultra-fast scanning calorimetry).

Daarna zijn compressie- en spuitgietsamples kristallografisch gekarakteriseerd met behulp van Wide angle X-ray diffraction (WAXD) en Small angle X-ray scattering (SAXS). Voor de drie sample-productiemethoden zijn er zijn duidelijke verschillen gevonden in de kristallisatie kinetiek.

Bovendien is gevonden dat er een duidelijke invloed is van de structuurformatie op de glasovergangstemperatuur in de droge conditie ($T_{g,d}$). Dit fenomeen is in detail bestudeerd met behulp van flash-DSC voor kristallisatie bij isotherme condities en voor continue koeling. Het blijkt dat $T_{g,d}$ niet afhankelijk is van de krista $T_{g,d}$ als functie van de RAF/MAF-ratio geeft en, daarmee, een link met de thermische geschiedenis.

Concluderend kan worden gesteld dat dit onderzoek een set van methoden heeft opgeleverd die kunnen worden gebruikt voor het voorspellen van de eigenschappen van Nylon 6 producten als functie van hun thermische productiegeschiedenis en de gebruikscondities, te weten temperatuur en vochtigheid.

Acknowledgments

First of all, I want to thank Prof. Leon Govaert and Prof. Gerrit Peters for giving me the possibility to work with them for the last 4 years. They have strongly contributed to my professional growth. I also want to thank all the committee member for being part of this Ph.D defense.

I want thank my group, all the staff and all the PhD-students. In particular the colleagues with whom i have shared the "famous" office 4.22 and all the "regular visitors".

I also want to mention the friends with whom I have been spending my free time during these 4 years in The Netherlands. Mainly because of our incredible passion for motorcycles we have shared the happiest and only sometimes saddest moment of our sport/life.

This part continues in Italian because it goes to my family. Uno dei piu grossi ringraziamenti va ai miei genitori. Una volta ancora sono stati un pilastro nella mia vita. Grazie a loro ogni decisione é stata e sarà piu facile. Con i miei genitori, voglio citare anche mio fratello, mia nonna, i mei zii, zie e cugini.

Continuo in italiano anche per i miei amici della "vecchia guardia". Nonostante l'assenza, seppur a piccole dosi, le relazioni si mantengono e rimangono un riferimento.

Since 4 years I also have a second family, incredibly nice people who have accepted me as a son since the first time we met. Spasibo!

To conclude, I want to thank my girlfriend Daria. She is my daily partner, she gets the best and the worst of myself. With her by my side, everything is possible (even obtaining a Ph.D).

Curriculum Vitae

Emanuele Parodi was born in Genoa on the 19th May 1988. He started his academic path at the Genoa University, where he received his B.Sc. in Materials Science in March 2011. He continued his study at the same university. During his master he moved to Singapore for an internship in the Department of Materials Science and Engineering, at the Nanyang Technological University. Next, he moved to The Netherlands where he completed his final master project in the Polymer Technology group, Department of Mechanical Engineering, Eindhoven University of Technology. In March 2013 he received his M.Sc. in Material Science and Engineering at the Genoa University, with the thesis Structure-properties relations in i-PP supervised by L.E. Govaert (Eindhoven University of Technology) and G.C. Alfonso (Genoa University). In June 2013 he started his Ph.D in the Polymer Technology group under the supervision of Prof. Leon Govaert and Prof. Gerrit Peters.

Since July 2017, Emanuele is employed as "Tyre Development Engineer" at Maxxis Tech Center Europe in Uden, The Netherlands.

List of publications

This thesis has resulted in the following papers:

- Prediction of plasticity-controlled failure in polyamide 6: influence of temperature and relative humidity, *submitted*
- Glass transition temperature versus structure of polyamide 6: a flash-DSC study, *in press, accepted manuscript*
- Structure-properties relations in polyamide 6 processed in quiescent condition: influence of the thermal history on mechanical performance, *in preparation*
- Injection molding of polyamide 6: influence of mold temperature on the yield and failure kinetics at different environmental conditions, *in preparation*

Additionally, the author contributed to a publication outside the scope of this thesis:

- Caelers, H.J.M., Parodi, E., Cavallo, D., Peters, G.W.M. Govaert, L.E. (2017). Deformation and failure kinetics of iPP polymorphs. *Journal of Polymer Science, Part B: Polymer Physics*, 55(9), 729747-729747

